ABSTRACT

Title of dissertation: *IN-OPERANDO* ELECTRON MICROSCOPY AND SPECTROSCOPY OF INTERFACES THROUGH GRAPHENE-BASED MEMBRANES

Alexander Yulaev, Doctor of Philosophy, 2017

Dissertation directed by: Professor Marina S. Leite,
Department of Materials Science
and Engineering, Institute for Research
in Electronics and Applied Physics, UMD

Doctor Andrei Kolmakov,
Center for Nanoscale Science
and Technology, NIST

Electron microscopy and spectroscopy (EMS) techniques enable (near-) surface and interfacial characterization of a variety of materials, providing insights into chemical/electrochemical and morphological information with nanoscale spatial resolution. However, the experimental realization of EMS in liquid/gaseous samples becomes problematic due to their incompatibility with high vacuum (HV) conditions. To perform EMS under elevated pressure conditions, electron transparent membranes made of thin C, SiO_2 or/and Si_3N_4 are implemented to isolate a liquid/gas sample from HV environment. Nevertheless, even a few ten nanometer-thick membrane deteriorates signal quality due to significant electron scattering. The other challenge of EMS consists in inaccessibility to probe solid state interfaces, *e.g.* solid-state Li-ion batteries, which makes their *operando* characterization

problematic, limiting the analysis to *ex situ* and *postmortem* examination.

The first part of my thesis focuses on developing an experimental platform for *operando* characterization of liquid interfaces through electron transparent membranes made of graphene (Gr)/graphene oxide (GO). The second part is dedicated to probing Li-ion transport at solid-state-battery surfaces and interfaces using ultrathin carbon anodes. I demonstrated the capability of GO to encapsulate samples with different chemical, physical, and biological properties and characterized them using EMS methods. I proposed and tested a new CVD-Gr transfer method using anthracene as a sacrificial layer. Characterization of transferred Gr revealed the advantages of our route with respect to a standard polymer based approach. A novel platform made of an array of Gr-capped liquid filled microcapsules was developed, allowing for a wide field of view EMS. I showed the capability of conducting EMS analysis of liquid interfaces through Gr membranes using energy-dispersive X-ray spectroscopy, photoemission electron microscopy, and Auger electron spectroscopy. Using *operando* SEM and AES, I elucidated the role of oxidizing conditions and charging rate on Li plating morphology in all-solid-state Li-ion batteries with thin carbon anodes. *Operando* EMS characterization of Li-ion transport at battery interfaces with carbon or Gr anodes will provide valuable insights into safe all-solid-state Li-ion battery with enhanced performance.

IN-OPERANDO ELECTRON MICROSCOPY AND SPECTROSCOPY OF INTERFACES THROUGH GRAPHENE-BASED MEMBRANES

by

Alexander Yulaev

Dissertation submitted to the Faculty of the Graduate School of the
University of Maryland, College Park in partial fulfillment
of the requirements for the degree of
Doctor of Philosophy
2017

Advisory Committee:
Prof. Marina S. Leite, MSE and IREAP, Advisor/Committee Chair
Prof. John Cumings, MSE
Dr. Andrei Kolmakov, CNST NIST, Co-Advisor
Prof. Oded Rabin, MSE and IREAP
Prof. Srinivasa R. Raghavan, ChBE, Dean's Representative

© Copyright by
Alexander Yulaev
2017

Acknowledgments

First of all, I would like to thank my thesis advisers Prof. Marina S. Leite (MSE, IREAP UMD) and Dr. Andrei Kolmakov (CNST NIST) for their helpful mentorship, patience, and guidance over the years I spent at UMD and NIST. I want to especially thank Prof. Leite for advising me to focus on one scientific problem at a time and Dr. Kolmakov for various assignments to diversify my theoretical and hands-on experience. In a nutshell, completing the dissertation would not have been conceivable without my advisors' contributions.

Next, I want to thank all CNST NIST staff. Particularly, I would like to give special thanks to Drs. Nikolai Zhitenev, Jabez McClelland, Paul Haney, Robert D. McMichael, Renu Sharma, Veronika Szalai, Mark D. Stiles, Michael P. Zwolak, Stephan Stranick, Dmitri Ruzmetov, Vladimir Oleshko, Hongxuan Guo, Evgheni Strelcov, Guangjun Cheng, Angela R. Hight Walker, and Canhui Wang for insightful comments on my projects. I also wish to highlight the contributions by Marc Cangemi, Lei Chen, Gerard Henein, Alline Myers, Joshua Schumacher, Kerry Siebein, Alan Band, Neal Bertrand, Steve Blankenship, Barbara Coalmon, Russell Hajdaj, and Glenn Holland for technical support and invaluable training. I also want to acknowledge our collaborators: Drs. Ivan Vlassiouk (ORNL), Alexey Lipatov (University of Nebraska-Lincoln), Alexander Sinitskii (University of Nebraska-Lincoln), Annie Xi Lu (UMD), A. Alec Talin (Sandia), Jiaxing Huang (Northwestern University), Vjollca Konjufca (SIUC), Marjorie Brooks (SIUC), and Nina Kovtyukhova (Penn State University).

I also greatly appreciate the input from the other thesis committee members Prof. John Cumings (MSE), Prof. Srinivasa R. Raghavan (ChBE), and Prof. Oded Rabin (MSE, IREAP). Finally, I should acknowledge support under the Cooperative Research Agreement between the University of Maryland and the National Institute of Standards and Technology Center for Nanoscale Science and Technology, Award 70NANB14H209, through the University of Maryland.

Contents

List of Tables

List of Figures

List of Abbreviations

2D	Two-dimensional
3D	Three-dimensional
AES	Auger electron spectroscopy
AFM	Atomic force microscopy
ALD	Atomic layer deposition
APS	Ammonium persulfate solution
BCC	Body-centered cubic
BE	Binding energy
BSE	Backscattered electrons
CVD	Chemical vapor deposition
DC	Direct current
DD	Double donor
DI	Deionized
E. coli	*Escherichia coli*
EDS	Energy-dispersive X-ray spectroscopy
EELS	Energy-loss spectroscopy
EMS	Electron microscopy and spectroscopy
E-T	Everhart-Thornley
FFT	Fast Fourier transform
FOV	Field of view
GO	Graphene oxide
Gr	Graphene
GSV	Gray scale values
HRTEM	High-resolution transmission electron microscopy
HV	High vacuum
IMFP	Inelastic mean free path
IPA	Isopropyl alcohol
LCO	Lithium cobalt oxide
LED	Lower electron detectors

LEEM	Low-energy electron microscopy
LiPON	Lithium phosphorus oxynitride
LVSEM	Low-voltage scanning electron microscopy
MALDI	Matrix-assisted laser desorption/ionization
MCA	Multi-channel array
MCP	Microchannel plate
MEMS	Microelectromechanical systems
ML	Monolayer
MS	Materials science
NW	Nanowire
PAH	Polyaromatic hydrocarbons
PDMS	Polydimethylsiloxane
PE	Primary electrons
PEEM	Photoemission electron microscopy
PMMA	Poly(methyl methacrylate)
ROI	Regions of interest
SAED	Selected area electron diffraction
SD	Single-donor
SE	Secondary electrons
SEM	Scanning electron microscopy
SESSA	Simulation of electron spectra for surface analysis
SSE	Solid-state electrolyte
SSLIB	All-solid-state Li-ion battery
STEM	Scanning transmission electron microscopy
TE	Transmitted electrons
TEM	Transmission electron microscopy
TEY	Total electron yield
TTL	Through-the-lens
UHV	Ultra-high vacuum
UV	Ultraviolet
XAS	X-ray absorption spectroscopy
XPS	X-ray photoelectron spectroscopy

Chapter 1: Introduction

Materials science (MS) is an interdisciplinary research field, which establishes interdependent relations between the structure, properties, performance, and processing of materials. The "materials science tetrahedron" with all four components in its vertices is usually used to illustrate these relationships graphically (Figure 1.1). Profound understanding of materials structure, properties, performance, and processing is of outmost importance for engineers; therefore, a comprehensive characterization is required for each component of MS tetrahedron. Electron microscopy and spectroscopy (EMS) are among the most powerful and widely used techniques for (near-) surface and interfacial characterization, where incoming and/or outgoing electrons with different probing depths are used to obtain chemical and/or morphological information of a sample. Table 1.1 displays the information on a typical energy range, input and output signals for most EMS techniques. Many materials, processes, and systems of interest, such as batteries, fuel cells, (photo-)catalysts, bio samples, film growth, corrosion, *etc.*, require EMS characterization either during their operation (*operando*) or on site (*in situ*). However, the conventional EMS necessitate high or ultra-high vacuum (HV, UHV) conditions, which restricts the sample choice to non-volatile materials (mostly solids). The other challenge of EMS

consists in inaccessibility to probe solid state interfaces, *e.g.* solid-state Li-ion batteries (SSLIB), which makes their *operando* characterization problematic, limiting the analysis to *ex situ* and *postmortem* examination. For example, it is vitally important to monitor the early stages of Li oxidation at surfaces and interfaces of SSLIB during its cycling with nanoscale resolution because such irreversible processes eventually define the capacity loss mechanisms and the lifetime of the battery. In sections 1.1 and 1.2, I provide historical introduction and state of research for each problem. In section 1.3, I briefly present the current MSE problems and objectives of this thesis, which address the stated problems.

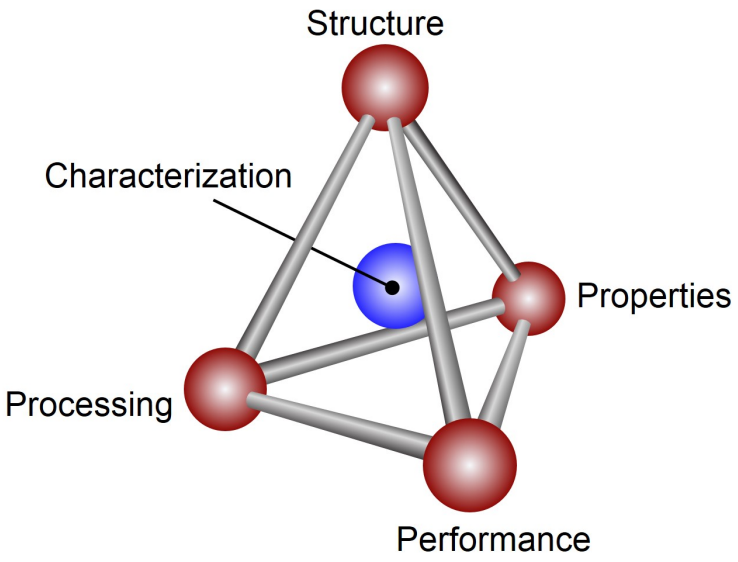

Figure 1.1: Materials science tetrahedron representing the relationships between structure, properties, processing, and performance. The characterization of materials is equally important for each component, thus it is posited in the middle of the tetrahedron.

Table 1.1: EMS techniques

EMS technique	Excitation probe	Measured signal
SEM	<30 kV electrons	secondary and backscattered electrons
TEM	100-300 keV electrons	transmitted electrons
STEM	<300 kV electrons	transmitted electrons
EELS	100-300 keV electrons	scattered electrons
XPS	10^3 eV X-rays	valence and core level electrons
AES	<30 kV electrons, ions or X-rays	Auger electrons
LEEM	1-100 eV electrons	elastically scattered low energy electrons
PEEM	UV light, synchrotron radiation (soft and hard X-rays)	secondary electrons, valence, core level, Auger electrons
EDS	<300 kV electrons	characteristic X-rays
EBSD	<30 kV electrons	backscattered electrons

1.1 *In situ/operando* SEM, TEM, XPS, XAS in liquid, gaseous, and reactive samples

Two approaches have been successfully implemented to extend conventional HV EMS to "real world" elevated pressure environment, thus allowing for *in situ* and *operando* analysis of gaseous and liquid systems. These are instruments equipped with: (i) differential pumping stages or (ii) electron transparent membranes. Figure 1.2 shows different scanning and transmission electron microscopy (SEM/TEM) setups: (a) traditional HV, (b) differentially pumped, (c-d) membrane based SEM/TEM or "closed cell". [1]

1.1.1 Open cell configuration: differential pumping approach and direct imaging of low-vapor liquids

The differential pumping relates to an "open cell" type (Figure 1.2 (b)) and is based on implementing small apertures to maintain elevated pressure (up to ∼0.3 bar/220 Torr) within the region of interest and HV conditions at objective lenses. The first open cell in TEM was reported in 1942 (Figure 1.3). [1,2] The same open cell approach is still actively used in modern EMS, *e.g.* for *in situ* imaging of nanostructures growth under reactive gas conditions using TEM (Figure 1.4 (a)) [3] or *in situ* chemical characterization of water phase transformations (Figure 1.4 (d)), [4] water adsorption onto different substrates of interest, [5,6] chemical state variation of a catalyst (Figure 1.4 (c)) [7–9] using ambient pressure X-ray photoelectron spectroscopy

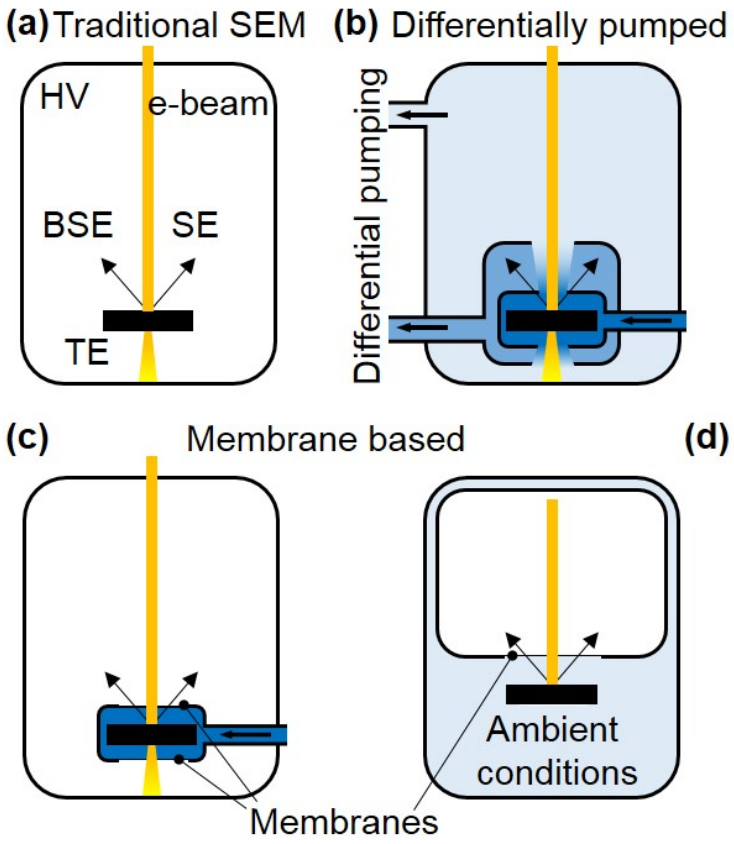

Figure 1.2: SEM and TEM architectures. (a) Traditional HV setup. (b) Differentially pumped open cell. (c) Closed cell with electron transparent membranes. (d) Atmospheric pressure SEM. BSE, SE, TE, and HV stand for backscattered, secondary, transmitted electrons, and high vacuum, respectively.

(XPS) and X-ray absorption spectroscopy (XAS) [10] (Figure 1.4 (b-d)), and catalytic CO oxidation of Pt using photoemission electron microscopy (PEEM). [11]

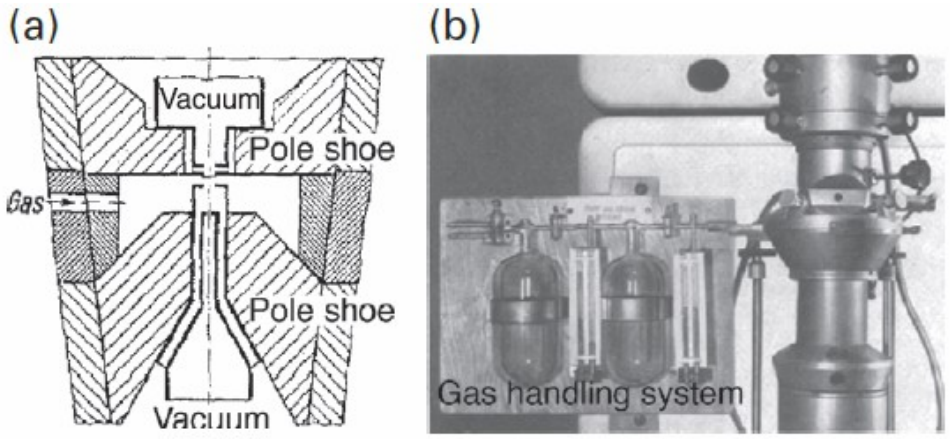

Figure 1.3: First environmental TEM equipped with differentially pumping stage. (a) Schematic of the chamber and (b) photograph of the TEM with a gas handling system. [1, 2]

Low-vapor liquids, such as room temperature ionic ones, can be loaded directly into an HV chamber and characterized directly using EMS with only little modifications of sample preparation. *In situ* probing ionic liquid films unveiled new details of crystal nucleation and growth, particle motion, surface passivation, and battery reactions. [12–14]

1.1.2 Membrane-based cells

In closed cell setups, the sample of interest is isolated from HV of EMS chamber by a molecular-impermeable, electron-transparent, and mechanically robust membrane capable to withstand the pressure differential between HV and the sample environment (Figure 1.2 (c)). Whether the membrane is transparent to electrons

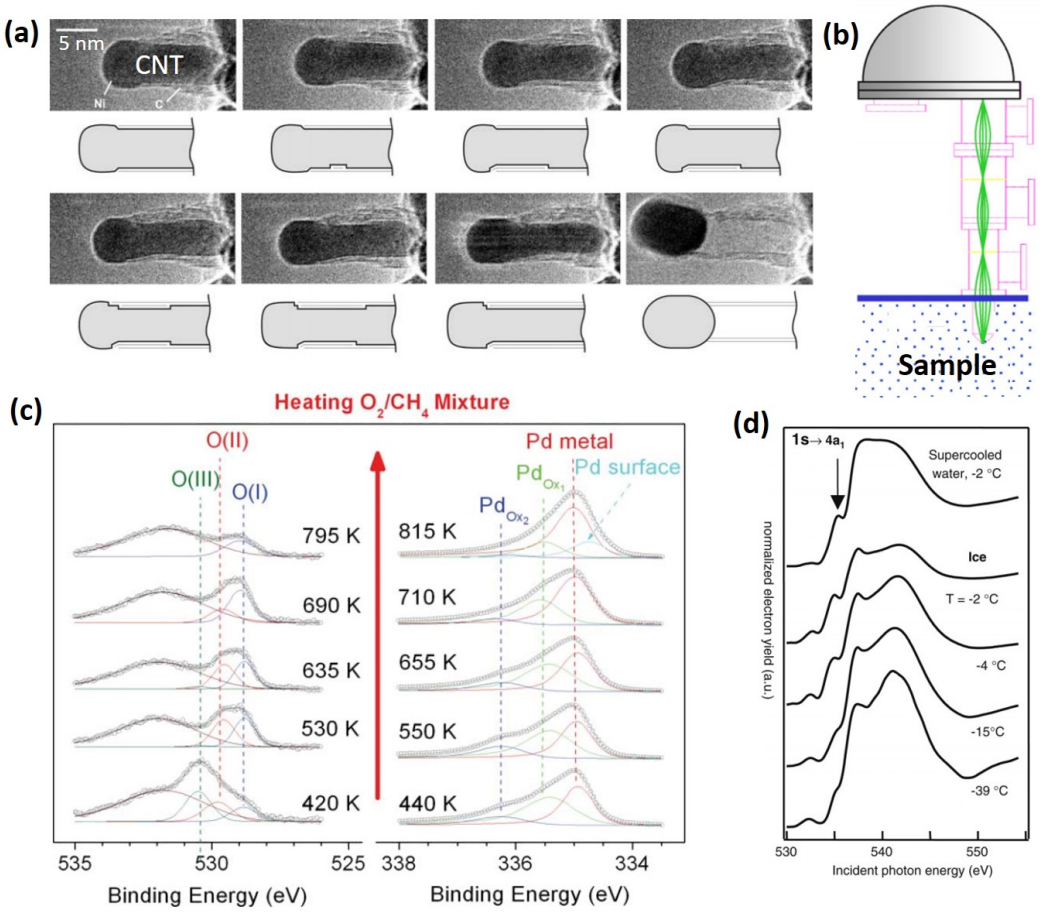

Figure 1.4: Environmental TEM, XPS, and XAS. (a) *In situ* TEM images of carbon nanotube growth. [3] (b) Schematic of differentially pumped electron spectrum analyzer (adapted from [10]). (c) Environmental XPS spectrum evolution of O and Pd peaks recorded during heating in an O_2/CH_4 mixture. [15] (d) Auger-electron-yield XAS of water and ice for a few values of temperature. [10]

depends on the ratio between a membrane's thickness, d, and material dependent inelastic mean free path of electrons (IMFP), λ: [16, 17]

$$\frac{I}{I_0} = e^{-\frac{d}{\lambda}}, \tag{1.1}$$

where I_0 and I are intensities of initial and attenuated electron signals, respectively. In practice, a few ten nanometer thick membranes made of silicon, silicon nitride, silica or amorphous carbon are used as electron transparent membranes for electrons with kinetic energies in excess of 10 keV. Figure 1.5 (a) depicts the theoretical IMFP dependence on electron energy in graphite, which consists of electron transparent graphene layers used almost in all experiments of this thesis. A gray region shows a 2 nm thick graphite membrane. According to eq. 1.1, the exponential dependence of intensity allows us to conventionally assume that the graphite membrane is transparent to electrons in regions I ($d < \lambda$) and opaque to ones in domain II ($d > \lambda$).

Monte Carlo simulation can be used to visualize the electron scattering in multilayered structures (Figure 1.5 (b-c)). The figures depict the electron beam scattered in a water liquid cell without and with 200 nm Au nanoparticle on the path of the electron beam, respectively. The cell is capped with a 30 nm thick Si_3N_4 membrane. The electron scattering from the particle results in a dramatic increase in the BSE signal. Therefore, the implementation of electron transparent membranes capping the liquid cells makes SEM imaging of objects immersed below

the membrane-liquid medium interface feasible.

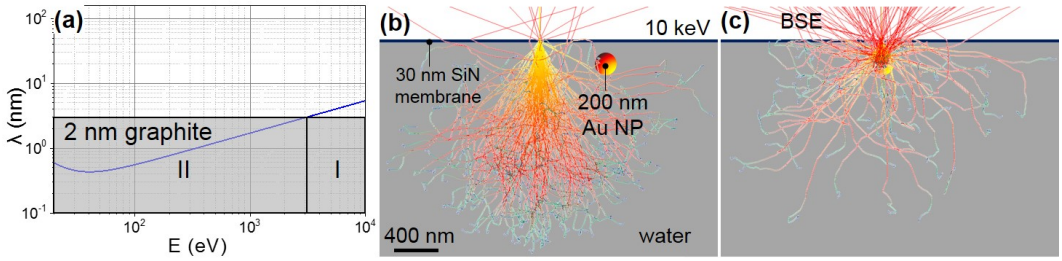

Figure 1.5: Examples of electron transparency. (a) IMFP dependence on an electron energy in graphite. The calculations are from the Penn algorithm. [18] A gray region depicts a 2 nm thick carbon membrane. Regions I and II correspond to transparency and opacity of the membrane to electrons, respectively. (b) Monte Carlo simulation of 10 keV electron beam scattering in a water liquid cell capped with a 30 nm thick Si_3N_4 membrane. (c) 10 keV electron beam scattering in the same liquid cell illustrated as in panel (b) but with a 200 nm Au nanoparticle. Red trajectories show BSEs.

The region that can be probed below the membrane-liquid interface is defined by the Kanaya-Okayama equation as:

$$R_{KO} \approx \frac{27.6W \cdot E_b^{1.67}}{Z^{0.89} \cdot \rho}, \tag{1.2}$$

where R_{KO} [nm], W [g/mol], Z, ρ [g/cm^3], and E_b [keV] stand for the electron interaction range, the atomic weight, atomic number, mass density of the sample, and electron beam energy, respectively. [19, 20] According to eq. 1.2, an interaction volume spans from ∼50 nm to ∼2000 nm for a water sample buried beneath a 30 nm thick Si_3N_4 membrane when the energy of the electron beam increases from 1 keV to 10 keV (Figure 1.5 (b)). Figure 1.6 (a) shows a schematic of electron in-

teraction volume partitioned into characteristic zones, which specify what type of signal can characterize these regions. Auger electrons escape the sample without inelastic scattering only from a few nanometer deep region, making Auger electron spectroscopy (AES) a surface sensitive technique. The SE signal is useful to characterize several tens of nanometers beneath the sample surface. Moving further into the sample from the free surface, the regions of characteristic X-ray radiation, BSEs, Bremsstrahlung, and secondary fluorescence signal follow sequentially. Thus, choosing the proper technique is important to characterize a sample of interest located at specific depths in the liquid.

It is crucial to understand how the SEM contrast depends on the electron beam (e-beam) energy and materials properties. During imaging the sample immersed into the liquid and capped with a thin membrane, the resultant signal, S, comprises several components (Figure 1.6 (b)): secondary electrons (SEs), backscattered electrons (BSEs) due to a sample (s) and a membrane (m)

$$S = SE_m + BSE_m + SE_s + BSE_s. \tag{1.3}$$

The SE_s component is a result of inelastic scattering of BSEs and usually is called SEs type 2. The total BSE coefficient is the sum of corresponding BSE signals:

$$\eta = \eta_m + \eta_s. \tag{1.4}$$

Similarly, for the total SE yield, δ, one can specify:

$$\delta = \delta_m + \Delta \cdot \eta_s, \tag{1.5}$$

where Δ refers to SEs scattered due to BSEs from the sample. Thus, the total electron signal collected by the detector with corresponding efficiencies ϵ_{SE} and ϵ_{BSE} is:

$$S = \epsilon_{BSE} \cdot \eta + \epsilon_{SE} \cdot \delta. \tag{1.6}$$

The contrast, C, between two points (A and B) can then be defined as

$$C = \frac{S_A - S_B}{S_A}. \tag{1.7}$$

In case of relatively high energy of the PE beam, the scattering from a membrane is negligible, and eq. 1.7 may be approximated by

$$C = \frac{\eta_{SA} - \eta_{SB}}{\eta_{SA}}. \tag{1.8}$$

Eq. 1.8 emphasizes the importance of BSEs on contrast formation mechanism. To conclude, the electron scattering contribution from the membrane to the ultimate signal fades with electron energy growth, and the maximum contrast is obtained if

the electron signals from an object and liquid media significantly differ from each other, *e.g.* the BSE coefficient increases by ≈4 times, resulting in $C = 0.73$ (see Figure 1.5 (b,c))

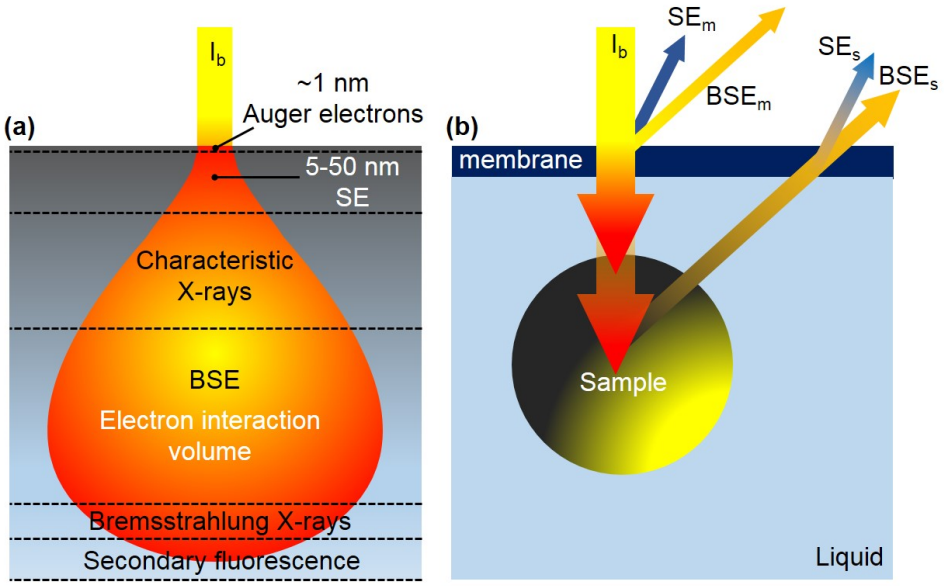

Figure 1.6: Electron beam interaction with a sample. (a) Schematic of interaction volume divided into regions showing what type of signal characterizes them. (b) Illustration of scattered electrons from membrane-liquid-sample system: secondary electrons (SEs), backscattered electrons (BSEs) due to a sample (s) and a membrane (m).

History of membrane-based cells for EMS

The pioneering works on implementation of ultra-thin electron transparent membranes to seal a liquid cell and perform electron microscopy at elevated pressure date back to 1935 [21] and 1944, [22] where aluminum and collodion films were used, respectively. Over last three decades, the progress in microfabrication and imaging opened new routes to liquid cell EMS. For instance, microfabricated 10–100 nm thick carbon [23, 24], polymer, SiO_2, and Si_3N_4 [25–31] membranes demonstrated

high transparency to both 10–300 keV electrons and 1×10^3 to 1×10^4 eV X-rays, which propelled research in both ambient pressure electron microscopy [23,26,32,33] and X-ray spectroscopy. [34, 35] The capability to characterize buried interfaces through ultra-thin SiO_2 membranes using PEEM was demonstrated in Ref. [36]. The ambient pressure PEEM in transmission configuration was used to characterize CaI_2 solution droplets confined between two Si_3N_4 membranes. [37]

Recently, a large-scale synthesis of 2D atomically thin materials, such as boron nitride, graphene (Gr), [38–42], graphene oxide (GO), [43–45] and their transfer [46–48] methods were developed. These 2D materials establish a new scalable and versatile platform for ultra-thin membrane based ambient pressure cells, offering intriguing opportunities for XPS [49] and AES within 100 – 1000 eV characteristic energies of electrons. Particularly, a single layer Gr demonstrates unique properties: chemical inertness, unprecedented mechanical intrinsic tensile strength (130 GPa) and a Young's modulus (1 TPa), [50, 51] ultimate electron transparency (negligible electron scattering) due to a small scattering cross-section, [52–55] and impermeability to gases and liquids. [56–58] All these properties allowed for the realization of liquid cells based on Gr and GO membranes for SEM, [59, 60] high-resolution transmission electron microscopy (HRTEM), [61] synchrotron-based PEEM, [62] photoelectron spectroscopy, [63] and XPS. [60] Other 2D materials cannot compete with Gr/GO for EMS applications due to a rapid degradation under water and oxygen exposure (*e.g.* phosphorene [64]) or brittleness (*e.g.* $MoSe_2$ [65]).

1.1.3 Applications

There is a number of applications where *in situ/operando* EMS can provide invaluable insights into details of physical and chemical mechanisms in a stark contrast to other characterization methods. Atmospheric pressure EMS can be employed in modern biology to study the molecular machinery underlying cellular function. [66, 67]. For example, *Helicobacter pylori* bacterium preserved in saline was labeled with Au nanoparticles and probed through ultra-thin membrane using *in situ* SEM (Figure 1.7 (a)). [68] Au-labeled epidermal growth factor receptors on whole fixed fibroblast cells were analyzed with scanning transmission electron microscopy (STEM) in a microfluidic chamber (Figure 1.7 (b)). [26] Ambient pressure EMS was helpful to study dynamics of structural changes that occur in individual biomolecules during nutrient injection [69]. The intercellular variation of HER2 proteins, which are important for breast cancer aggressiveness and progression study, were localized using environmental SEM. [70]

In the realm of materials science, EMS enable *in situ/operando* analysis of nucleation and growth of particles during electrochemical processes with high spatial and temporal resolutions, unveiling reaction kinetics and mechanisms. [27,28,71–75] For instance, Figure 1.7 (c) depicts the TEM images of potentiostatic deposition of Cu from 0.1M $CuSO_4$/0.18M H_2SO_4 onto an Au electrode. The obtained results are helpful to understand the effects of surface and bulk diffusion on size and density of metal nuclei. [76] *Operando* EMS enable correlative electron imaging (Figure 1.7 (c)) coupled with electrochemical characterization (Figure 1.7 (d)). In particular,

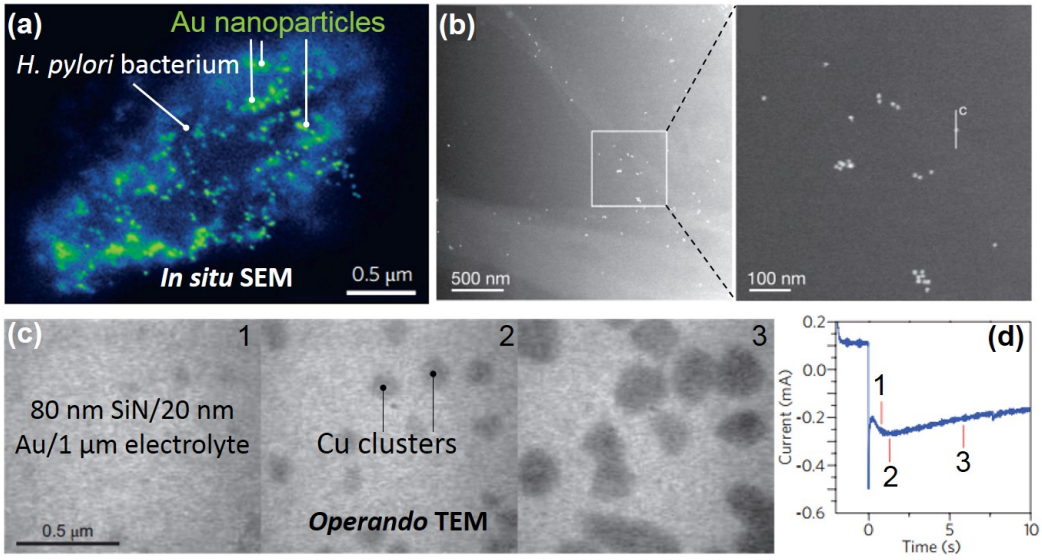

Figure 1.7: Ambient pressure EMS through electron transparent windows. (a) *Helicobacter pylori* bacterium preserved in saline was incubated with biotinylated gastrin on streptavidin-coated 20 nm Au nanoparticles and probed through an ultra-thin membrane using *in situ* SEM. (b) Au-labeled epidermal growth factor receptors on whole fixed fibroblast cells were analyzed with STEM in a microfluidic chamber. Bright features correspond to Au labels. [26] (c) A sequence of TEM images showing evolution of Cu potentiostatic deposition from 0.1M $CuSO_4$/0.18M H_2SO_4 onto an Au electrode. Dark contrast corresponds to Cu clusters; gray background relates to the 20 nm thick Au electrode, 80 nm thick Si_3N_4 window, and 1 μm thick electrolyte. (d) Temporal dependence of electrochemical current. Red lines point out moments when the images (panel c) were obtained. All figures are adapted from Ref. [67]

operando probing of dendrite formation has a high relevance to safety issues during Li-ion liquid battery operation. [77–82] Our understanding of particle and liquid motion at nanoscale can also benefit from liquid cell EMS experiments. [83–85] Finally, EMS can help examine solidification kinetics, [86] catalysis, [87] corrosion, [88–90] phase transformations during cooling or heating, and surface reactions. [91–93]

1.2 *In situ/operando* EMS in battery research

Besides liquid cell EMS, the thin membrane approach can be used to understand details of chemical/electrochemical processes occurring in battery research, *e.g.* solid-state Li-ion batteries. The recent progress in SSLIBs has led to novel opportunities in miniaturization of energy storing electrochemical cells, relevant to micro-electronics, autonomous and medical devices. [94] SSLIBs demonstrate a high specific power and double or triple energy density of liquid electrolyte electrochemical cells. Moreover, SSLIBs significantly reduce safety risks associated with a thermal runaway occurring in conventional liquid organic electrolytes. [95] Despite the rising interest in the energy storage community, the electro-mechanical and electro-chemical interfacial processes are not well understood at the nanoscale due to scarcity of experimental methods to map Li ion transport during battery cycling. For example, the details of Li plating/stripping inhomogeneity in contact with a solid electrolyte LiPON (lithium phosphorus oxynitride) [96] are still unknown. Better understanding of Li-ion transport at SSLIB anodes-electrolyte interfaces dur-

ing operation at the nanoscale will help reduce capacity losses upon cycling, identify local regions with increased mechanical strains, and improve electrode capacities.

To date, optical, electron, and atomic force microscopies (AFM) were employed to study Li-ion transport in SSLIBs. Electrochemical strain microscopy was implemented to probe Li-ion transport through LiPON into a thin Si anode at nanoscale [97]. The work revealed the bias induced Li-ion transport predominantly along the grain boundaries of a polycrystalline cathode (Figure 1.8 (a)). Because SSLIBs contain no volatile components, *operando* EMS studies of electrochemical processes can be conducted under vacuum conditions. Real-time UHV SEM, conductive AFM, and XPS were used to probe ternary Li-Al-O alloy anode systems (Figure 1.8 (b)). [98, 99] The results revealed a fast capacity fade owing to Li trapped in the alloyed Li-Al mounds. TEM was employed to probe the scaling limit of a LiPON layer in a nanowire SSLIB fabricated with a radial geometry (Figure 1.8 (c)). [100] Finally, Li electrochemical deposition at Li blocking current collector/LiPON interfaces was investigated using SEM for several charging rates (Figure 1.8 (d)). [101,102] Nucleation and growth of lithium nanorods were directly observed in SEM coupled with standard electrochemical experiments.

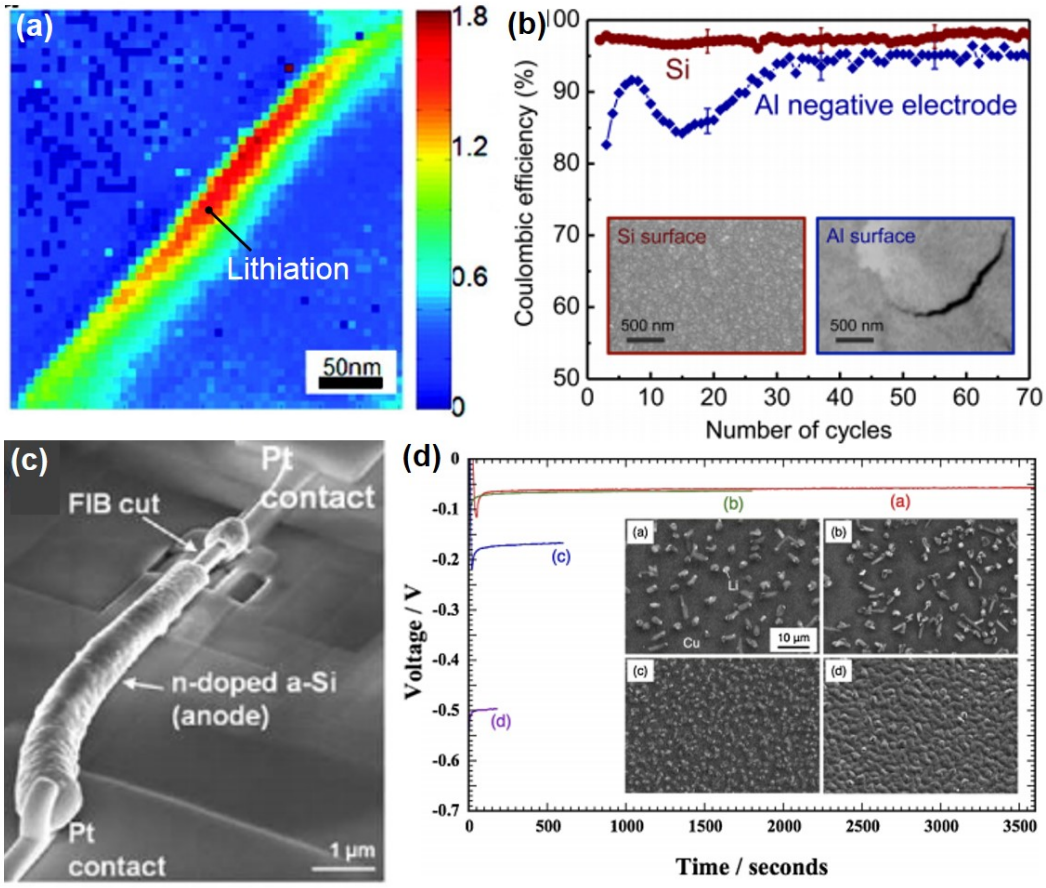

Figure 1.8: *Operando* characterization of SSLIBs. (a) Electrochemical strain microscopy revealed the Li-ion transport predominantly along the grain boundaries of a polycrystalline cathode. [97] (b) SEM imaging Li-Al-O alloyed mounds on an Al current collector resulting in a capacity fade. [99] (c) Nanowire SSLIB for an *operando* TEM study. [100] (d) SEM observation of Li nanorod growth at a Cu current collector/LiPON interface for (a) 50 μA cm^{-2}, (b) 100 μA cm^{-2}, (c) 300 μA cm^{-2}, and (d) 1 mA cm^{-2}. [101, 102]

1.3 Objectives of this thesis

In this dissertation, I posit several goals to be addressed using *operando* EMS, as divided into 4 following chapters:

- *Developing in situ/operando EMS characterization applied through graphene oxide membranes formed from an aqueous solution.* Processing quasi-2D membranes *via* spin coating or drop casting is very attractive. The details of self-assembling membranes from colloids remain an active field of research. To date, it is not completely understood whether GO self-assembling membranes can be used for encapsulation of micro- and nano-scale objects with successive EMS characterization through formed films. This part of the research focuses on the GO membrane formation from aqueous solution and testing the impact of GO encapsulation on compressible/incompressible, liquid/solid, bio, and reactive samples. In addition, the capabilities of optical and EMS characterization of encased micro- and nano- scale objects through encapsulant films are investigated. [103, 104]

- *Quantifying the cleanliness of the novel transfer method of CVD graphene onto a substrate of interest.* Clean chemically vapor deposited (CVD) Gr is required in different fields of science and technology; however, commonly used transfer methods of CVD Gr are usually based on polymer sacrificial layers, *e.g.* poly(methyl methacrylate) (PMMA), [105] thermal release tape, [42] *etc.*, which leave residues after removal of the sacrificial layer in solvents or by

thermal annealing. [106] Surface contaminants deteriorate mechanical, thermal, electronic, optical properties, and electron transparency of resultant Gr. This work aims to develop a clean method of carbon monolayer transfer based on an polyaromatic hydrocarbon (PAH) sacrificial layer that could be easily desorbed at temperatures below 150 °C. The proposed method will be of high importance for heat and humidity sensitive processing used in SSLIB fabrication. Comparative analysis of different Gr transfer methods is conducted using SEM, TEM, Raman, and XPS techniques. [107]

- *Developing and testing graphene liquid cells compatible with wide field of view EMS.* Common laboratory EMS equipment, such as XPS, would require millimeter wide electron transparent membranes to analyze liquid interfaces. However, point defects and grain boundaries of Gr obtained by CVD method restrict the size of Gr windows used in closed cells to a few micrometers. Therefore, ambient pressure XPS in closed cells can be realized only using beamline limited X-ray synchrotron radiation microscopes that enable a submicron focused X-ray beam. Finally, probing a liquid cell with a Gr membrane using EMS is also affected by a low Gr coverage and analysis of one sample per session. This research is dedicated to a novel design of Gr liquid cells: a multi-channel array (MCA) consisting of many isolated cells. The developed experimental platform could enable the correlative wide field of view EMS imaging and analysis, such as ambient pressure PEEM or conventional XPS (Figure 1.9). [63] The fabricated MCA platform capped with a Gr electron

transparent membrane could facilitate the high throughput characterization of liquid samples using SEM, AES, PEEM, and XPS. Several *operando* EMS practices are also tested. [108, 109]

- *Understanding the effect of oxidizing conditions and charging rate on Li plating morphology during SSLIB operation.* A Li anode is a promising material for SSLIBs due to both its high theoretical capacity (3860 $mAhg^{-1}$) and a low potential (-3.04 V vs. hydrogen anode). However, the origin of inhomogeneous electrochemical Li deposition/dissolution during SSLIB operation is not fully understood yet at nano- and mesoscales. Moreover, oxidizing contaminants, such as O_2, N_2, H_2O, have been shown to affect the durability and performance of SSLIB anodes, and the exact mechanism of irreversible interfacial changes is unclear. The effect of oxidizing conditions and charging rate on the nucleation and growth morphology of electrochemically plated Li should be elucidated using *operando* SEM and AES. For that, thin carbon anodes deposited onto solid state electrolyte will be probed using EMS methods during battery cycling. This system is the first step toward studying Li-ion transport at anode-electrolyte interfaces through electron transparent anodes.

1.4 Organization of this thesis

This thesis is composed of 6 chapters, as briefly described below and represented in Figure 1.10: Chapter 1 provides the motivation and a review of the literature about implementing *in situ*/*operando* EMS for liquid samples and reactive

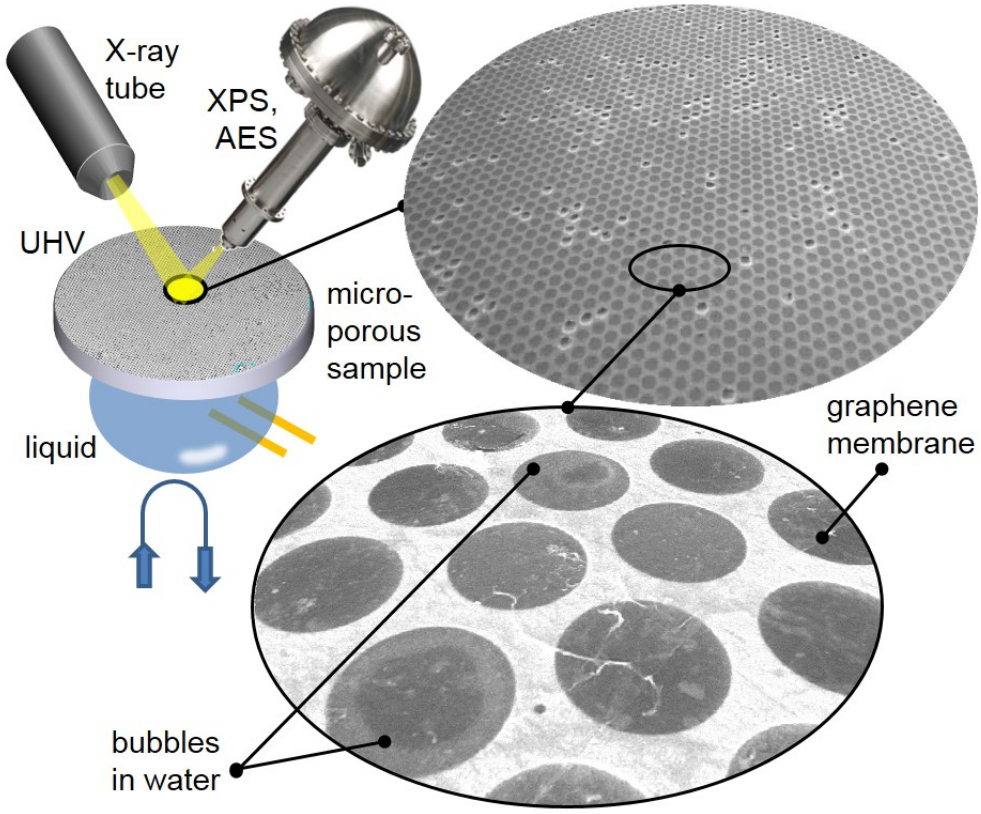

Figure 1.9: An MCA comprising numerous liquid filled isolated microchannels. Schematic of XPS and AES analyses for the proposed platform is also illustrated. [63]

materials.

Chapter 2 is focused on developing an encapsulation technique based on GO aqueous solution followed by EMS characterization of encapsulated objects through thin GO films. The developed approach would be helpful in histological practices, forensic studies, dip pen-like encapsulation technology and situations where reliable adhesion and isolation of reactive, toxic/radioactive samples or precious artifacts is required.

Chapter 3 presents a new method of CVD-grown Gr transfer based on an anthracene sacrificial layer, which sublimes at 150 °C. A systematic comparison of the most commonly used methods of Gr transfer applied under the same conditions is performed. The proposed method opens a new horizon for integrating clean graphene into complex devices, including the heat and humidity sensitive systems.

Chapter 4 describes the fabrication and testing of a multi-channel array for liquid cell EMS, including both advantages and limitations of the method. Results of *operando* EMS characterization of electrochemical reactions and crystal growth from liquid phases are presented. The new liquid cell platform paves the way for understanding details of chemical and electrochemical processes in liquid environment.

Chapter 5 is devoted to EMS characterization of Li metal plating at C-anode during the battery operation. Here, we combine theoretical model of nucleation and growth with experimental results of Li plating to quantify effects of oxidizing conditions and charging rate on Li plating/stripping morphology at C anodes.

Chapter 6 summarizes the main results of this thesis and provides an outlook

for future research directions on implementing electron transparent Gr anodes for Li-ion transport characterization in SSLIBs.

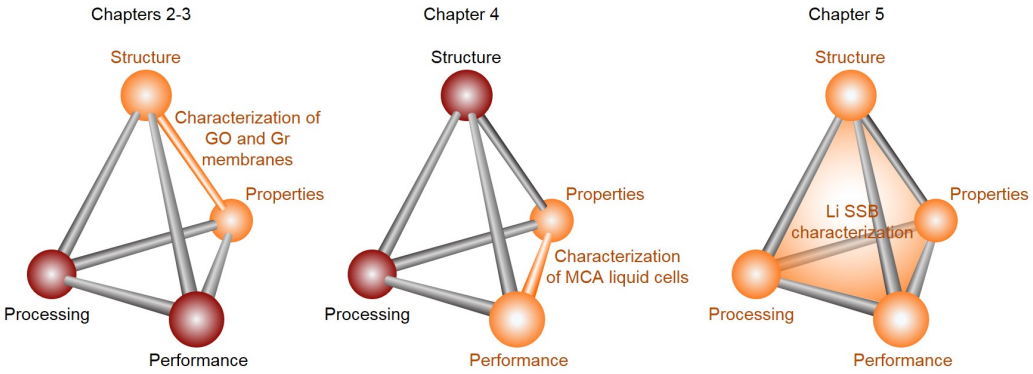

Figure 1.10: Organization of this thesis, illustrated by the MSE tetrahedron for each chapter.

Chapter 2: EMS enabled through the encapsulation of objects by graphene oxide membranes

This chapter demonstrates a technique for facile adhesion and encapsulation of micro- and nanoscale objects on arbitrary substrates, stencils, and micro structured surfaces by ultrathin graphene oxide membranes *via* a simple drop casting of graphene oxide solution. A stable encapsulating membrane forms during the drying process at the liquid-air and liquid-solid interfaces and consists of a water-permeable quasi-2D network of overlapping graphene oxide flakes. Upon drying and interlocking between the flakes, the encapsulating coating around the object becomes mechanically robust, and chemically protective. In addition, high transparent GO films to electrons and photons enable microscopic and spectroscopic access to encapsulated objects in a wide energy range. The characteristic encapsulation scenarios are demonstrated on a set of representative inorganic and organic micro and nanoobjects and microstructured surfaces. Finally, electron and optical microscopies/spectroscopies of objects through encapsulant films are conducted and discussed. The text and figures are adapted from Ref. [103]

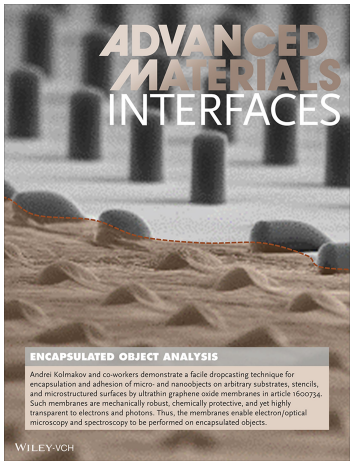

2.1 Motivation

The problems of object isolation from reactive environment and understanding the physics and chemistry of surface passivation are of great importance for a variety of applications, such as microelectronics, [110, 111] drug delivery, [112] forensics, [113, 113] archeology/paleontology, and space research. [114, 115] In scientific practices, encapsulation of micro-objects in organic matrices is commonly used in histology. [116] While, in general, encapsulation implies the protection of objects from undesirable effects of ambient conditions, the opposite is also true, and isolation can be important to protect the environment from hazardous effects of biologically or chemically reactive, toxic or radioactive nature of the encapsulated objects. [117, 118]

In addition to physicochemical protection of objects from the ambient, the ability to image and analyze the encapsulated matter spectroscopically is often a requirement. The latter becomes a challenge when the sampling area is reduced to meso- or nanoscale necessitating the application of electron, advanced optical or X-ray microscopies. [119] In the light of the aforementioned requirements, nanometer-thin membranes and coatings made of low atomic number (Z) elements, such as Gr and GO, were employed as electron transparent windows for *in situ* ambient pressure electron microscopy [59, 60] and optical and X-ray spectroscopy due to their high transparency to both photons [120,121] and electrons in a wide energy range. [53,122] GO colloids have a peculiar combination of properties and can serve a prospective material platform for high yield fabrication of encapsulating membranes [123–126]

with the following advantages: (i) amphiphilic nature of individual colloid particles, [125] (ii) unimpeded water permeability of hydrated membranes, [44] and (iii) mechanical stiffness upon drying. [123] Indeed, during mechanical tests values of the tensile elastic modulus exceeding 30 GPa were reported for the dry membranes, [123] implying that individual micro flakes are strongly interlocked inside the membrane. As it has been emphasized in Ref. [125], chemically exfoliated flakes have hydrophilic edges owing to facile deprotonation of terminating carboxyl groups in solution and largely hydrophobic basal planes due to the presence of polyaromatic domains of pure graphene [127]. The amphiphilicity of GO is a key factor responsible for segregation and formation of membranes at the liquid-air and liquid-solid interfaces in diluted solutions [44, 125, 128] and liquid crystal phases at high concentrations. [129–132] Conveniently, the amphiphilic properties may be tuned by varying the solution pH, their size or *via* chemical reduction. [125] Moreover, it was demonstrated that as formed membranes are highly permeable to water due to capillary-driven intercalation between the overlapping micro flakes and yet impermeable to many other liquids, vapors, and gases including helium. [44, 133–135] In a hydrated state a sharp cutoff in permeation of ions and molecules with hydration radius >0.45 nm was observed. [133] Based on this peculiar selectivity of the membranes, a variety of applications, such as their use as ultrathin selective filters, have been proposed. [136–139] Finally, the colloids are well suited for low cost and high yield aqueous processing, such as Langmuir–Blodgett, spin coating, nebulization, flow-directed assembly, jet printing, and drop casting protocols, [125] expanding the breadth of possible approaches for the GO-based encapsulation. [133]

In the realm of biology, important demonstrations of GO crumpled flakes as deoxyribonucleic acid cargo or bio-sensing platforms for molecular probing in living cells have been also reported. [140] Besides, protein-functionalized graphene has been successfully utilized to encapsulate live bacteria inside electron transparent cocoons suitable for *in vivo* TEM. [141] The development of GO encapsulation of sulfur particles and metal oxide nanoparticles [142] resulted in high energy density cathode composite materials for Li-ion batteries. [143, 144] In addition, aqueous solutions have been recently employed to encapsulate nanoparticles by aerosolizing suspensions followed by drying of micro-droplets, [145, 146] as well as used to create more effective matrices for mass spectroscopy. [147] Finally, the effectiveness of GO colloids for toxic or radionuclide removal from solutions was demonstrated. [118]

In this chapter, we discuss physicochemical aspects of isolation, encapsulation, and adhesion of organic and inorganic micro-objects on planar and microstructured surfaces using drop-cast GO membranes. We demonstrate the capabilities of this technique on a variety of solid, liquid, and gaseous samples, such as nanowires, nanoparticles, micro-droplets, bubbles, and microorganisms. We show that SEM, AES, fluorescence and Raman spectroscopies can be successfully applied to image and analyze the encapsulated objects through the formed membrane.

2.2 Fabrication of GO membranes by drop casting

The encapsulation of micro-objects *via* drop-casting of GO aqueous solutions compatible with optical and HV SEM (and SAM) studies has two related aspects:

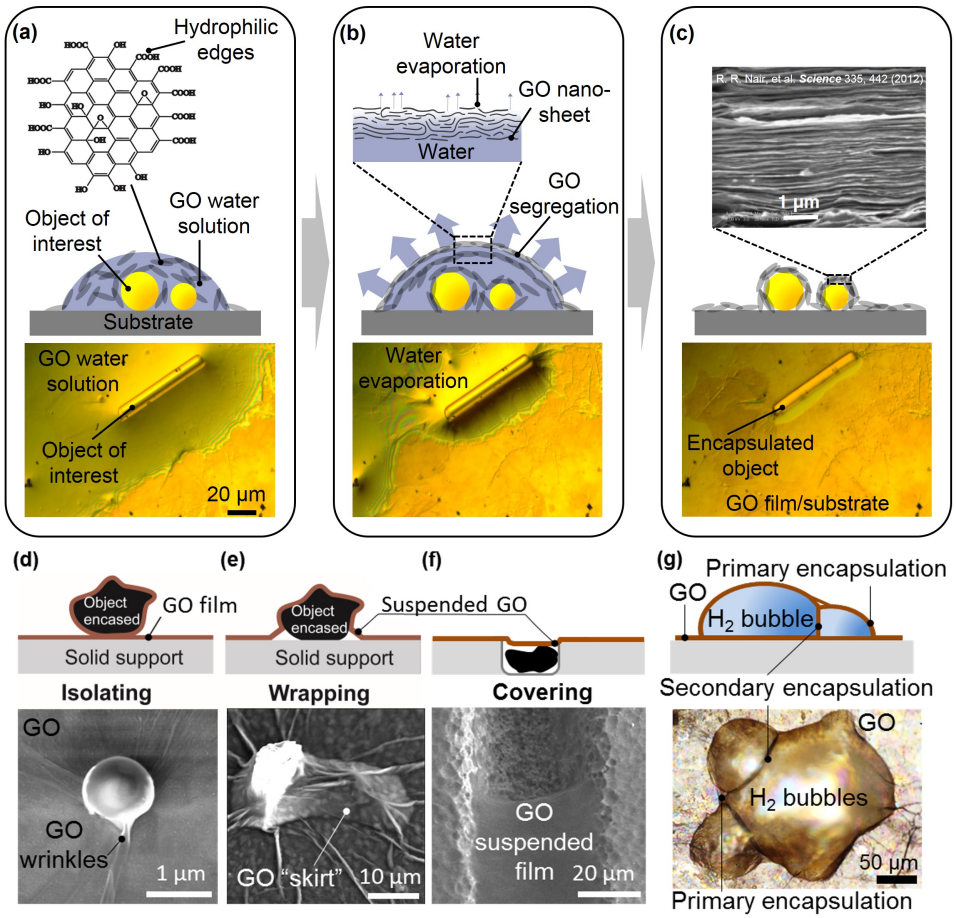

Figure 2.1: Graphene oxide encapsulation. (a) Graphene oxide aqueous solution is drop cast onto the object on the substrate. Graphene oxide flakes with hydrophilic end-groups and hydrophobic basal sites are homogeneously distributed in the droplet. (b) Graphene oxide flakes segregate at interfaces with following water intercalation and evaporation through the newly formed membrane. (c) Once water completely evaporates, graphene oxide film completely encapsulates the core object. The inset SEM image shows the cross-section of graphene oxide film. [44] (d) Three regimes of encapsulation: complete encapsulation of a polystyrene microparticle is manifested by the presence of a narrow "neck" connecting the objects to the surface. (e) Wrapping of a SnO_2 microparticle: only top part of the object is in direct contact with the film. Empty "pockets" remain under the membrane along the perimeter of the sample. (f) SEM of a trench in a glass substrate covered with the film. (g) Drying of the membrane leads to primary and secondary encapsulation of micro-objects: an optical micrograph of encapsulated hydrogen bubbles.

(i) the process of membrane formation and object encapsulation during the droplet drying and (ii) optical and electron imaging and spectroscopy through the membrane. Both aspects are discussed separately below taking into consideration the effect of the encapsulating membrane on the samples final morphology as well as on the imaging conditions and spectroscopic analysis.

Sample preparation:

GO solution was fabricated according to standard Hummer's method followed by dispersing in water *via* sonication to obtain homogeneous suspension. [44,45,123,148] Different concentrations of the solution ($0.02\,\mathrm{kg/m^3}$ – $1\,\mathrm{kg/m^3}$) were used to tune the thickness of the drop-cast membranes. SiO_2/Si wafers and different metal substrates were employed as solid supports for objects of interest. To study the effect of wetting on encapsulation dynamics, the surface was functionalized with a hydrophobic silane. Besides planar substrates, microchannel arrays made of a boron doped silicate glass were used. Polydimethylsiloxane (PDMS) microparticles were synthesized using microfluidic setup. [149] PDMS micro-posts were created using standard photolithography base approach to fabricate elastomeric stamps for soft lithography. Water fleas (*Daphnia*) were transferred on a Si substrate with micropipette from culture liquid. The laboratory strain of *Escherichia coli* (*E. coli*) bacteria and grass pollen followed a similar encapsulation by drop casting procedure. All experiments involving biological samples: *Daphnia*, *E. coli* bacteria, and grass pollen were conducted at the SIUC campus.

The drying of colloids is an active field of research on its own, [150] which

remains largely unexplored for ultra-high aspect ratio discotic particles. [129] The process of encapsulation during slow evaporation of colloid droplets qualitatively proceeds *via* the following steps: (i) the membrane formation, (ii) solvent evaporation, and (iii) membrane drying. Once the diluted water solution is drop cast onto a nanoscopic or microscopic object on a substrate, the sample and the part of the substrate become submersed in homogeneous GO solution inside the droplet (Figure 2.1 (a)). At low initial mass concentrations (w_{GO} from 0.05 g/g to 0.1 g/g), amphiphilic flakes slowly diffuse and segregate at all accessible liquid-gas, liquid-liquid or liquid-solid interfaces (Figure 2.1 (b)). During water evaporation, the concentration of GO inside the droplet and at interfaces steadily increases. As it has been shown, [129–132] at concentrations exceeding $w_{GO} = 0.5\,\mathrm{g/g}$, the colloid experiences a transition from a disordered isotropic liquid phase to an ordered phase similar to the one observed in nematic liquid crystals. This takes place predominately at the interfaces resulting in formation of lamella-like precursor membranes. On a molecular level, these precursor membranes consist of overlapping sheets with water filled percolating capillary network formed by polyaromatic domains. This network is responsible for facile unidirectional water transport from the interior of the droplet to the ambient. [44,134] As it has been shown recently, the interlocking between the flakes is greatly enhanced when traces of multivalent metal cations are present in the solution. [151] The thickness of the nematic membrane increases until complete solvent evaporation, and the object becomes encapsulated. At the last stages of the membrane drying, the interlayer water evaporates, which is manifested by sudden changes in the optical properties and stress development in the membrane (see

discussion below). Some amount of intercalated water remains inside of the membrane [152] and can be desorbed only upon moderate (120 °C to 150 °C) annealing. As a result, the sample and surrounding substrate become covered with a robust laminate-like film, which has a nearly uniform thickness (Figure 2.1 (c)). [59, 153] This is quite opposite to the commonly observed "coffee-ring" effect in drying colloids [154] and can be explained by a significant interaction between the 2D flakes and their hampered diffusion during the nematic phase of a drying droplet. Apparently, the final thickness of the formed membrane, h, depends on the initial concentration C_{GO} (in kg/m^3) of flakes in the solution and the cumulative area of covered surfaces, S:

$$h \approx \frac{C_{GO} V_L}{S \rho_{GO}}. \tag{2.1}$$

Here V_L and ρ_{GO} stand for initial volume of the GO droplet and final density of the dried membrane, respectively.

Depending on the initial object and substrate topography, one can distinguish between three different encasing types: (i) when the solid sample has a small contact area with the substrate, the film encapsulates the item conformly (Figure 2.1 (d)), and a complete "isolation" takes place. The complete isolation routinely occurs around solid grain-line objects or ones resting on hydrophobic surfaces where the interaction between the layer and the object dominates over the GO adhesion to the substrate. In the latter case, the drying membrane can slide over the substrate.

Alternatively, when the solution wets the sample, the drying edge of the forming membrane becomes pinned to the substrate (Figure 2.1 (e)). This pinning front propagates from the periphery of the droplet toward the object upon drying, and the object becomes covered with the membrane having a characteristic suspended film around it. The formation of the suspended film implies that a partial interlocking between the individual flakes in the membrane takes place even before complete drying. Finally, when a solid object, gas bubble or water-immiscible liquid is confined inside a meso- (micro) pore or trench, the drying of the solution leads to the formation of a membrane, which covers the pore or trench (Figure 2.1 (f)). The stability of the suspended membrane depends on the interplay between the capillary forces, the pressure differential (see below) and the mechanical stiffness of the membrane over the cavity. Figure 2.1 (f) shows a trench partially covered with the membrane. The above scenario describes the membrane formation at the water-air interface and defines the so-called primary encapsulation. However, when the droplet contains multiple micro-objects with inner liquid-solid, liquid-liquid or liquid-gas interfaces, a secondary encapsulation may take place at those interfaces [125] (Figure 2.1 (g)). To substantiate this point, optically transparent objects can be used. For that, three hydrogen bubbles were produced in GO water solution by electrolysis (Figure 2.2). GO aqueous drop was placed on top of two Pt electrodes (Figure 2.2 (a,b)), and a DC electrolysis was initiated (Figure 2.2 (c)). Figure 2.1 (g) illustrates that both primary and secondary encapsulating membranes were formed at the air-GO solution and hydrogen bubble-solution interfaces, respectively.

Several effects that occur during the encapsulation process can strongly influ-

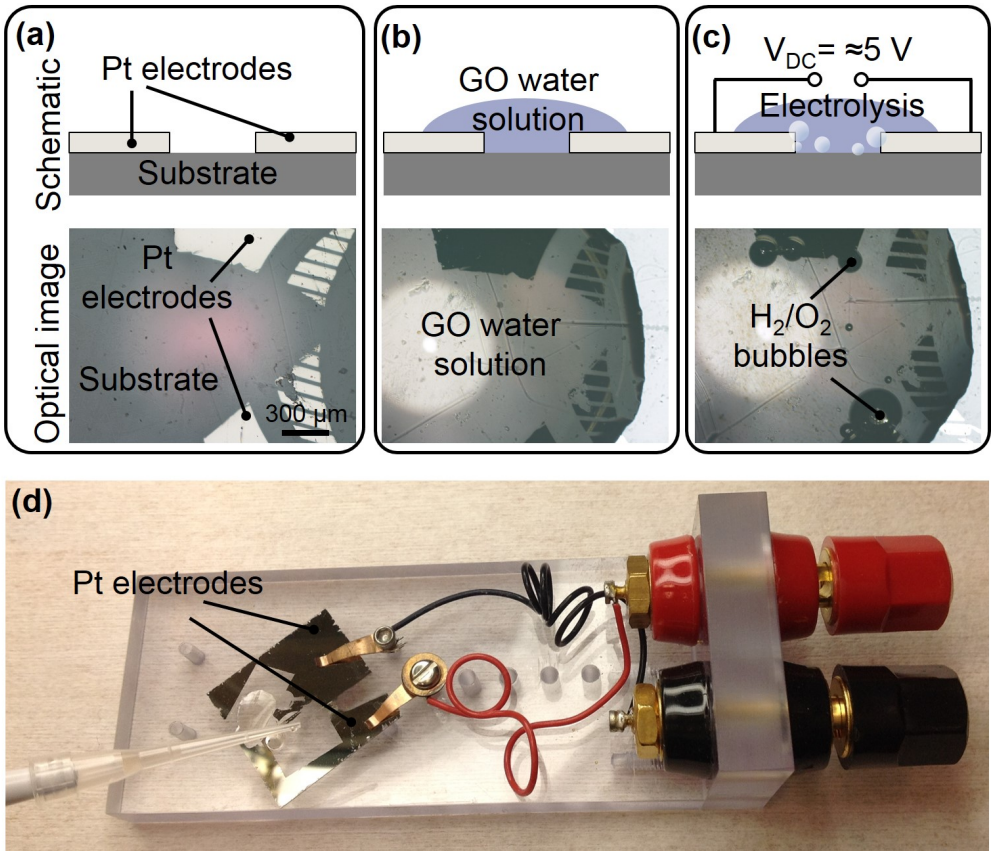

Figure 2.2: Hydrogen bubble synthesis in graphene oxide aqueous solution by electrolysis. (a) Two Pt electrodes deposited onto a glass slide. (b) Graphene oxide aqueous solution is drop cast onto electrodes. (c) 5 volts of DC are applied between Pt electrodes resulting in H_2/O_2 bubble growth at electrodes. (d) Photograph showing the entire setup.

ence the final morphology of the encased objects. The main one is the buildup of the pressure differential between the ambient and encapsulated volume upon water evaporation. This pressure differential leads to contraction of the film around the object, complete wrapping around it and its deformation. There are two major origins of this effect. Firstly, a newly formed membrane is highly permeable to water molecules, and the solvent easily evaporates from the membrane covered droplet. On the other hand, the opposite diffusion of atmospheric gases is impeded. Thus, the residual gas pressure inside the shrinking encapsulated volume becomes reduced to saturated water vapor pressure ($\approx 3.2 \times 10^3$ Pa at room temperature) while the outside pressure is about 10^5 Pa. In fact, the unidirectional flux of water content acts as a vacuum pump on the encapsulated volume similar to a "vacuum storage

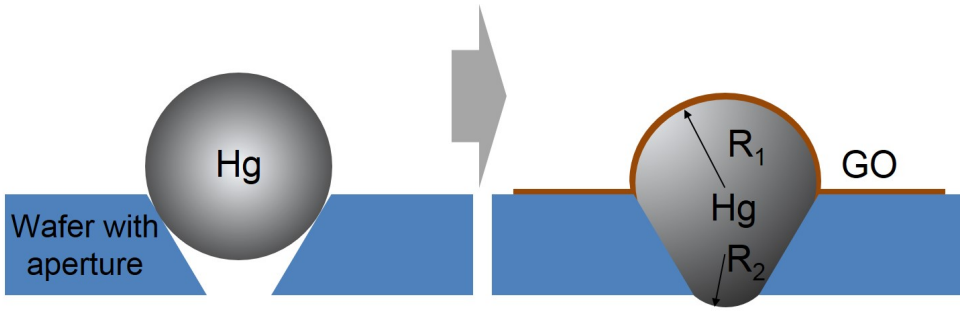

Figure 2.3: Schematic of the experiment to estimate the pressure induced by graphene oxide membrane on a liquid incompressible object. The pressure balance can be described as $\frac{2\gamma_{GO}}{R_1} + \frac{2\gamma_{Hg}}{R_2} = \frac{2\gamma_{Hg}}{R_2}$, where γ_{GO}, γ_{Hg} stand for the effective surface tensions of graphene oxide and Hg correspondingly; R_1 and R_2 are radii of drop curvatures from wide and narrow sides of the conical aperture, respectively. Measuring R_1 =268 μm, R_2 = 100 μm and taking γ_{Hg} =0.487 N/m, we obtain γ_{GO} =0.816 N/m and pressure differential across the membrane $\Delta p = \frac{\gamma_{GO}}{R_1} \approx 4 \times 10^3$ Pa. Therefore, the tensile stress applied to the 138 nm thick membrane is equal to 5.9 MPa.

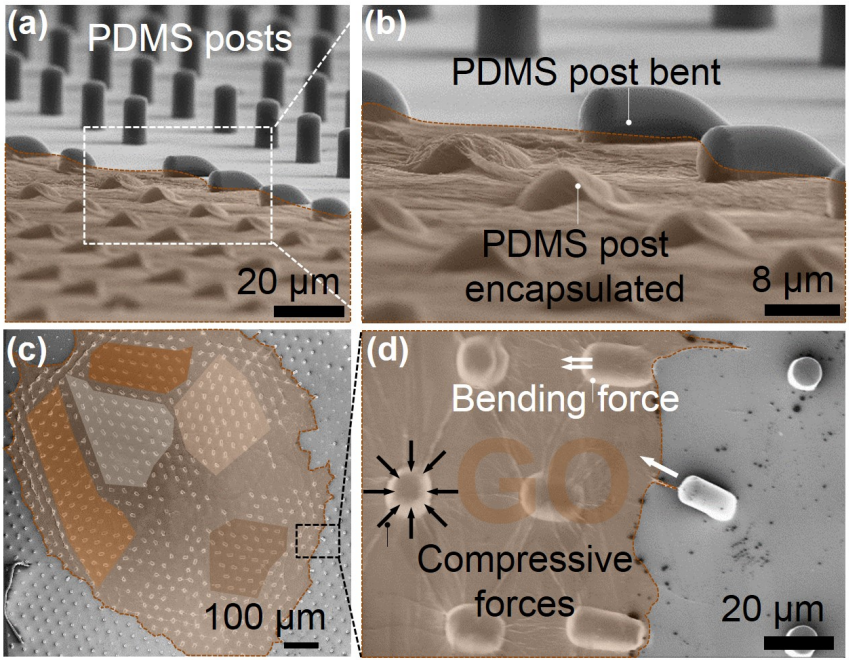

Figure 2.4: Interaction of a PDMS micro-post array with a membrane. (a-b) Side and (c-d) top views of graphene oxide encapsulated (pseudo-colored) and pristine PDMS posts, respectively (SEM micrographs). Shadowed regions in panel (c) show different orientation of encapsulated micro-posts.

bag" principle. Secondly, during the latest stages of encapsulation, a significant portion of water intercalated between GO stacks evaporates, leading to membrane's appreciable shrinkage and an increase of its elastic modulus.

The measurements of the membrane induced pressure differential showed that it does not exceed 10^5 Pa in most of the encapsulating cases reported here (Figure 2.3). To visualize the forces acting on a sample and a substrate during drying of the solution, we monitored the encapsulation of an array of easily bendable PDMS micro-posts (Figure 2.4). The elastic properties of an individual PDMS post are well studied and allow one to detect bending and compressive forces as small as ≈ 1 nN. [155, 156] The typical strain maps (Figure 2.4) indicate the traction forces acting on samples located close to the edge of a drying drop due to initial pinning of the edge and shrinking of the membrane upon drying. Further away from the edge, the drying pattern becomes more symmetric, and compressive forces affect the interior objects. The strain map, however, is not homogeneous on the millimeter scale but consists of a net of domains with different traction directions.

2.3 Physical properties of graphene oxide membranes

The integrity of the encapsulating membrane as well as the resultant shape of the object strongly depend on the sample size, its mechanical properties, and GO adhesion to the substrate. Below, we provide several examples of encapsulation showing the applicability of this technique to a variety of objects of different nature.

We first tested nanoparticle opals [157] as a model of a solid undeformable

object for the encapsulation. [104] A diluted solution of polystyrene nanoparticles (1 μm in diameter) was drop cast and dried on a cover glass pre-coated with Au film (Figure 2.5 (a)). A typical formation of the opal structure with a characteristic "coffee-ring" effect was observed. [154] After formation of a microparticle array, the GO-solution was drop cast on top. On drying, a typical wrapping topography of the membrane along with characteristic wrinkles and a peripheral suspended film around the solid object is observed (Figure 2.5 (a)). The suspended film is pinned to the object and the substrate and experiences about 10^5 Pa pressure differential. The tension applied to the object under the membrane is limited by the membrane's tensile strength that can reach 120 MPa [123] until it disrupts. As a result, a significant compression of the object under membrane can occur, promoting the close packing ordering of the microparticle array at the Au surface. A completely different encapsulation scenario was observed when nanoparticles and GO colloids were mixed together. The presence of immobile flakes in the nematic phase of the solution drastically impedes the mobility of the colloid microparticles inside the drying droplet. The result showed a strong suppression of the long range close pack ordering.

GO encapsulation of immiscible liquids on a solid substrate represents another interesting class of practically important deformable objects [104] demonstrating very different results as compared to encapsulated solid objects. As a model system, we used mercury that has poor wettability to most interfaces due to its high surface tension, leading to the well-known challenges in collecting toxic Hg spills. The contact angle between mercury and naturally oxidized aluminum is about 140 °, [158] resulting in an almost perfect spherical shape of a Hg drop on the substrate (Fig-

ure 2.5 (b)). However, when the mercury drop is encapsulated, its shape becomes distorted with a significant reduction in the contact angle ($\approx 72^\circ$ in our case; Figure 2.5 (c)). The mechanism behind this "wetting" behavior is depicted in Figure 2.5 (e). As described in section 2.2, water surrounding the Hg droplet gradually evaporates through a permeable membrane. Thus, a membrane adheres to the substrate from edges toward the center until the film reaches the uppermost point of the Hg droplet (the central panel in Figure 2.5 (e)). At this moment, the liquid mercury starts deforming due to tension forces induced by the drying membrane and atmospheric pressure differential. Since the mercury drop is easily deformable, the initially spherical Hg droplet accepts a "pseudo-wetting" shape. Therefore, in contrast to the encapsulated solid items, deformable objects can mediate the pressure differential *via* changing their shapes during drying and without forming empty pockets. Note that this explanation implies strong membrane-substrate adhesion along the contact line of the membrane with naturally oxidized aluminum substrate. Thus, the compression and shape of the encapsulated object can be controlled *via* tuning the membrane-substrate interaction. To validate this hypothesis, we reduced adhesion between the membrane and substrate by functionalizing the substrate with a hydrophobic coating. The resulting shape of a Hg droplet became significantly less affected by the membrane in this case (Figure 2.5 (d)) since the membrane is not pinned to the support anymore but slides over the hydrophobic surface. It results in conservation of nearly-spherical Hg droplet shape with a simultaneous increase in the number of wrinkles and thickness of the film that is in a good accordance with equation 2.1.

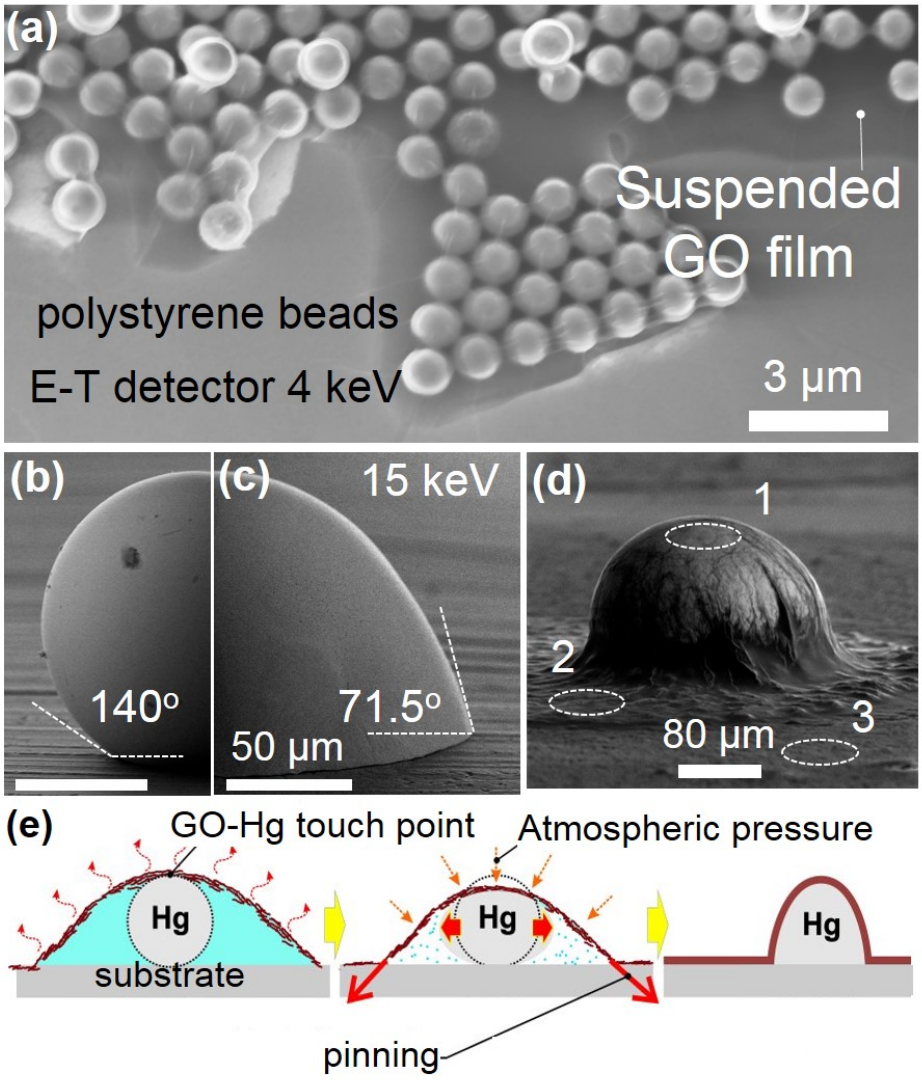

Figure 2.5: Graphene oxide encapsulation of polystyrene microparticles and mercury microdroplets as models of solid and liquid samples, respectively. (a) An array of encapsulated ordered polystyrene microparticles. SEM images of (b) uncovered and (c) an encapsulated mercury microdroplet on an aluminum substrate acquired at E_b=1 keV and 15 keV, respectively. (d) A Hg drop encapsulated on a chemically functionalized substrate at E_b=15 keV. Regions encircled with white dashed contours correspond to collected spectra in Figure 2.9 a. (e) GO-mercury interaction during encapsulation (from left to right): the film reaches and touches the top of Hg drop; Hg drop deforms due to the tension forces exerted on the film by atmospheric pressure; the film completely encapsulates the drop once water entirely evaporates.

Encapsulation of the biological objects is particularly important for histological and forensic applications. Graphene coating was previously used for non-destructive electron microscopy imaging and analysis of biological samples. [159–162] Here, we apply GO encapsulation to exemplary biological objects and microorganisms, such as pollen grains, *Daphnia*, and laboratory strains of *E. coli* bacteria (Figure 2.6). The encapsulated grass pollen (Figure 2.6 (a)) has a characteristic collapsed morphology, which is commonly observed during cellular dehydration. GO encapsulation also enables reliable adhesion of the bio-samples to the substrate. According to our classification above (see Figure 2.1 (d-f)), the observed encapsulation corresponds to a complete isolation since GO folds and wrinkles are distinctly seen at the very base of the pollen grain. Significantly larger hydrated organisms such as *Daphnia* experienced even higher degree of compression during the encapsulation. This is due to combined effect of dehydration and tension forces appearing in a drying membrane (Figure 2.6 (b)). The morphological instabilities induced by the encapsulation can be considered as a drawback compared to standard CO_2 critical point drying technique. However, the advantage of the current method stems from the selective permeability of the membrane to water molecules. Therefore, the entire chemical content of the micro-object (except water) is preserved, which can be a decisive factor for forensic practices.

Other application where an encapsulation can be essential is the isolation of pathogenic bacteria. This can be realized simply by spraying or spilling GO solution over the hazardous areas. To demonstrate the feasibility of this method, we have made side by side comparison of the areas containing untreated and encapsulated

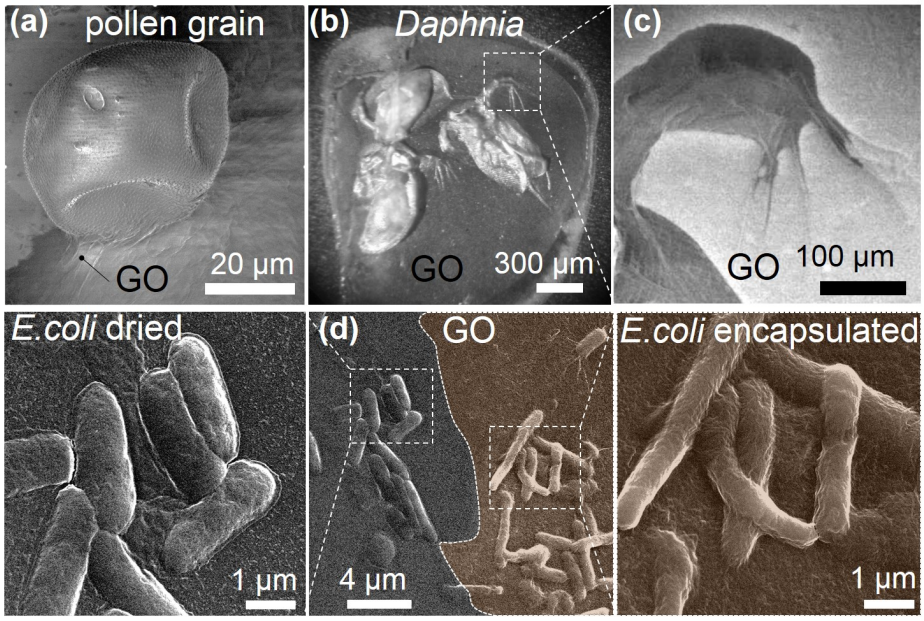

Figure 2.6: Encapsulated bio objects. (a) A pollen grain. The SEM image collected at 1 keV. (b) *Daphnia* (water flea) optical image. (c) The magnified SEM image (1 keV) of graphene oxide encapsulated antennae. (d) Comparative SEM (10 keV) imaging of vacuum dried (left panel) and encapsulated (right panel) *E. coli* bacteria. The central panel represents the border between these two regions.

E. coli bacteria. The border region between the untreated and encapsulated bacteria was imaged with SEM (Figure 2.6 (d)). A direct comparison of the pristine (Figure 2.6 (d) left panel) and encapsulated (Figure 2.6 (d) right panel) bacteria shows that the pristine samples do not preserve their shape and become flattened releasing their intracellular materials upon vacuum dehydration. On the other hand, the structure of the encapsulated bacteria is largely preserved by the membrane under the same conditions. In addition, it has been shown that the GO encapsulant not only immobilizes *E. coli* bacteria at the surface but also exhibits strong antibacterial activity. [147]

The last two encapsulation examples underline the role of the sample shape and size on the encapsulation scenario and membrane induced compression. Symmetric micro-objects such as bacteria tend to be conformly coated with GO and, therefore, experience minor pressure differential mostly induced by membrane shrinkage upon drying. On the contrary, encapsulation of sub-millimeter samples with multiple protruding features (such as *Daphnia*) proceeds with creation of the numerous empty pockets under the membrane. The membrane experiences an additional tensile stress over these pockets which, in turn, leads to elevated compression.

2.4 Analysis of encapsulated objects: SEM, EDS, Auger, Raman and fluorescence

There is a great interest in the development of encapsulation techniques, compatible with high-resolution microscopy and spectroscopy, which would not require

traditional procedures such as fixation, staining, freezing or critical point drying. Unlike the common embedding media used in histology, the ultrathin GO film offers a unique possibility for imaging and probing the encased objects directly using the standard SEM (or TEM) without time-consuming microtoming, sectioning, and other histological procedures. The key advantage is that the membrane thickness can be tuned such that it becomes largely transparent to electrons in a wide range of electron beam energies. In this section, we discuss the influence of the membranes on SEM signal attenuation as well as spatial resolution and comment on the optimal imaging conditions using several examples. Electron beam generates low energy SEs and higher energy BSEs upon inelastic and elastic collisions with GO coated sample.

To evaluate the influence of the coating on SEM imaging, we conducted comparative Monte Carlo trajectory simulations [163] for 10 keV electron beam probing: (i) high atomic number (Z) metal (Hg, 201 u), (ii) liquid droplet (CH_3OH, 32 u), and (iii) gas bubbles (10^5 Pa Ar, 40 u) with and without a 50 nm thick GO coverage (Figure 2.7 (a)). The interaction volumes at 10 keV electron beam energy for the materials covered with a membrane and without coverage are depicted at the left and right halves of each panel, respectively. The parametric Kanaya-Okayama expression 1.2 for electron beam range [164] predicts R_{KO} =0.38 μm and R_{KO} =9 μm for Hg and methanol droplets, respectively. As can be seen, a 50 nm thick membrane does not profoundly affect the interaction volume in mercury and methanol and it is primarily due to low scattering of electrons in GO and much higher Z number of the host materials. The contribution of the membrane to electron scattering becomes, however, dominating in the case of gaseous samples (Figure 2.7 (a), right panel) due

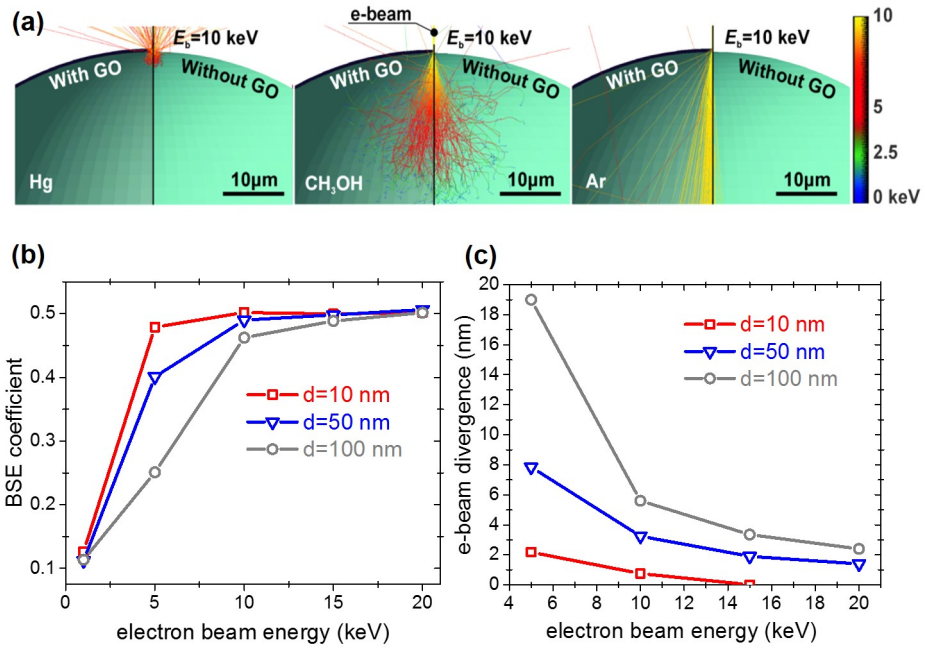

Figure 2.7: (a) Monte Carlo simulations of electron scattering in liquid Hg drop of 13.5 g/cm^3 density (left), liquid methanol of 0.79 g/cm^3 density (center), and argon bubble of 1.7×10^{-3} g/cm^3 density without the membrane (right-half of each panel) and encapsulated with a 50 nm thick graphene oxide film (left side of each panel). (b) BSE coefficient vs. electron beam energy calculated for a Hg drop encapsulated with a 10 nm, 50 nm, and 100 nm thick film. (c) Calculated divergence (in nm) of the electron beam scattered by 10 nm, 50 nm, and 100 nm thick film as a function of primary electron energy.

to a three orders of magnitude reduction in the density compared to solid or liquid encapsulated sample.

Figure 2.7 (b) depicts the variation of the BSE coefficient (the number of elastically scattered BSEs electrons per a PE) of a GO covered Hg droplet as a function of electron beam energy for three different thicknesses of the membrane. The BSE coefficient is relatively small for the 50 nm and 100 nm thick coatings, and the interaction volume is mostly confined within the shell when the PE energy E_b is low. Under these conditions, the image mainly contains surface topographical information. With E_b increase, the interaction volume increases with a dominant contribution to BSE coefficient from the core material. Contrarily, relatively thin film, *e.g.* 10 nm, is highly transparent to PE beam at 5 keV electron energy; thus, BSE is dominated by the high-Z Hg encapsulated interior. In summary, for electron beam energies of 10 keV and above, the BSE coefficient is nearly independent of the membrane thickness if it is less than 100 nm. At lower electron energies, the attenuation of the BSE signal by the membrane becomes noticeable and strongly depends on the film thickness. The latter may be used to image the completeness of the coverage of high-Z materials. Figure 2.7 (c) shows the calculated divergence of 10 nm wide PE beam propagating in a gaseous medium after passing the membranes of three different thicknesses. The cross-sectional region containing 68% of TEs was used as an effective beam diameter. [33] Apparently, the divergence of the beam grows with increase of the film thickness and reduction of PE energy, affecting the ultimate resolution achievable on the encapsulated objects.

Imaging:

An optical microscope and field emission SEM were employed to observe the encapsulation process and final products. The electron beam energy and type of an electron detector were varied to gain the desired contrast of encapsulated objects. Electron trajectory simulations were calculated by means of Monte Carlo simulation package. [163] To perform STEM, specimens were placed onto a 50 nm thick polyimide TEM grid. The latter was mounted on a carbon STEM holder with Au covered plate facing E-T detector. Electrons transmitted through the sample produced the image formed by a SE signal scattered from the gold surface. Therefore, the image could be created concurrently by either conventional SE_1 scattered from the specimen and collected by through-the-lens (TTL) detector or by transmitted signal resulting in SE_2 and analyzed by E-T detector.

To experimentally validate the simulated results, we imaged the coated SnO_2 whiskers and hydrogen bubbles at different SEM settings. Figure 2.8 (a) and (b) show two images of the same area recorded using surface sensitive and bulk sensitive imaging conditions, respectively. Under these conditions, low-energy e-beam and a SE sensitive TTL detector reveal mostly the surface topography of the film covering the SnO_2 sample (Figure 2.8 (a)) while the high-energy e-beam in conjunction with the BSE detector probes the interior of the encased object through the membrane (Figure 2.8 (b)). High electron transparency of the GO coating to the outgoing BSEs enables detection of even small diameter SnO_2 nanowires (Figure 2.8 (b)) that were completely invisible beneath the membrane (Figure 2.8 (a)) when lower electron energies were used.

Gaseous samples provide an ideal platform to quantify the attenuation and scattering of the electron beam during SEM imaging of the encapsulated objects. For that, a microchannel plate (MCP) was used as a substrate with sharp topographical features and high SE yield surface suitable for resolution tests. A GO solution was drop cast onto MCP microporous surface followed by oxygen or hydrogen bubbles generation beneath the membrane. In agreement with prior Monte Carlo simulations, Figure 2.8 (c-f) demonstrates a gradual decrease of electron scattering by the thin encapsulating membrane resulting in an increase of electron transparency of the membrane and lateral resolution of the underlying substrate with electron energy.

Besides SEM imaging, GO electron transparent films open exciting avenues for spectroscopic analysis of encapsulated samples. Figure 2.9 (a) shows EDS spectra taken at different locations: (1) on a Hg drop covered with the membrane, (2) Al substrate covered with the same film, and (3) pristine Al substrate (see Figure 2.5 for details). Despite a thick membrane, these spectra demonstrated the feasibility of EDS elemental analysis of encapsulated objects.

AES spectroscopy:

For AES, the samples were admitted to an UHV analytical chamber using standard load-lock system. No additional cleaning or baking procedures were undertaken. Auger electrons were excited by a 3 keV PE beam and collected at takeoff angle close to normal to the sample surface. Hemispherical electron energy analyzer was set to 100 eV pass energy.

In a different experiment, differential AES were acquired comparatively from

two adjacent GO-covered (blue curve) and uncovered (red curve) areas of a SnO_2 whisker (Figure 2.9 (b)). As expected, the carbon C_{KVV} Auger peak dominates the spectrum from the covered area, however, a strongly attenuated tin Sn_{MNN} signal can still be recorded. This result is somewhat surprising since the average thickness of the membrane is expected to be more than 10 nm based on the concentration of the solution and the droplet size.

The standard attenuation equation [165]:

$$\frac{I_{Sn}}{I^0_{Sn}} = exp(\frac{-d}{\lambda_{MNN} \cdot cos\phi}). \tag{2.2}$$

where d is the thickness of the GO layer, λ_{MNN} is Sn_{MNN} electron attenuation length in GO layer, and ϕ is the take-off angle (25 °), allows estimating the thickness of the membrane *via* given peak-to-peak intensity ratio of the Auger Sn_{MNN} signal from pristine and covered areas. The recorded ratio corresponds to the thickness of just one or two monolayers. The observed discrepancy requires further investigation and is presumably a result of electron beam induced chemical reduction of the membrane under intense irradiation. [166] Despite the possible GO electron beam induced local decomposition, the spectra demonstrate the possibility to obtain fine chemical information for analytical purposes from an encapsulated object using standard electron spectroscopy.

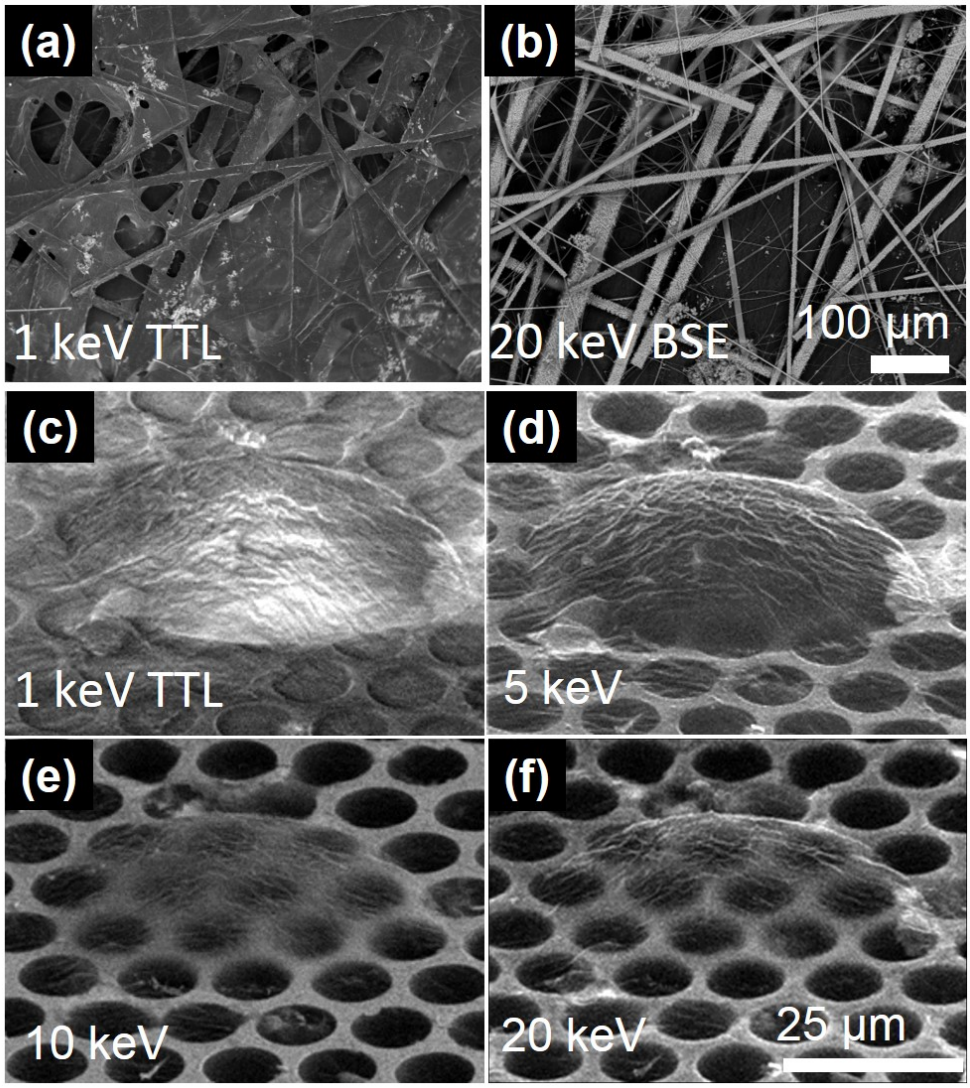

Figure 2.8: Electron transparency of graphene oxide membrane and e-beam divergence. (a) SEM image of encapsulated SnO_2 whiskers obtained using secondary electron sensitive TTL detector and low energy electron beam E_b =1 keV. (b) The same object imaged using BSE detector and E_b =20 keV. (c-f) The evolution of membrane transparency with electron beam energy *via* imaging of the same encapsulated H_2 bubble at E_b=1 keV, 5 keV, 10 keV, and 20 keV.

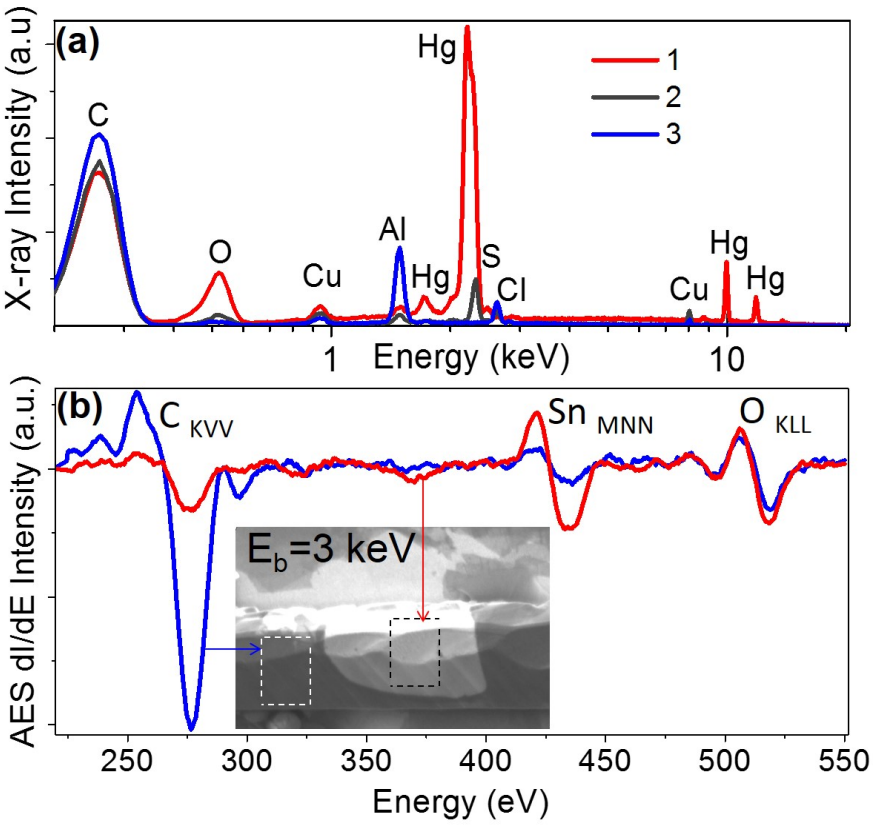

Figure 2.9: Electron spectroscopy through a thin graphene oxide membrane. (a) EDS spectra marked as 1, 2, and 3 are collected from graphene oxide encapsulated Hg microdroplet (E_b=15 keV), Al substrate covered with graphene oxide film, and Al substrate shown in Figure 2.5 (d), respectively. Al, C, and O peaks originate from Al substrate. (b) Differential AES (E_b=3 keV) collected from pristine SnO_2 (red curve) and covered areas (blue curve).

2.5 Optical transparency and Raman spectroscopy

Optical microscopy and spectroscopy are major tools for materials science, forensics, and biomedical research. Transparency of thin-film GO membranes not only to electrons but also to optical photons enables facile fluorescence and Raman analysis of the encapsulated materials. To demonstrate this, we used fluorescent polystyrene microparticles, which are common in drug discovery, phagocytosis, and microfluidic studies and serve as good model objects for encapsulation tests.

Raman spectroscopy:

The Raman spectra were collected using a Raman microscope with a 532 nm excitation laser. Laser power was set to 2 mW. We used 25 μm slit aperture and 50$\times$ objective. The estimated spot size was 2.1 μm.

Figure 2.10 (a) and (b) show images of the same area containing fluorescent microparticle deposit recorded using an optical microscope operating either in the bright field or fluorescence imaging modes. A white dashed line in Figure 2.10 (b) demarks the border between the encapsulated and pristine arrays of particles. In contrast to prior observations [167] where GO was used to quench surface fluorescence, only a minor attenuation of the fluorescence signal from microparticles was observed in our experiments. This is due to the high optical transparency of the membrane for the 480 nm to 550 nm emission band [168] and the bulk doping of polystyrene microparticles with a dye.

An example of Raman spectroscopy through a membrane is shown in Figure

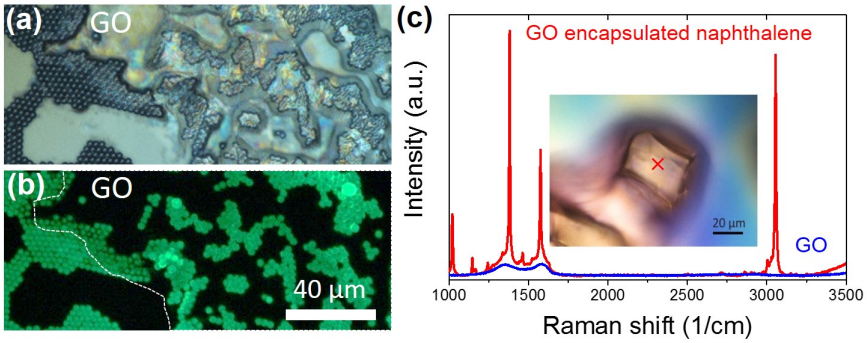

Figure 2.10: (a) The bright field and (b) fluorescence microscopy images of an array of fluorescent 4 μm in diameter polystyrene microparticles partly encapsulated with GO. The white dashed line demarcates the border between the pristine and covered microparticles. (c) Raman spectra of a covered naphthalene grain (red) and pristine graphene oxide film (blue). The Raman signal from naphthalene was collected through an optically transparent film. The red cross in the inset image shows the location where the data were collected.

2.10 (c). Here, a grain of crystalline naphthalene was encapsulated with GO to preserve this highly volatile material. The stability and comparative analysis of the sublimation rates for pristine and encapsulated naphthalene is an interesting problem of its own, which remains beyond the scope of this thesis. The recorded spectrum is a superposition of sharp peaks corresponding to the Raman signatures of naphthalene (red curve) and broad characteristic GO peaks (blue curve). Due to the small thickness, the contribution of the membrane to the cumulative Raman signal is insignificant compared to naphthalene. This experiment exemplifies the feasibility of high-quality Raman analysis through the encapsulating membrane. The latter opens exciting opportunities for analytic forensic applications where preservation of probed materials is required.

Other applications of GO encapsulation

GO encapsulation can find an application as a new method in histology. As an example, the conventional sample preparation for TEM and STEM imaging relies on van der Waals adhesion of the sample to electron transparent supporting membranes or special TEM grids. Alternatively, the samples are often glued or embedded into a polymerized resin block followed by microtoming. [116] However, due to either poor adhesion or incompatibility with glues, resins, toxicity, *etc.*, a large class of samples cannot be easily prepared using aforementioned recipes. Our approach provides a complementing way to snugly attach an arbitrary micro sample to membranes and stencils with a precise control of the film thickness. Figure 2.11 shows an STEM image of *E. coli* bacteria on a 50 nm thick polyimide TEM grid encapsulated by GO

(Figure 2.11 (c)) and uncovered (Figure 2.11 (a)). The Figure 2.11 (b) comprises both encapsulated and non-encapsulated regions. [104] Figure 2.11 (d) exemplifies our approach to fix and image a grass pollen in STEM mode. The symmetrical radial wrinkles visible in a transmission mode prove a complete encapsulation of the pollen on a very thin TEM membrane.

Another potentially important application of this encapsulation technique is X-ray micro-tomography. Usually, to obtain a 3D reconstruction of an object, a set of 2D images of the sample pivoted within a wide range of angles $\pm$ 70 $^\circ$ is recorded. [169, 170] This technique requires mounting the sample on a pivoting axis with an open access for the X-rays in the aforementioned angle range. Currently, the latter raises design challenges in sample mounting. Our approach helps resolve many of impediments *via* attaching a micro sample to the needle-like holder and encapsulating an object of interest by GO (Figure 2.11 (e)). Here, an X-ray transparent GO film serves as both supporting media for the micro sample and the isolation membrane from the ambient environment.

2.6 Summary

In conclusion, we have demonstrated that a wide class of solid, liquid, gaseous micro- and mesoscopic objects can be reliably adhered to a variety of substrates and encapsulated with an electron (and optically) transparent membranes using a simple drop casting method. The thickness of the membrane can be tuned by the concentration of the solutions and the size of the droplet. Different regimes of en-

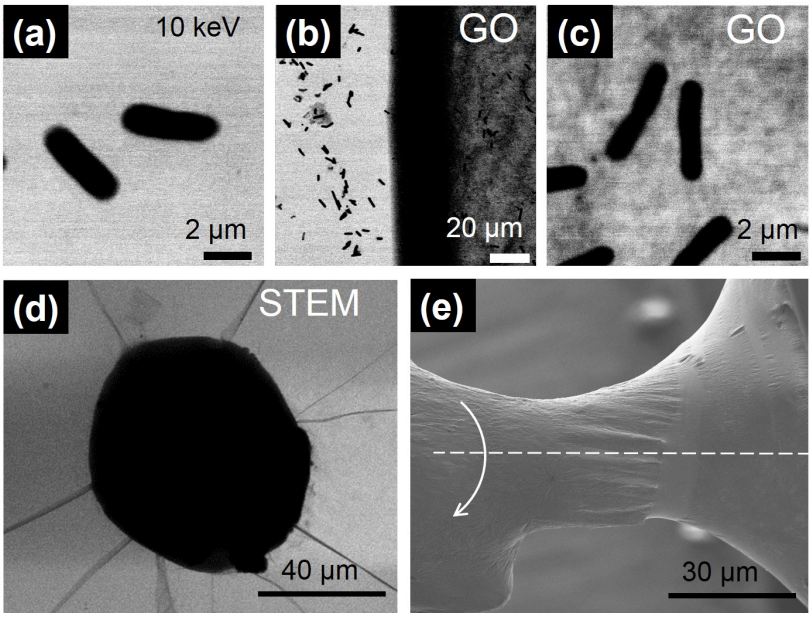

Figure 2.11: *E. coli* bacteria and a pollen grain encapsulated by graphene oxide on a TEM membrane and sample preparation for X-ray microtomography and 3D imaging. Comparative STEM (10 keV) imaging of vacuum dried (a) and left part of (b) and encapsulated (c) and the right part of (b) *E. coli* bacteria. (d) A pollen grain imaged in STEM mode at E_b=20 keV. (e) Liquid Ga neck formed between the needle and a solid surface and wrapped with the membrane. Part of the membrane was torn away (right side) exposing the surface of pristine Ga. The dashed line represents the axis of rotation.

capsulation such as covering, wrapping, and complete isolation of objects can be realized depending on the hydrophobicity and/or topography of a substrate surface. The shape and morphology of encapsulated objects may change upon encapsulation due to pressure differential buildup and membrane shrinkage. This effect is particularly noticeable in the case of soft, deformable, and biological samples.

Due to the low atomic number of carbon and small thickness of the film, it is largely transparent to photons and even to a few keV electrons enabling routine fluorescence, Raman, X-ray, SEM, STEM imaging, and EDS/AES chemical analyses of encapsulated micro-objects through a membrane. Though few monolayer thin membranes can be fabricated, a 50 nm to 200 nm range of the film thickness defines a practical compromise between its mechanical strength and electron transparency in the 5 keV to 30 keV electron energy range. Tight adhesion between the membrane and the sample minimizes electron attenuation and broadening effects in the membrane.

Finally, along with the benefits in performing routine optical, X-ray, and SEM/STEM imaging and analysis, the elemental composition of membranes is favorable for other analytical methods such as flame photometry, mass-spectroscopy methods *i.e.* matrix-assisted laser desorption/ionization (MALDI). This is because destruction of the membrane during analysis leads to simple and easily identifiable molecules such as CO and CO_2. We envision that scalable, inexpensive, and high-yield GO encapsulation will open new routes in histological practices, forensic studies, dip pen-like encapsulation technology and other fields where reliable adhesion and isolation of reactive, toxic/radioactive samples or precious artifacts

is required. Furthermore, the technique can be easily integrated with the modern microelectronic and microfluidic methods and applications.

Chapter 3: Anthracene as a sacrificial layer for clean transfer of CVD-grown graphene

The application of suspended graphene as electron transparent supporting media in electron microscopy, vacuum electronics, and micromechanical devices requires the least destructive and maximally clean transfer from their original growth substrate to the substrate of interest. In this chapter, we use thermally evaporated anthracene films as the sacrificial layer for graphene transfer onto an arbitrary substrate. We show that clean suspended graphene can be achieved *via* desorbing the anthracene layer at temperatures in the 100 °C to 150 °C range, followed by two sequential annealing steps for the final cleaning, using Pt catalyst and activated carbon. The cleanliness of the suspended graphene membranes was analyzed employing the high surface sensitivity of low energy scanning electron microscopy and X-ray photoelectron spectroscopy. A quantitative comparison with two other commonly used transfer methods revealed the superiority of the anthracene approach to obtain larger area of clean, suspended CVD graphene. Our graphene transfer method based on anthracene paves the way for integrating cleaner graphene in various types of complex devices, including the ones that are heat and humidity sensitive. This chapter is adapted from Ref. [107]

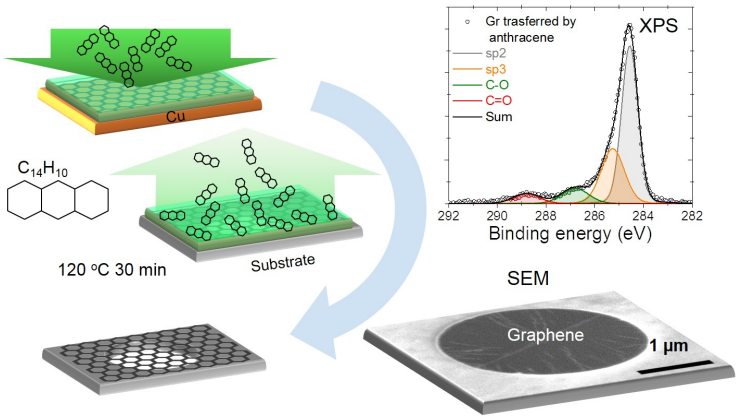

3.1 Motivation

Ultra-thin and clean suspended graphene (Gr) membranes have been applied in a variety of micromechanical devices, [171] sensors, [172] and vacuum electronics; [173] as supporting media for HRTEM, [61] and as electron transparent windows in ambient pressure photoelectron spectroscopy and microscopy. [49] The mechanical exfoliation of the graphite flakes remains the cleanest method to prepare such devices but it is low yield. Alternatively, ultrathin membranes assembled of interlocked chemically exfoliated Gr (graphene oxide) flakes or platelets are simple to fabricate. [59] However, they possess a large number of defects and reactive functional groups. The latter, being advantageous for the development of new composite materials [174] *via* Gr functionalization, can lead to undesirable alteration of the physical and chemical properties of the membrane devices. Conversely, the growth of Gr *via* CVD on copper or nickel substrates is a well-developed, scalable, and a high-yield method of Gr production with large single crystal domain size. [38] In order to transfer Gr from copper or nickel foils onto a substrate of interest, multiple approaches have been implemented, which can be roughly classified into two groups: "wet" and "dry" methods, depending on whether any liquid is involved during the final stage of the Gr layer transfer. For suspended Gr devices, wet transfer methods *via* a sacrificial layer [105, 175, 176] or direct transfer approaches using capillary action of solvent droplets [48] (*e.g.* isopropyl alcohol (IPA)) as an adhesion promoter

are commonly used. The former method usually relies on a PMMA layer spin-coated over the Gr-metal substrate, followed by etching of the metal and transferring the PMMA/Gr onto a substrate of interest. After the transfer, the PMMA layer is dissolved appropriately, or removed by annealing in vacuum [177] or under reducing conditions. [178] Recently, alternative polymer scaffolds, which do not require an additional annealing after the polymers are dissolved, [179] have been used instead of PMMA. However, some of the commonly used copper etchants, such as ammonium persulfate solution (APS), can promote a crosslinking in polymers, resulting in a high concentration of residues on the Gr layer. [106] Alternatively, the direct transfer method is based on an adhesion between a Gr/substrate stack and a flexible perforated carbon membrane induced by capillary forces of a drying solvent such as IPA. [46] In this case, the growth substrate is etched away, and, after rinsing in water and drying, a suspended, high-quality membrane is obtained. Other wet methods of Gr transfer include the soak-and-peel, [180] bubbling transfer, [181] and electrochemical delamination (see Refs. [182–184] for a detailed description of each approach). Dry transfer of Gr is necessary when the substrate of interest is reactive or sensitive to moisture. Solvent-free methods to transfer CVD-grown Gr employ PDMS stamps, [41] thermal release tape, [42] thermal decomposition of PMMA in forming gas, [105] *etc.*

The application of Gr in electron or scanning probe microscopies, microelectromechanical systems (MEMS)/electronic devices, and many other fields requires the ultimate surface cleanliness of the suspended membrane. However, all the transfer methods unavoidably contaminate the Gr surface, requiring a sequential step of

rigorous cleaning. The direct comparison of the reported cleaning methods is challenging to conduct due to the variety of fabrication and characterization techniques used. Therefore, a systematic comparison of the most commonly used methods applied under the same conditions is essential to determine the most effective one. In this chapter, we demonstrate a novel clean method for the transfer of CVD-grown Gr utilizing an anthracene film as a sacrificial layer. Different from higher molecular mass PAHs that strongly interact with Gr, an anthracene film can easily sublime at moderate temperature (< 150 °C), [185] thus preventing structural changes of the Gr and a sensitive substrate of interest. We perform a comparative cleanliness analysis of our approach with two widely used transfer methods: (i) direct transfer by IPA [48] and (ii) PMMA-based transfer. [105] The samples transferred *via* all three aforementioned protocols were subjected to the same two step cleaning procedure after the transfer: annealing in the presence of platinum catalyst [186] followed by annealing in activated carbon. [187] The cleanliness of the resultant membranes was examined with techniques highly sensitive to the surface contamination and defects: low-voltage (1 keV) scanning electron microscopy (LVSEM), XPS, and TEM. We show that Gr transferred using anthracene is consistently cleaner and less defective than samples prepared by other methods.

3.2 Graphene transfer using anthracene

Gr was grown from a methane gas precursor on a copper substrate using the standard CVD method, which is described in details elsewhere. [38, 40, 188]

Briefly, 125 μm thick copper foils electropolished in phosphoric acid were loaded into atmospheric pressure CVD reactor and annealed at 1065 °C under the flow of 2.5% H_2 in Ar for 30 min. Gr growth was performed by addition of methane with a gradual increase of concentration from 10 to 20 and then to 40 ppm for 30 min increments. After cooling down to room temperature, a monolayer of Gr with less than 5% fraction of the hexagon-shaped bilayer was formed on both sides of the copper foil.

The anthracene film was deposited onto a Gr/copper stack by thermal evaporation in an evacuated glass test tube (Figure 3.1 (a,b)). The copper foil with CVD-grown Gr was tightly attached to the copper supporting tube. The copper tube was used for pumping the test tube before anthracene deposition, as well as a cold finger for the substrate. To grow a uniform anthracene film, the copper tube was cooled with liquid nitrogen during the anthracene deposition. The bottom part of the glass tube was filled with 1 mm size anthracene particles (purity $\geq$ 99%), pumped to $\approx 10^{-3}$ Pa, and then immersed into a boiling water bath to evaporate anthracene. After 30 min of anthracene evaporation, 14 μm $\pm$ 7 μm thick layer of anthracene film has been deposited onto the Gr-copper specimen. To avoid water condensation onto the anthracene film upon venting, the glass tube with the sample was constantly evacuated until the temperature of the copper tube and mounted sample reached room temperature.

SEM image in Figure 3.1 (c) shows the anthracene film deposited onto the Gr on a copper substrate. The second layer of Gr is clearly seen as a hexagon. Dense and mechanically stable, quasi-amorphous films were obtained if the deposition was

conducted onto a pre-cooled (≈ -20 °C) Gr/substrate in vacuum (Figure 3.2 (c,d)). Note that low temperature of a substrate is essential to increase the density of the nucleation sites for anthracene. The film deposited onto a substrate at room temperature tends to form an incomplete film of weakly bound crystallites as large as few tens of μm (Figure 3.2 (a,b)). Capillary forces can easily destroy such a sacrificial layer during wet copper etching, which would make the transfer problematic.

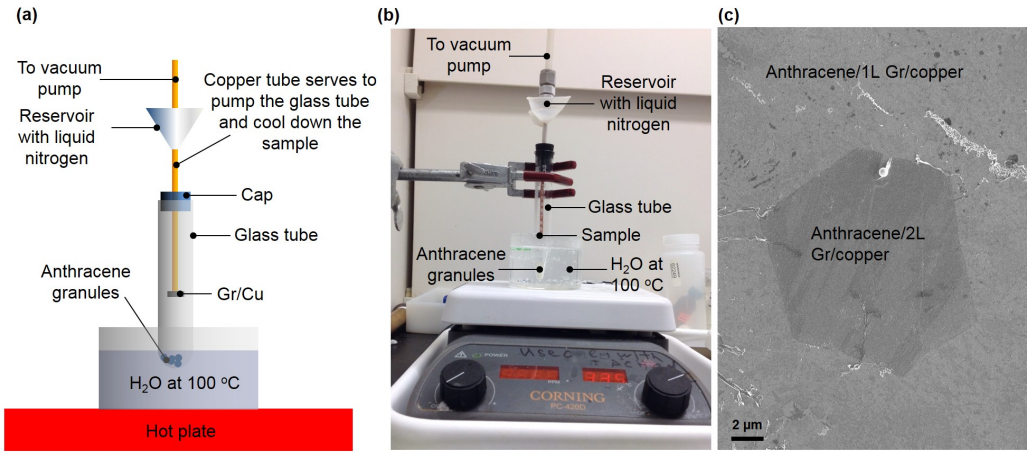

Figure 3.1: Anthracene deposition onto graphene CVD grown on a copper substrate. (a) Schematic and (b) photo of the deposition setup. (c) SEM image of an anthracene film thermally evaporated on Gr/copper at ≈ -20 °C. The hexagon in the middle of the image is the island of two-layer Gr. Both single and two-layer graphene are buried under the anthracene film.

After the deposition onto the pre-cooled sample (Figure 3.3 (ii)), the copper substrate was etched in aqueous APS (Figure 3.3 (iii)). The Gr-anthracene stack was then rinsed in distilled water, and transferred directly to the target substrate (Figure 3.3 (iv)). After annealing at 120 °C for 40 min (Figure 3.3 (v)), the anthracene film sublimed, and only the Gr layer was left on the target substrate (Figure 3.3 (vi)).

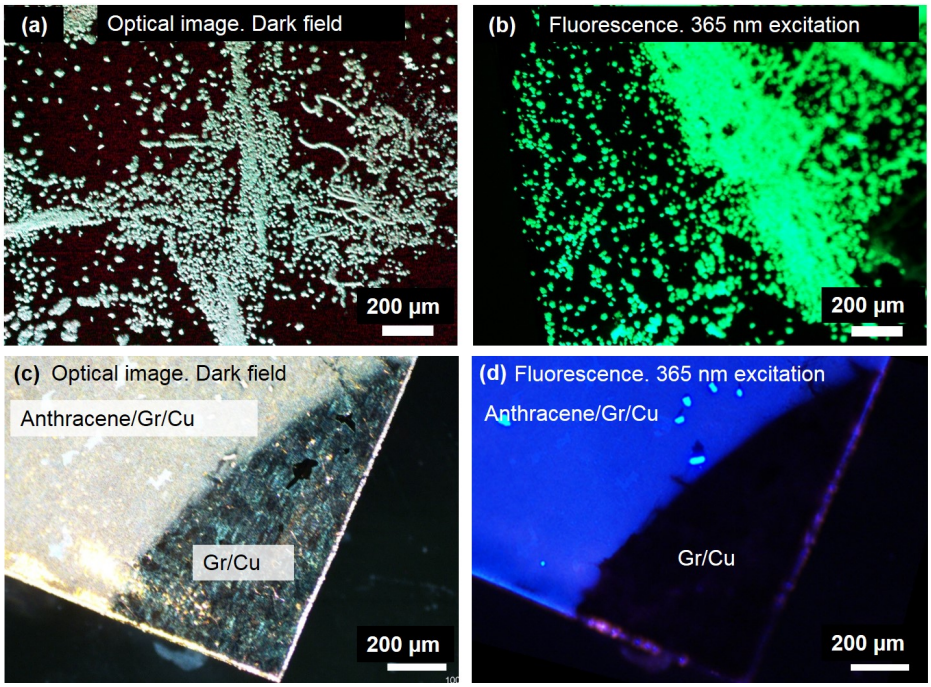

Figure 3.2: The morphology of the anthracene film deposited onto Gr/copper stack. Dark field optical images of a typical anthracene film evaporated onto Gr/copper held at the room (a) and ≈ -20 °C (c) temperature. The dark area of the sample corresponds to pristine Gr on copper. Fluorescent microscopy images (b) and (d) of the representative regions (a) and (c), respectively, excited using UV light-emitting diode with emission band at ≈ 365 nm.

Besides the low temperature sublimation of anthracene, the other advantage of this PAH is its high fluorescence yield under ultraviolet (UV) light irradiation (Figures 3.2 (b) and 3.2 (d)), which helps visualize the anthracene during the transfer process and track residues left on Gr after annealing.

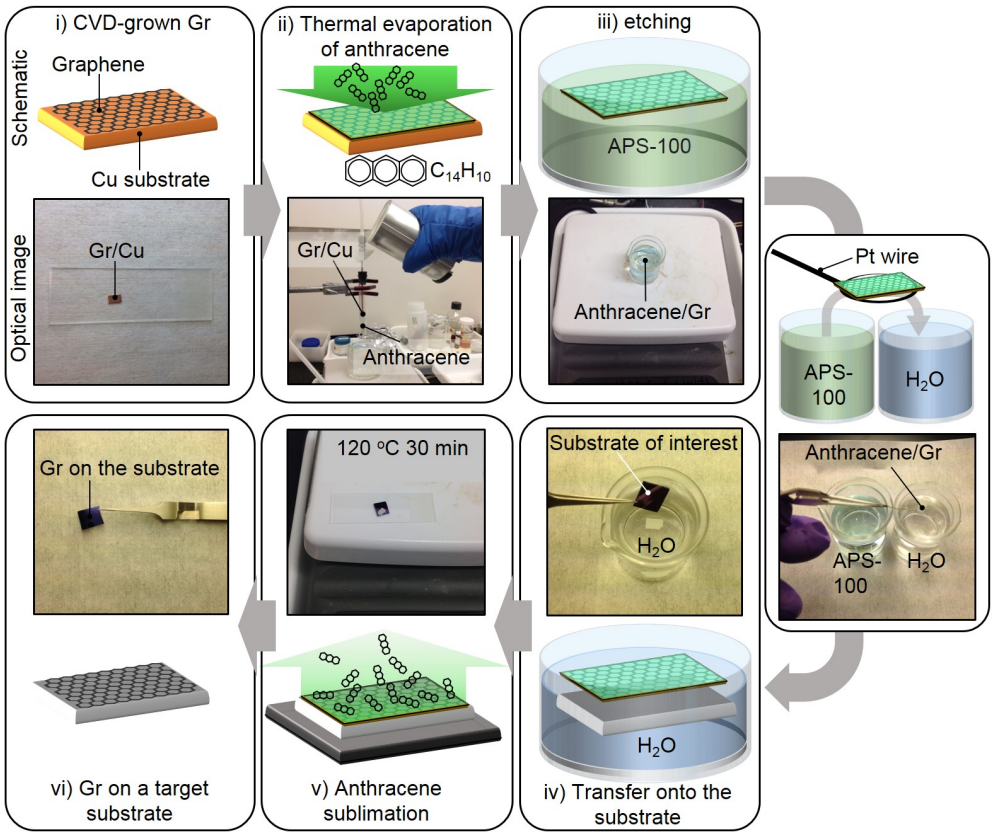

Figure 3.3: Gr transfer procedure using anthracene: (i) CVD-grown graphene on a copper substrate; (ii) thermal evaporation of anthracene onto graphene at ≈ -20 °C; (iii) copper substrate etching by aqueous solution of ammonium persulfate (APS-100) at 40 °C; (iv) Gr-anthracene transfer onto the target substrate; (v) anthracene sublimation on a hot plate at 120 °C; (vi) graphene on a target substrate.

3.3 Characterization of graphene quality using Raman spectroscopy, SEM, TEM, and XPS

Three sets of Gr membrane samples transferred using (i) PMMA as a sacrificial layer, (ii) IPA droplet capillary adhesion (so called "direct transfer"), and (iii) anthracene as a sacrificial layer were subjected to the same cleaning treatments and characterizations to compare and identify the least contaminated product.

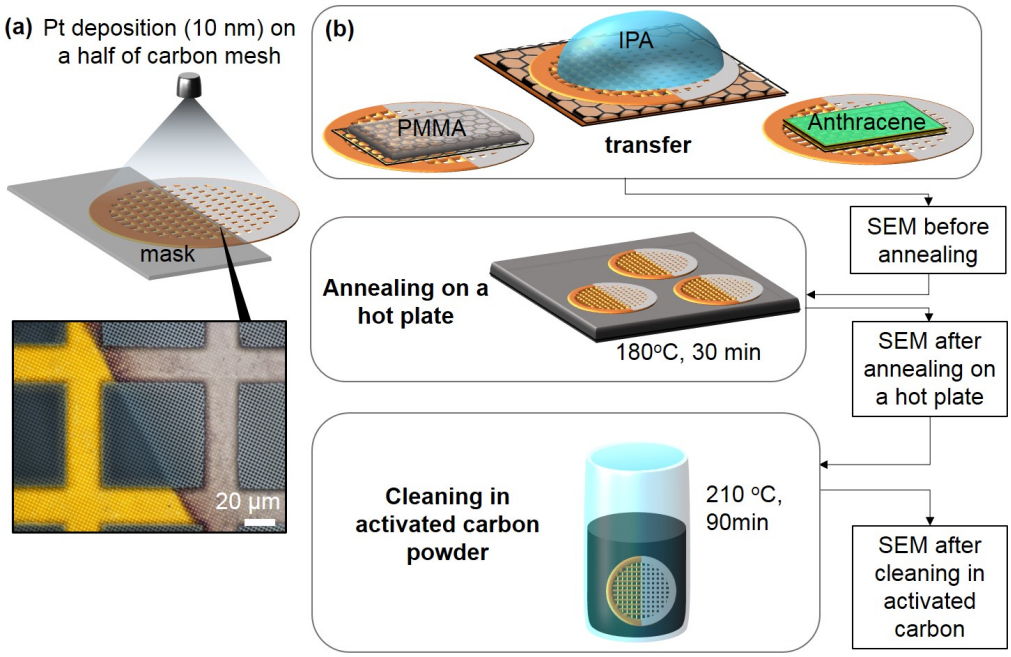

Figure 3.4: Sample preparation for comparison of graphene transfer methods. (a) Pt deposition (10 nm) on a half of a carbon mesh (*e.g.* TEM grid). (b) Schematic of graphene transfer and subsequent cleaning procedure. After each step the sample was characterized by SEM.

The sample fabrication procedure for the comparative analysis is schematically illustrated in Figure 3.4. First, TEM grids made of gold with a perforated

20 nm thick carbon mesh (2 μm hole diameter) were half-coated with a 10 nm platinum layer to compare the effect of the platinum catalysis on the surface purity (Figure 3.4 (a)) on the same substrate. Second, CVD-Gr films were transferred onto the grids using the three methods depicted in Figure 3.4 (b). All the samples concurrently underwent first the catalytic cleaning (180 °C, 30 min) on a hot plate in ambient air, followed by an activated carbon cleaning procedure step (210 °C, 90 min, rate 5 °C/min) in an oven. We used LVSEM to image all samples immediately as transferred, after the platinum-catalysis treatment, and, ultimately, after the cleaning in activated carbon. For LVSEM imaging, all samples have been mounted on a graphite specimen stub to minimize the background signal formed by spurious SEs. The same contrast/brightness adjustments were maintained during all three LVSEM sessions to quantitatively compare results of each cleaning step. To maximize surface sensitivity of the SEM to impurities, a low-energy electron beam (1 keV) in combination with through–the–lens detector, and short working distance (3 mm) were used. All samples have been studied by TEM at 300 keV electron beam energy.

XPS spectra of Gr samples were collected at $\approx 3 \times 10^{-7}$ Pa in UHV chamber equipped with a 125 mm radius hemispherical electron energy analyzer operating with an emission angle of 54 °. The monochromatic Al Kα (1486.6 eV) X-ray source was used for the XPS measurements. The analyzer was working at the constant pass energy E_p=13.6 eV and slit sizes offering an experimental energy resolution of 0.55 eV. The XPS peaks of Gr were deconvoluted using mixed asymmetric Gaussian–Lorentzian line shapes after a Shirley background subtraction.

The suspended Gr obtained by the anthracene-based method demonstrates high yield (with no holes) coverage over the perforated structure, ≈ 95% (Figure 3.5), comparable with the best results obtained using the direct transfer by IPA drop and PMMA sacrificial layer. An optical image of supported Gr on a SiO_2 substrate is depicted in Figure 3.6 (a) and indicates the continuous film with little amount of cracks and tears.

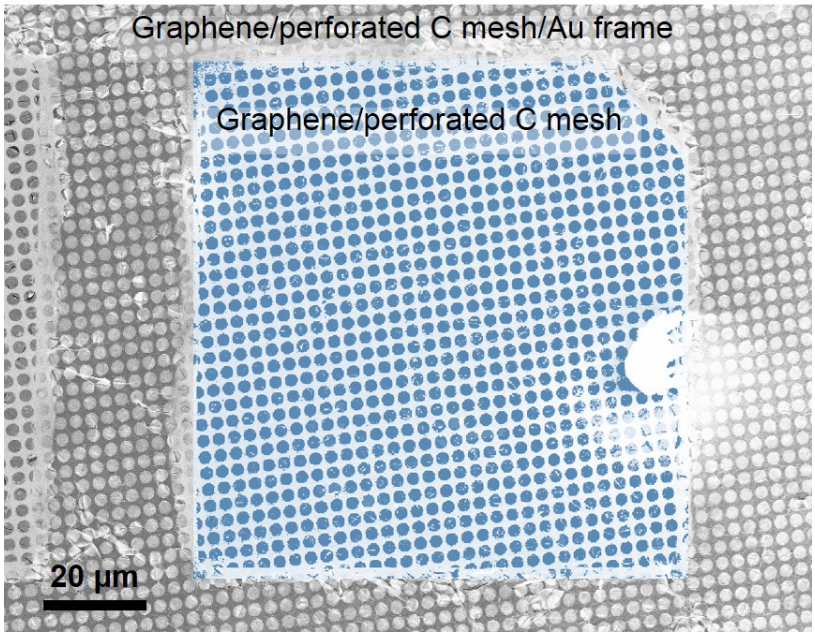

Figure 3.5: SEM image showing perforated carbon mesh covered with as transferred suspended graphene (false blue color) Surface coverage (≈95% before anthracene cleaning procedures) was calculated as the ratio of orifices covered with graphene to all orifices in carbon mesh.

Raman Characterization:

The quality of the as-transferred Gr was evaluated using Raman spectroscopy *via* measuring defect/impurities related D-peak intensity and position of G-peak (Figure 3.6 (b)). Raman spectra were acquired under ambient conditions with a

micro-Raman spectrometer equipped with a 514.5 nm (2.41 eV) wavelength excitation laser and a grating with a 1800 mm^{-1} pitch, while operating in 180 ° backscattering geometry. A 50× objective was used to focus the excitation laser to an approximately 1 μm spot onto the sample with an incident power of less than 2 mW to avoid local heating effects. The shift of G-peak in the Raman spectra indicates the induced strain in Gr (Figure 3.6 (c)). [189] The experimental data reveals compressive/tensile forces acting on a single layer Gr transferred onto SiO_2 substrate using anthracene/PMMA methods, respectively. However, since the standard deviation of ten G-peak position measurements spreads across the value of the unstrained Gr, one can conclude that both PMMA and anthracene methods can result in both compressed and stretched Gr depending on a probing location.

SEM analysis:

Different from commonly used high voltage (5 kV to 15 kV) SEM imaging, we employed low electron beam energies (0.5 keV to 1 keV) in combination with a SE detector to monitor the contaminants evolution upon different cleaning procedures. The enhanced electron interaction cross-section and surface sensitivity of such imaging conditions are advantageous for distinguishing clean and contaminated regions on the Gr layer. [190, 191]

According to the semi-empirical law for the SE emission from carbon, [192] the dependence of SE yield on electron beam energy E_b has a maximum at 400 eV and decreases with electron beam energy due to the decrease of the stopping power. The

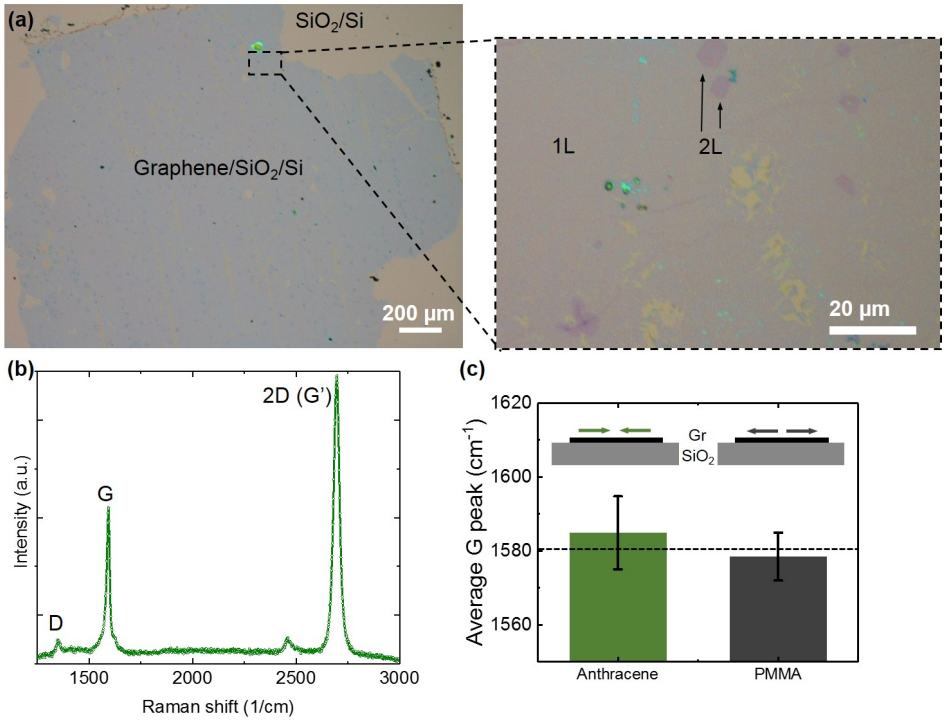

Figure 3.6: Optical image of graphene transferred on SiO_2 and Raman analysis. (a) Optical image of CVD Graphene transferred using anthracene onto SiO_2 (285 nm)/Si(100) substrate (see Figure 3.3 (vi)). (b) Raman spectra of graphene transferred using anthracene onto SiO_2 (285 nm)/Si(100) substrate. The D-peak (1360 cm^{-1}) indicates the defect density of graphene layers, the G-peak (1580 cm^{-1}) is due to Stokes phonon energy shift of the in-plane vibrational mode, and the 2D (G')-peak (2690 cm^{-1}) is the second-order overtone of another in-plane vibration. The wavelength of the excitation laser was 514.5 nm. (c) G peak values of Gr transferred using anthracene and PMMA methods. The error bars represent the standard deviation value after ten measurements on different sampling points. The dashed line depicts the G-peak value of unstrained Gr.

dependence of SE yield, δ, on membrane thickness, d, and E_b, can be evaluated [192] as:

$$\delta = 0.5\frac{E_b}{\epsilon} \cdot \frac{\lambda}{R}(1 - e^{-\frac{d}{\lambda}}), \tag{3.1}$$

where ϵ, λ, and R stand for the effective energy to produce SE, the effective SE escape depth, and the penetration depth of the incident electron, respectively. For a carbon membrane with $\epsilon = 80\,\text{eV}$, [192] $\lambda = 2.5\,\text{nm}$, and $R = 7\,\text{nm}$, the formula yields $\delta = 0.1$, 0.2, and 0.3 for 1, 2, and 3 layer thick Gr, respectively, implying that a clean, suspended, single Gr layer will be distinguishable from any additional carbon-containing residual layers. For our experiments, we used 1 keV electron beam energy to reduce electron induced carbon contamination.

Figure 3.7 demonstrates the efficiency of low-voltage SEM (LVSEM) to evaluate the cleanliness of suspended membrane. Figure 3.7 (a) depicts the model consisting of 20 nm thick carbon mesh covered with 10 nm Pt and one layer of Gr as in the real sample. Four carbon pads of 1, 2, 5, and 10 layer thicknesses and an open orifice mimic different levels of contamination and a tear in Gr layer, respectively. Figure 3.7 (b) shows the corresponding Monte Carlo simulated [163] SE images, where the grayscale refers to the number of SEs collected per 1000 PEs. According to the simulation, the impurity pads are clearly distinguishable from a pristine single-layer Gr if a low energy (<1 keV) electron beam is used as the SE yield increases with impurity thickness. The experimental results qualitatively cor-

roborate with our simulations (Figure 3.7 (c, d)). As the energy of the electron beam increases from 1 keV to 3 keV, the overall SE yield from the membrane diminishes due to the reduction in the inelastic interaction cross-section. Thus, the contrast between clean, contaminated Gr and void areas decreases (Figure 3.7 (e)) and the carbon membrane appears to be more transparent and cleaner.

LVSEM images of suspended Gr on a perforated carbon film with Pt (10 nm) film transferred using PMMA (top: a, b, c), IPA (center: d, e, f), and an anthracene sacrificial layer (bottom: g, h, i) are shown in Figure 3.8. All samples demonstrate visible contamination before cleaning, which is noted as bright spots and lighter color corrugated regions. In the case of PMMA, the typical residues are left from incomplete scission of PMMA bonds during cleaning steps. [106]

Contamination of Gr transferred by anthracene and IPA methods is mainly due to hydrocarbons; in particular, (-CH_2-) and (-CH_3) groups of hydrocarbons accumulated on the surface have been routinely detected after samples were exposed to air. [193]

A comparison between the different transfer methods was performed by imaging samples after each sequential cleaning step using SEM, see Figure 3.8. The images in the left, central, and right columns show suspended Gr before cleaning, after Pt catalytic cleaning at 180 °C, and after annealing in activated carbon, respectively. Each image contains the typical regions with a suspended membrane (dark circle in the center), Gr over Pt-covered carbon mesh (peripheral brightest area), and open holes (the darkest area). SEM images of partially cleaned CVD-Gr revealed the accumulation of the contaminants in elongated strips (Figure 3.8 (b,

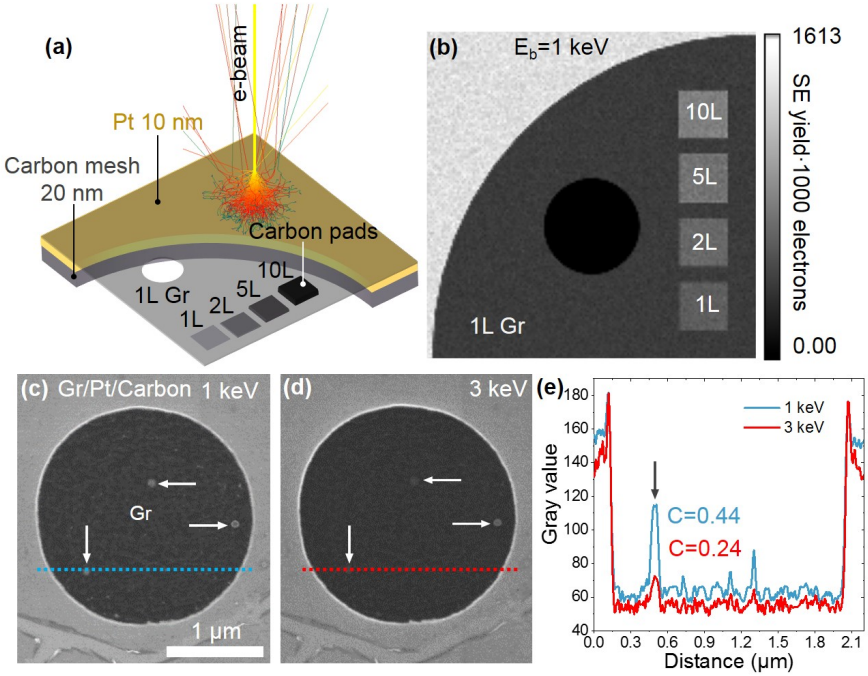

Figure 3.7: LVSEM imaging of suspended graphene with impurities. (a) Schematic of model used for Monte Carlo electron trajectory simulations. (b) Simulated secondary electron image of suspended graphene with overlaying carbon pads of 1, 2, 5, and 10 layer (L) thickness, mimicking impurities on the membrane. The black orifice represents void area. Gray scale bar values correspond to SE yield per 1000 primary electrons. Experimental LVSEM images of suspended graphene obtained at 1 keV (c) and 3 keV (d) energies of primary electrons. White arrows show impurities on the membrane. (e) The line profiles taken along the dotted horizontal lines in (c) and (d). Black arrow points to the same impurity visible in the panels (c) and (d). C-numbers correspond to contrast values between the impurity and graphene region calculated using eq. 1.7 for images (c) and (d), respectively.

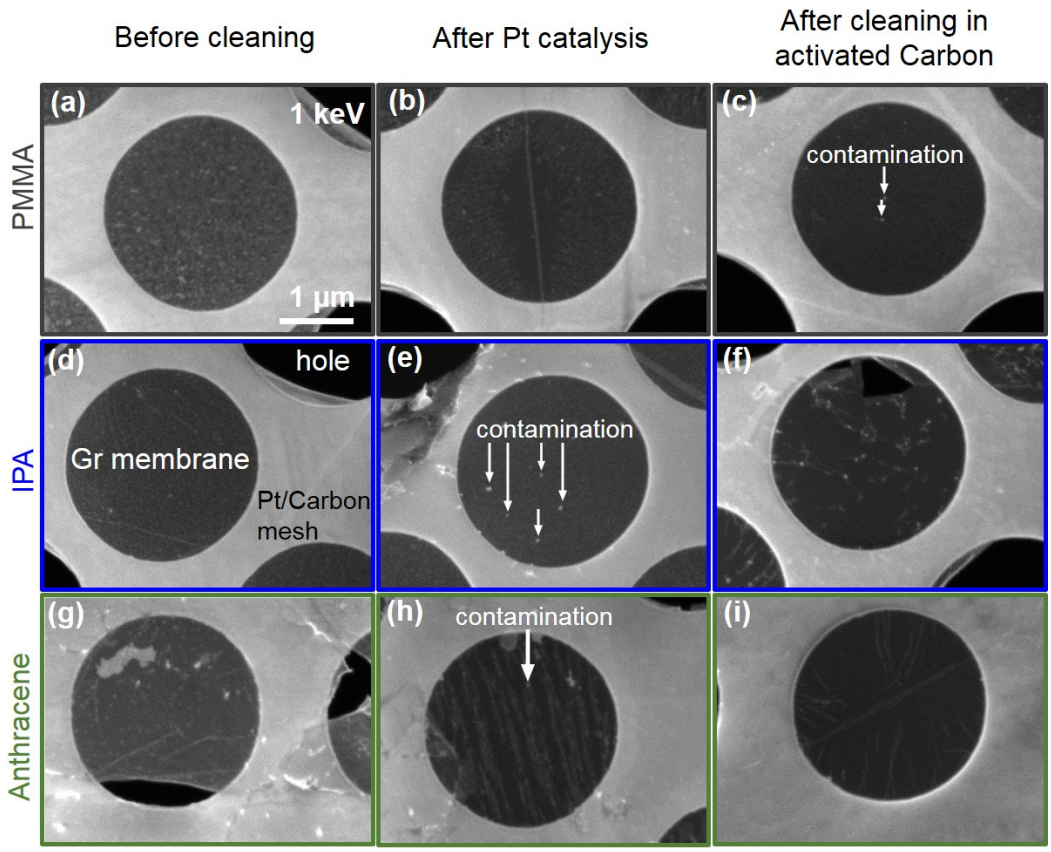

Figure 3.8: Comparison of the graphene cleanliness after consecutive cleaning cycles. Typical SEM images of free-standing graphene transferred by (a, b, c) PMMA, (d, e, f) IPA, and (g, h, i) anthracene before (left column), after annealing over Pt catalyst (central column), and after annealing in activated carbon (right column). To preserve the brightness/contrast settings, the SEM detector was set to the same fixed values of gain and offset for all the measurements.

h)). The origin of such impurity distribution is attributed to stronger affinity of the contaminating molecules to Gr point and extended defects, [194, 195] as well as to wrinkles, which are common in CVD-grown Gr and occur as a result of compressive strain in as-grown carbon monolayer. [196] According to the set of SEM images of differently prepared samples and after all treatments, PMMA and anthracene methods demonstrate fewer residues on a carbon monolayer after two sequential cleaning steps compared to the direct transfer using IPA. The evolution of the residue concentration with a cleaning sequence can be illustrated using PMMA transferred Gr as an example. The transferred (before any additional cleaning) membrane routinely contains polymer contaminants seen as multiple bright spots and network of gray patches over the membrane (Figure 3.8 (a)). The cleanliness of the suspended membranes at a microscale level can be addressed more quantitatively using the gray scale values (GSV) of SEM images, implying that the GSV is proportional to the total SE signal from the corresponding area. To conduct such measurements, the SEM detector was tuned to the same fixed values of gain and offset for entire set of measurements. The results of this analysis for all three transfer methods and samples with and without pre-deposited Pt catalyst are summarized in Figure 3.9. The vertical axis values correspond to SE signal of the imaged Gr with respect to the open hole. Therefore, the cleanest and the most transparent sample will have the SE signal approaching zero.

After annealing the samples on a hot plate, the overall SE signal from all samples decreased because the large partition of the PMMA remnants become decomposed by the Pt catalysis. During this process, end-chain PMMA dissociation is

initiated, and the polymer degrades into monomers that can sublime. [186] Interestingly, the PMMA decomposition is observed even a few microns away from the Pt catalyst. We assign this extended catalytic action to a spillover effect when dissociated reactive species such as hydrogen and/or oxygen migrate from Pt to PMMA residues. [197] Thus, the transparency of Gr after annealing in the presence of Pt catalyst increases by $\approx 50\%$ (Figure 3.9 right semi-plane). The electron transparency of the membrane without Pt (left semi-plane) improves after the same treatment only by $\approx 30\%$, confirming the noticeable contribution of catalytic activation and spillover effect.

As can be seen from Figure 3.9 (blue dots), the Pt catalysis is effective not only for PMMA decomposition, but also for cleaning from hydrocarbon contaminants after IPA transfer. The latter results in $\approx 50\%$ cleaning effect after the treatment (compare with only $\approx 20\%$ cleaning without Pt). The similar cleaning trend can be observed for Gr transferred by anthracene yielding the cleaning effect of $\approx 50\%$ after thermal desorption of contaminants.

The cleaning effect of activated carbon with high degree of microporosity, which provides high surface area, is based on its adsorptive capacity. Upon thermal activation, the contaminants left on a Gr surface randomly diffuse until they become adsorbed and trapped by high surface area activated carbon particles. This second step of cleaning significantly improves the cleanliness of the PMMA and anthracene transferred Gr. This is not the case, though, for impurities left from the IPA-based transfer. The cleaning effect is most pronounced for the sample with anthracene impurities annealed in the presence of a Pt catalyst and activated carbon. After

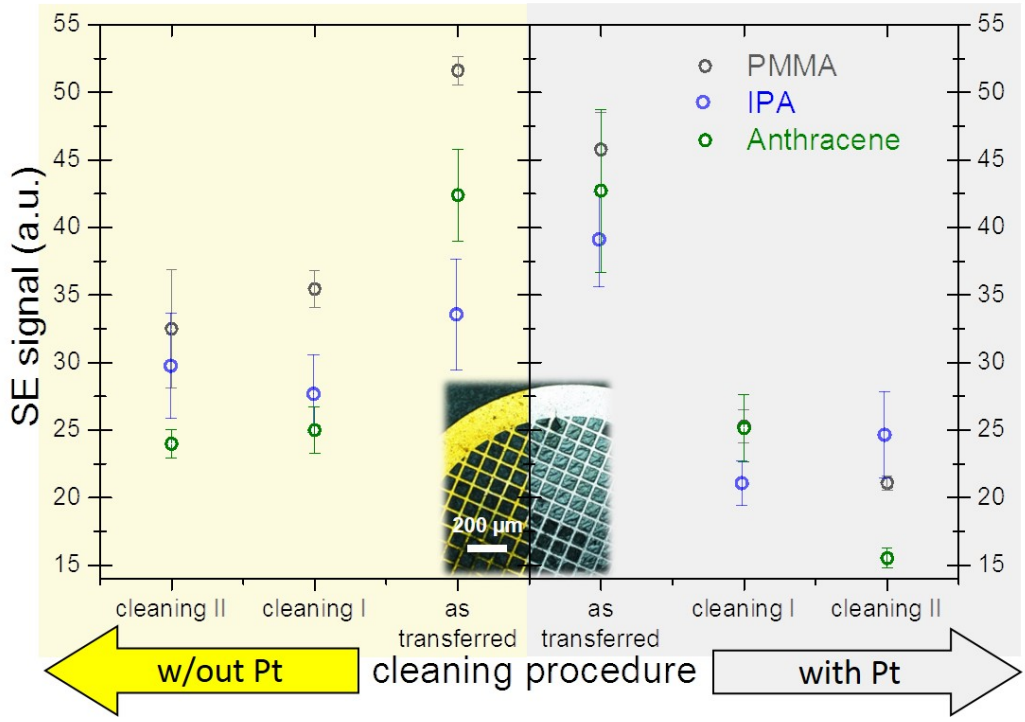

Figure 3.9: The effect of cleaning procedures on secondary electron signal (proportional to gray scale values) of suspended graphene transferred by PMMA, IPA, and anthracene. The right panel dataset was collected from the samples in contact with Pt catalyst and the left one from platinum-free region. The error bars represent the standard deviation value after five measurements on different sampling points.

the treatment, the transparency of the suspended membrane increased up to ≈ 65% compared to as transferred Gr (Figure 3.9, green dots). To summarize, the combination of two cleaning steps provides an efficient recipe to clean Gr, independent of whether PMMA or anthracene impurities were present on the sample.

It is necessary to note that electron beam induced carbon contamination can often be observed during SEM inspection of the suspended membrane. [198] This effect is particularly pronounced when the sample has hydrocarbon impurities and, therefore, can be used as an additional tool to evaluate Gr purity before and after the transfer. Low energy SEs are mainly responsible for the dissociation of surface hydrocarbons and the buildup of the carbon deposit on a membrane. [106] Interestingly, both as transferred and partially cleaned (cleaning step I, Figure 3.9) samples have demonstrated prominent contamination buildup during SEM imaging at room temperature after 15 s of irradiation (Figure 3.10). However, the carbon contamination became negligible after samples were cleaned in activated carbon, indicating that the source of the hydrocarbons is the surface residues left on samples.

XPS analysis:

The microscopy results have been complemented with XPS analysis of Gr purity. For that, CVD Gr/Cu samples underwent the same set of cleaning procedures. PMMA-covered/Gr/Cu, anthracene-covered/Gr/Cu, and IPA-immersed/Gr/Cu samples were prepared first using the standard procedures: removing the sacrificial layers by acetone, thermal sublimation, and drying, respectively. The

samples then were first annealed in air (cleaning I) followed by annealing in activated carbon (cleaning II). The effective thickness of the overlay can be evaluated from the corresponding attenuation of the XPS substrate signal by carbonaceous contaminants layer. [199] For that, the cumulative intensity ratios of C 1s peak to attenuated Cu $2p_{3/2}$ peak were measured at the same spot after the sample preparation and after each cleaning procedure (Figure 3.11 (a)). These data were compared to Cu $2p_{3/2}$ peak attenuation test of as grown and vacuum annealed pristine Gr/Cu sample considered to be ultimately clean (black square in Figure 3.11 (a)). The SESSA algorithm [200] was used to compare experimental Cu $2p_{3/2}$ peak attenuation data with theoretical predictions for 1 to 4 carbon monolayers (MLs) (Figure 3.11 (a)). The XPS-assessed effective thickness of contaminants corroborates well with the trend observed *via* electron microscopy. As-prepared samples exhibit the highest degree of contamination, reaching almost four effective monolayers of impurities in the case of a PMMA-based sacrificial layer. The cleanliness of the samples

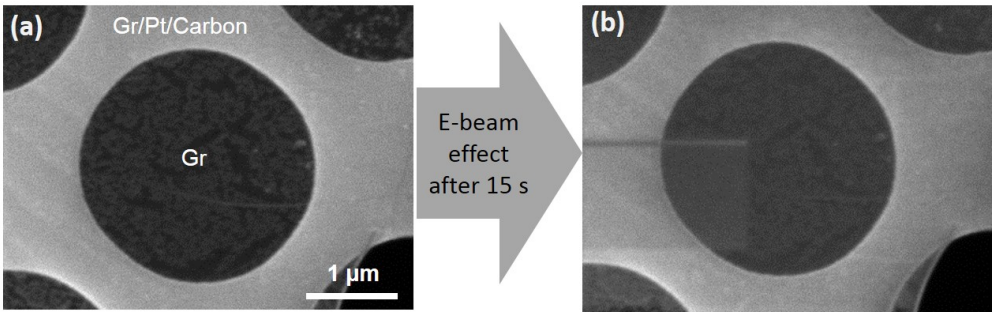

Figure 3.10: E-beam induced carbon contamination of a graphene membrane transferred by PMMA onto a carbon mesh with Pt and annealed on a hot plate. The SEM images of the suspended Gr before (a) and after (b) e-beam exposure.

improves progressively with sequential cleaning. Similar to the SEM observations above, anthracene and IPA introduced the least amount of contaminations at the Gr surface, and the final cleanliness approaches the quality of as grown and vacuum annealed CVD Gr/Cu sample, matching the theoretically predicted C 1s/Cu $2p_{3/2}$ ratio for 1 ML of carbon on copper.

More information on the chemical nature of the contaminants can be obtained from the C 1s peak shape evolution upon the cleaning treatments. Figure 3.11 (b) depicts the C 1s spectrum of as grown and vacuum annealed (10^{-7} Pa, 250 °C, 2 hours) Gr/Cu sample, that we consider ultimately clean Gr. The spectrum contains a dominating sp^2 Gr component and a minor contribution from sp^3 impurities separated by ≈ 0.75 eV. Figure 3.11 (c-e) show XPS spectra of PMMA, IPA, and anthracene transferred samples after cleaning step I. This intermediate cleaning of the PMMA sample did not completely removed a polymer, as can be seen from the prominent contribution from PMMA related peaks [201] compared to the sp^2 signal from Gr (Figure 3.11 (c)). On the other hand, the IPA and anthracene samples exhibited a dominating Gr (sp^2) contribution and traces of carboxyl (binding energy (BE) ≈ 289 eV), methoxy (BE ≈ 287 eV) groups, and sp^3 carbon (Figure 3.11 (d, e)). The overall trend observed in the XPS measurements agrees with the SEM and Raman results, showing significant reduction of impurity peaks upon cleaning in favor of pure sp^2 feature.

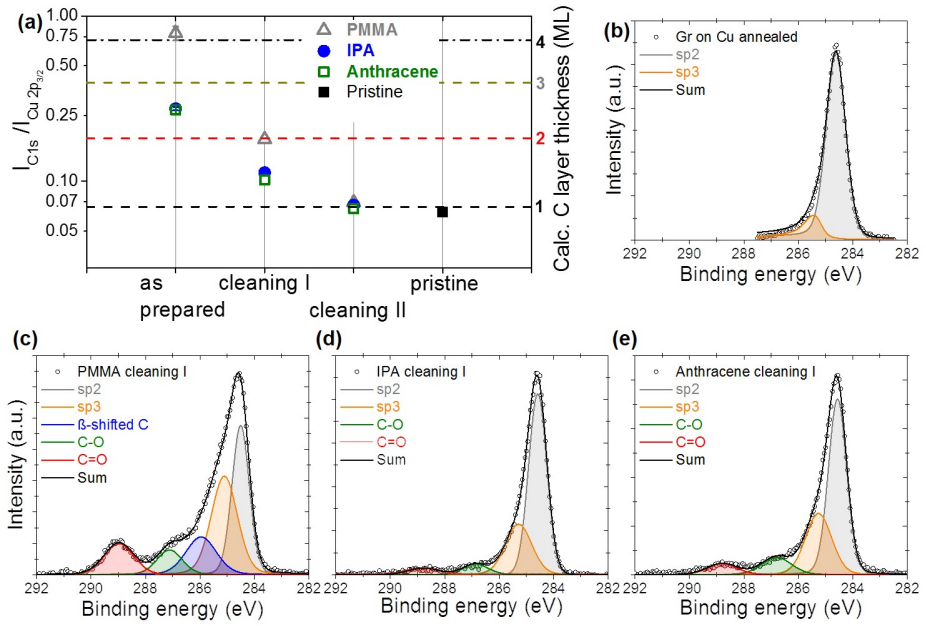

Figure 3.11: XPS analysis of transfer methods. (a) Ratio of C 1s peak to substrate Cu $2p_{3/2}$ peak for as transferred samples and after cleaning procedures for each method. Black square shows as grown and vacuum annealed pristine Gr/Cu sample. Triangle, circle, and squire marks correspond to the PMMA, IPA, and anthracene samples, respectively. Error bars are smaller or comparable to the size of data marks. (b) C 1s spectrum of as grown and vacuum annealed (10^{-7} Pa, 250 °C, 2 hours) Gr/Cu sample. (c-e) XPS spectra of PMMA, IPA, and anthracene transferred samples after cleaning step I.

TEM study:

Finally, the samples have also been examined using TEM to compare the quality of the resultant membranes at the nano- and atomic scales. Figures 3.12 (a) and 3.12 (b) show TEM images of the PMMA transferred Gr after final cleaning in activated carbon taken from the areas not affected by Pt catalyst (panel a) and areas in proximity to Pt catalyst (panel b). HRTEM images and fast Fourier transforms (FFTs) are shown in Figure 3.13. The membranes have domains of pristine Gr and a network of contaminants. The presence of the Pt catalyst results in enlargement of the area of pristine Gr, which can be as large as $\approx 2 \times 10^3\,\mathrm{nm}^2$. The cleaning effect is even more pronounced for anthracene impurities (compare Figures 3.12 (c) and (d)). The combined Pt and activated carbon cleaning results in the appearance of very large patches of clean Gr with a typical area $\approx 2 \times 10^4\,\mathrm{nm}^2$, which is comparable to or even better than previously reported results. [202]

3.4 Summary

In conclusion, we present a new method for the clean transfer of CVD-Gr using anthracene as a sacrificial layer. This approach will be particularly suitable for applications where Gr coverage is required over the chemically reactive and temperature sensitive substrates. The advantage of this approach is the dry removal of the sacrificial layer at temperatures below 150 °C, which often is a requirement for many systems. Using high surface sensitivity of LVSEM and XPS, we compare the cleanliness of the suspended membranes transferred by different methods with

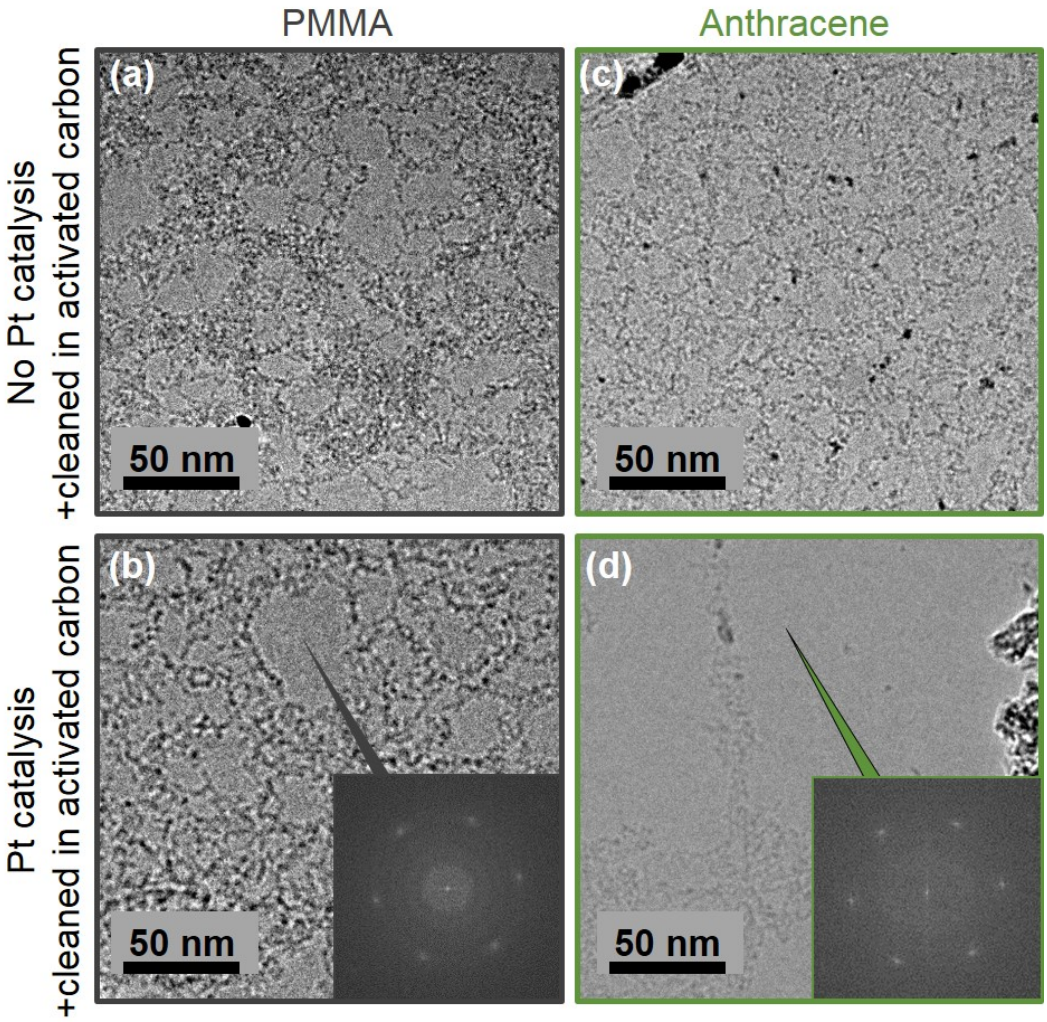

Figure 3.12: TEM images of graphene transferred by PMMA (a, b) and anthracene (c, d) onto a carbon mesh and treated thermally in the presence (b, d) and without (a, c) Pt catalyst. Insets are FFTs of HR TEM images (21 nm × 21 nm) obtained from representative regions for each method (see also Figure 3.13).

the same cleaning procedures. SEM, XPS, and TEM studies demonstrated the advantage of the anthracene method in combination with annealing in air in the presence of Pt catalyst, followed by annealing in activated carbon to achieve a cleaner CVD-grown Gr. Note, the thermal treatment of the Gr in activated carbon has a potential drawback: after cleaning, a small amount of activated carbon dust particles adheres to the sample. Therefore, whether cleaning in activated carbon should be applied depends on the particular Gr application. We envision that our approach may be suitable in applications where dry and clean transfer protocols are required.

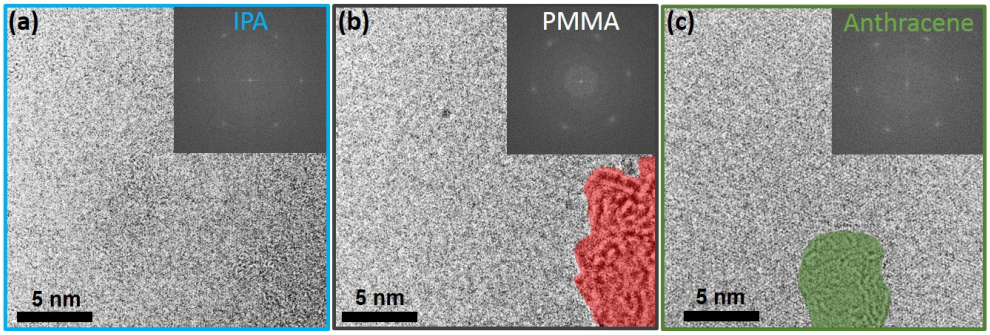

Figure 3.13: HRTEM images and fast Fourier transforms (insets) of graphene transferred by IPA (a), PMMA (b), and anthracene (c) onto a carbon mesh with Pt catalyst. Color coded regions have been excluded from FFT analysis.

Chapter 4: Graphene membranes for ambient pressure EMS

Atomic-scale thickness, molecular impermeability, low atomic number, and mechanical strength make graphene an ideal electron-transparent membrane for material characterization in liquids and gases with scanning electron microscopy and spectroscopy. Chapter 4 presents a novel sample platform made of an array of thousands of identical isolated graphene-capped micro-channels with high aspect ratio. A combination of a global wide field of view with high resolution local imaging of the array allows for high throughput *in situ* studies, as well as for combinatorial screening of solutions, liquid interfaces and immersed samples. We demonstrate the capabilities of this platform by studying a pure water sample in comparison with alkali halide solutions, a model electrochemical plating process and beam induced crystal growth in liquid electrolyte. Spectroscopic characterization of liquid interfaces and immersed objects with Auger, photoemission electron microscopy (PEEM), and energy-dispersive X-ray spectroscopy (EDS) analyses through the graphene membrane is also conducted. This chapter is adapted from Refs. [108, 109].

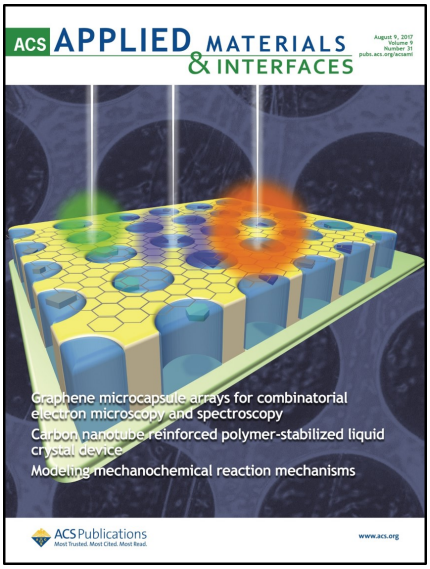

4.1 Motivation

The realization of *in situ* high throughput parallel screening of micro objects and processes in liquids with nanoscale spatial, high temporal and spectroscopic resolution is a current necessity in research related to materials genome, combinatorial chemistry, drug discovery, *etc.* Microfabricated fluidic or enclosed liquid cells equipped with electron transparent membrane windows a few tens of nanometers thick enable modern HRTEM in liquid media. [27, 67, 203, 204] Despite the continuing research and development efforts, [33, 205–208] this highly successful approach has been difficult to apply to more accessible SEM, mainly due to the significantly larger electron scattering by the membrane at typical SEM beam energies of 1 keV to 30 keV. Attempts to overcome the attenuated signal and reduced spatial resolution by increasing beam current and/or energy usually result in undesirable beam-induced effects, such as radiolysis and sample alteration.

In contrast to conventional membranes, the electron inelastic mean free paths (IMFPs) in a free standing 2D material, such as Gr, exceed its thickness. [16] Therefore, a membrane made of a 2D material is nearly transparent to electrons in a wide energy range, [49] eliminating the aforementioned limitations. The successful application of Gr liquid cells has recently been demonstrated for both SEM [209] and HRTEM. [61, 210] An alternative implementation of Gr windows *via* isolation of the entire SEM column from the ambient with electron transparent membrane has also

recently been reported. [211]

Reliable and high-yield integration of CVD Gr into the Gr-cell microfabrication process remains a challenging task. The major difficulty is the limited (yet very high) mechanical strength of the grain boundaries of CVD Gr. Having a breaking strength of ∼90 GPa, [212] suspended single layer CVD Gr is capable of sustaining a pressure differential in excess of 10^5 Pa, provided its lateral dimensions do not exceed a few micrometers. [56] Therefore, the early Gr-cell designs were single aperture devices with a field of view (FOV) of only a few micrometers. The recent demonstration of common-chamber multi-orifice Gr-cells was a significant step forward in atmospheric pressure electron spectroscopy. [213, 214] However, the probability of a catastrophic liquid release into a HV chamber due to an accidental (or beam induced) Gr rupture increases proportionally with the number of orifices. Therefore, this approach is currently used in combination with sophisticated interlocks and differential pumping stages.

In this Chapter, we describe a new liquid cell platform made from an ordered densely packed array of thousands of identical isolated microchannels capped with Gr. These high-aspect-ratio microchambers are filled with a few picoliters of liquid, thus an accidental rupture of even many cells would not affect the high-vacuum environment of the SEM. The measured lifetime of a water sample in the array exceeds several hours, enabling sufficient time to perform routine SEM and PEEM studies. The simultaneous presence of multiple channels filled with either liquid or vapor, or empty channels, in the same FOV also makes it possible to study the SEM contrast mechanisms. We demonstrate the possibility of performing EDS and AES of liquid

and immersed samples, along with the corresponding chemical mapping. Using a model electrochemical reaction, we observe the early stages of Cu electroplating on the Gr surface in real time. We envision that a multi-channel array (MCA), such as described here, will be employed as a platform for high yield combinatorial *operando* SEM studies of liquid-gas-solid interfaces relevant to electrochemical or biomedical applications.

4.2 Graphene liquid/electrochemical cells: design, fabrication, SEM tests, electrochemical tests

Gr is grown on a Cu foil using a high-pressure modification of the commonly used CVD method. As-grown Gr is transferred onto one side of commercially available glass MCA using PMMA as a sacrificial layer (Figure 4.1 (a)). [105] Briefly, a 200 nm PMMA film is spin-coated onto a Gr/Cu stack followed by etching copper in APS at 40 °C for 2 h. Then, the Gr monolayer is rinsed three times in deionized (DI) water and transferred onto another Gr/Cu foil. After annealing the sample on a hot plate for 2 h at 180 °C, etching in APS and rinsing in DI water are repeated again. A PMMA/bilayer Gr stack is transferred onto a MCA consisting of thousands of hollow straight channels with a diameter of 5 μm and 1:80 aspect ratio. Prior to Gr transfer, the MCA front surface is pre-coated with 200 nm/10 nm Au/Cr film serving as an adhesive layer for Gr and to minimize substrate charging during the SEM imaging. Then, the sample is annealed on the hot plate for 2 h at 180 °C again. For electrochemical measurements, the inner part of the channels at the backside

of MCA is covered with 40 nm Pt layer using ALD (Figure 4.1 (a)). [108] After the transfer, the PMMA is dissolved in acetone bath at 70 °C. Then, the acetone is gradually substituted with the IPA solution at 80 °C and then with DI water (Figure 4.1 (b)). For studies involving electrolytes, a droplet of the electrolyte is drop-casted onto the backside of the MCA. After few minutes required for establishing concentration equilibrium, the excess of the droplet is removed with a filter paper and a UV curable adhesive or liquid metal such as galinstan (GaInSn) is applied to seal the liquid containing MCA channels. The backside of the sample dedicated to combinatorial SEM imaging is pre-patterned with strips of a hydrophobic layer before the liquid filling. This prevents cross-contamination between the analytes during application. The resultant cell contains thousands of identical vacuum-tight microchannels filled with a liquid of interest (Figure 4.1 (c)).

4.3 Lifetime of liquid samples under vacuum conditions

The lifetime of a liquid sample in an MCA under vacuum conditions is one of the crucial experimental parameters defining the overall time allowed for imaging and analysis. It depends on the water leakage rate through intrinsic defects in a Gr membrane and/or through diffusion runaway along the Gr-MCA interface. The as-grown Gr quality, [56, 215, 216] the interface preparation, and the Gr transfer process can significantly affect both the intrinsic porosity (the areal ratio of holes to a Gr window) of the resultant membrane and the interfacial leakage. [56] We used bilayer Gr to reduce the inherent CVD Gr permeability. [216, 217] We assume

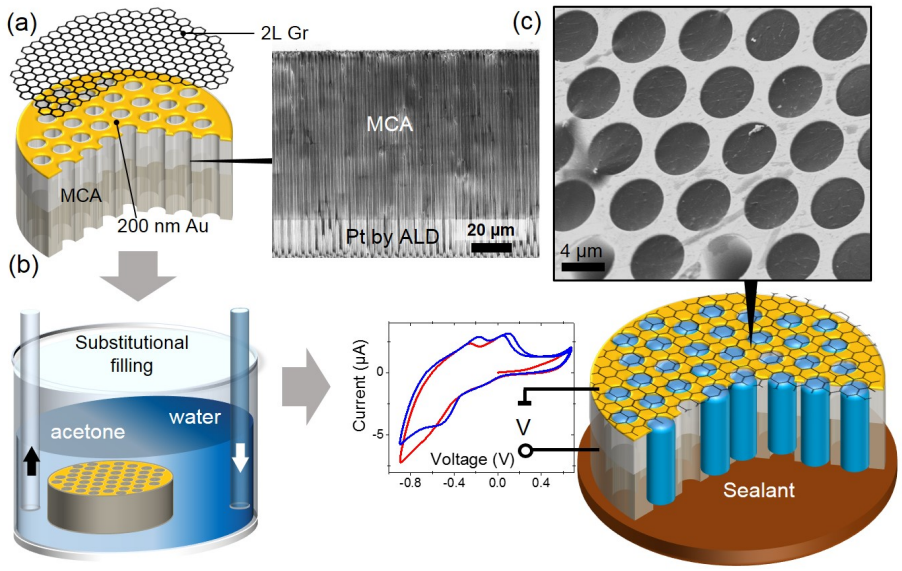

Figure 4.1: The fabrication and filling of the MCA matrix with an analyte. (a) A 200 nm Au/10 nm Cr film was sputtered sequentially onto the front side of the MCA silica matrix for metallization and reliable adhesion of graphene. For electrochemical measurements, the interior of the MCA channels was coated with 40 nm of Pt as a counter-electrode using atomic layer deposition (ALD). Bilayer graphene was transferred onto the front side of the MCA using PMMA as a sacrificial layer. The inset shows a cross-sectional SEM image of the MCA half-coated with Pt. (b) PMMA was dissolved in an acetone bath followed by a gradual substitution with IPA and water. (c) Depending on application, the sample was sealed either with UV curable adhesive or liquid metal (galinstan). The inset demonstrates the SEM image (3 keV) of water filled MCA channels. The exemplary voltammograms are shown here to highlight the electrochemical capabilities of the MCA platform.

that the backside of the MCA sample is vacuum tight sealed with an adhesive and the MCA matrix is also water impermeable. As it will be shown below and in the supporting file, the lifetime of the liquid sample inside the MCA is predominantly controlled by the density of native defects, tears and wrinkles in the covering Gr.

Since the MCA is comprised of identical channels, the lifetime of the liquid sample can be evaluated *via* measuring the filling factor (the ratio of filled channels to their total number in a FOV) as a function of time. The distinct difference in SE and BSE signals from liquid and dried channels allows us to use a simple threshold image processing algorithm to discriminate between these two moieties and determine the filling factor within the FOV. The sequence of SEM images in Figure 4.2 (a) demonstrates typical water loss in an MCA under vacuum conditions over several hours: from ≈86% filled channels in the beginning of observation to ≈23% after 5.1 hours. The measured filling factor as a function of time is depicted in Figure 4.2 (b) and indicates that the half-life time (the time when the filling factor halves) for the sample $t_{1/2}$ ≈1.7 h.

To analyze the impact of leakage on the filling factor, (i) we implement the cumulative Poisson distribution function to describe the temporal dependence of the total amount of the MCA empty channels, and (ii) we proposed a model based on a water permeable defects having normal distribution of effective areas across all channels to reveal the average size of defects in a Gr membrane.

(i) In the first model, we assume that the number of empty channel follows the cumulative Poisson distribution as time proceeds:

$$1 - Y(t) = e^{-\mu} \sum_{i=0}^{t+t_0} \frac{\mu^i}{i!}, \tag{4.1}$$

where $Y(t)$ is the temporal dependence of the filling factor, μ is the Poisson rate parameter, t_0 is the time when the first SEM image showing the empty/filled channels is collected, and t is the time of observation. After fitting the experimental data of the filling factor using eq.(4.1), we obtain $t_0 \approx 3$ h, and $\mu = 4.2$ h (Figure 4.2 (b)). The obtained numbers mean that the highest rate of filled-to-empty channel transformation occurs ≈ 1.2 h past the time when the first SEM image was collected. The physical interpretation qualitatively indicates that it still takes 1.2 h for rapidly drying channels to become completely empty. After 1.2 h, the filling factor drops not so fast due to the channels comprising less defects.

(ii) The second approach is based on a water permeable defects having normal distribution of effective areas across all channels. [108] In this model, we assume that the volume of liquid phase in the channel decreases with time due to the leaks through: (i) nanoscopic holes in the Gr and (ii) the Gr-substrate interface. The latter leakage channel is clearly evidenced in the low voltage SEM sequence in Figure 4.2 (c) as appearance and growth of "under carpet" water blisters surrounding the evaporating channel. The liquid adhered to Gr membrane remains all the time until its thickness reaches the onset of capillary instability due to hydrophobic nature of the Gr (middle panel in Figure 4.2 (c)). The free space released in the channel because of gradual liquid phase loss is filled with the water vapor. To estimate the

water retention time inside MCA in a vacuum, we assumed a normal distribution of effective area, s, of defects in every Gr-capped 5 μm wide MCA channel. At the defective sites, water effusion can be described with Knudsen's equation for a molecular flux per unit area:

$$F = \frac{P_S}{\sqrt{2\pi m_0 kT}}, \tag{4.2}$$

where P_S is the saturated water pressure at room temperature, m_0 is the mass of a water molecule, T is room temperature, and k is Boltzmann constant. The normal distribution of Gr defects, s, is expressed by

$$D(s) = A\frac{1}{\sqrt{2\pi}\sigma}e^{\frac{(s-s_0)^2}{2\sigma^2}}, \tag{4.3}$$

where σ and s_0 stand for the standard deviation and mean area of defects, respectively. A is a constant to normalize the distribution between $s = 0$ (channels without leak) and the maximal opening $s = S$ (channels without membrane). Each filled channel must lose a fixed amount of water of mass M to become empty. To obtain the temporal dependence of the filling factor, we integrate the normal distribution within 0 to t domain. After integration and normalization, the filling factor is:

$$Y(t) = \frac{erf\left(\frac{\frac{M}{fm_0(t+t_0)}-s_0}{\sqrt{2}\sigma}\right) - erf(\frac{-s_0}{\sqrt{2}\sigma})}{erf\left(\frac{S-s_0}{\sqrt{2}\sigma}\right) - erf(\frac{-s_0}{\sqrt{2}\sigma})}, \tag{4.4}$$

where t_0 is the moment when water starts evaporating. The latter was used to fit experimental data in Figure 4.2 (b).

Assuming molecular flow and a normal distribution of the nano-holes with an effective area s, a mean value s_0, and a standard deviation σ for a $5\,\mu$m diameter microchannel in the MCA sample, the filling factor in Figure 4.2 (b) can be fit using a Gaussian distribution function with $s_0 = 4.3{\times}10^3\,\mathrm{nm}^2$ and $\sigma = 2.1{\times}10^4\,\mathrm{nm}^2$. The reported porosity of the pristine CVD Gr varies between 0.012% and 0.61%. [217] Accepting the average porosity numbers for our case, the total open area of defects in the bilayer Gr per orifice will be less than $7.3 \times 10^2\,\mathrm{nm}^2$. Comparing the obtained number with an experimentally determined total s_0, it is reasonable to conclude that these are not Gr defects but the interfacial leakage that determines the lifetime of the MCA liquid sample under HV conditions. This result is not surprising since the standard Gr transfer procedures unavoidably results in a network of percolating wrinkles and microscopic tears at the sample interface.

4.4 Characterization of liquid samples using SEM, XPS, Auger, and PEEM

To explore the behavior of our new system, we first study SEM image contrast in a water filled MCA sample. The sample was observed using a field emission SEM. An Everhart-Thornley (E-T) detector sensitive to both SE and BSEs was employed for SEM imaging. The SEM base pressure was $\sim 10^{-4}\,\mathrm{Pa}$. The gray scale value of the SEM images was linearly proportional to the intensity of scattered and SEs

collected by the detector. For lifetime measurements, the SEM images were obtained at 5 keV and few tens of pA PE beam. For EDS spectroscopy and mapping, the sample was probed by a 15 keV PE beam. In terms of Figure 4.4 (a): θ=45 °, α=90 ° for EDS. The MCA platform enables studying the channel content comparatively and quantitatively due to the simultaneous SEM imaging and analysis of cells with different filling status while being probed under the same imaging conditions.

When an MCA is filled with water, the observed SEM GSVs can be partitioned into 4 typical groups (Figure 4.2 (d)): (i) open channels with completely or partially broken Gr membranes (bright); (ii) empty channels covered with a suspended Gr (bright); (iii) channels containing water vapor and yielding the lowest signal (dark); and (iv) channels filled with water that generate the intermediate gray values in SEM images. More quantitatively this partitioning can be represented by GSV histograms depicted in Figures 4.2 (d) and 4.3 (b). Interestingly, the Monte-Carlo [163] electron trajectory simulations of MCA of all aforementioned groups predict the smallest number of SEs and BSEs collected from empty channels (Figure 4.2 (e)). This discrepancy between the observed and the simulated images originates from the negative charging of MCA silica walls of empty or partly Gr covered channels under the PE beam irradiation, which leads to higher SE yield. [164] The SEM signal from channels with liquid excludes a contribution from the channel walls and is formed by SEs and BSEs from both the Gr membrane and water (Figure 4.2 (e)). Hence, the SEM image of liquid channel is uniformly gray. The electron scattering inside vapor filled channel is reduced and, therefore, the interaction volume of electrons with vapor significantly exceeds the one in a liquid channel. Different from the empty

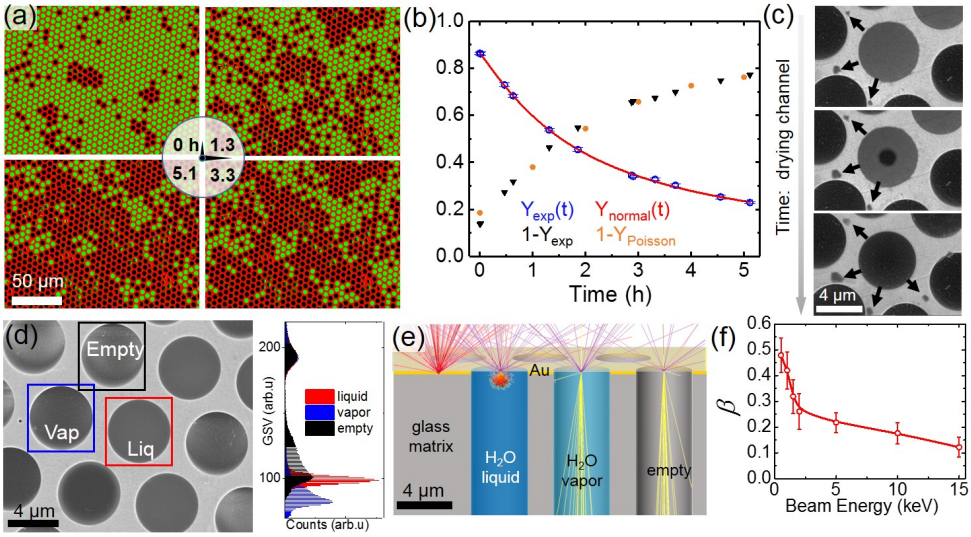

Figure 4.2: (a) SEM images of the MCA (false colored), showing a decrease in the number of channels filled with liquid over time (vacuum $\approx 10^{-4}$ Pa). Bright circles are water filled microchannels; dark circles are empty ones. (b) Experimentally recorded time evolution of the filling factor (Y_{exp}(t) marked by blue open circles) and empty factor (1-Y_{exp}(t) highlighted by triangle marks). The data were obtained from consecutive SEM images of the same FOV ($2.5\times10^4\,\mu m^2$ corresponding to ≈900 micro-channels). The error bars are due to uncertainty in the filling status of the channels at the very perimeter of the FOV. The orange marks and the red curve depict data fitting the filling and empty factors based on a cumulative Poisson and normal distributions of defects across channels, respectively. (c) The sequence of SEM (E_b=2 keV) images showing the typical steps of the channel drying process: water filled (top panel), bubble (middle panel) and vapor containing (bottom panel) channel. The arrows indicate the transport of water under the graphene towards few newly formed water blisters (dark). (d) SEM image (E_b=10 keV) of empty, water-filled and vapor-filled MCA channels, all sealed with bilayer graphene. Bright (framed with black square), uniformly gray (framed with blue square), and uniformly dark (framed with red square) channels correspond to empty, water and vapor filled channels, respectively. The histogram on the right shows the different distributions of the GSV inside the corresponding square frames. (e) Monte-Carlo trajectories simulations of 8 keV electron beam interacting with an empty (vacuum-filled) channel, a water-vapor-filled channel (assuming 3.17 kPa water saturated vapor pressure at 25 °C), a liquid-water-filled channel, and the gold MCA surface. (f) The H_2O to Au signal ratio of scattered electrons vs. electron beam energy. The error bars show the standard deviation of GSV of 5 different SEM.

channel scenario, electrons and ions inside the vapor filled channels neutralize the charging of the glass walls, and SE signal originates only from the Gr membrane and a low-density vapor inside the channel. Thus, the vapor filled channels yield the lowest SE intensity among all other covered cells. The intermediate contrasts can also be observed due to fast transient processes such as bubble formation, beam induced radiolysis, recondensation or impurities segregation.

It is important to note that different from TEM and prior SEM studies of liquid media enclosed in liquid cells, [1] the graphene's high electron transparency offers the capability of imaging the liquid-solid/liquid-gas interfaces *via* collecting true low energy SEs (Figure 4.3). This opens new possibilities for monitoring the spatio-temporal evolutions of the electrified interfaces within only one-two nanometers from the Gr surface. Conversely, monitoring high energy back scattered electrons allows probing the objects immersed in liquid few microns deep below the capping Gr membrane. Therefore, the choice of the PE beam energy and detector type are important for optimal SEM imaging conditions of liquid samples. Since the MCA platform allows for simultaneous recording of the SEM signals from Gr capped channels that are water-filled (S_{water}) and vapor-filled (S_{vapor}), as well as from the Au surface (S_{Au}), it is possible to deduce a measurable parameter that is independent of the pre-selected SEM brightness and contrast settings.

An electric potential on E-T detector with a positively biased Faraday cage was set to collect SEs. Under these settings, most of the SEs and a fraction of BSEs were collected. The gray scale values of the SEM images are, therefore, proportional to the local total electron yield detected. When the PE beam hits an MCA channel

without Gr, (or capped with broken one) it inevitably charges the inner glass walls of the high aspect ratio microchannel. The accumulating charge causes an increase of the SE electron signal and explains the elevated gray scale values from those channels. Similar scattering and charging take place inside the empty microchannels that are completely covered with a double layer Gr membrane. Gray scale values for those channels are lower compared to ones with broken (missing) Gr due to attenuation of the SEs and BSEs by the Gr membrane. Due to inhomogeneous charging, none of these groups of channels were used for image analysis. Different from the above, channels filled with water vapor do not exhibit charging of their walls. Since the intensity of BSEs and SEs generated by the vapor is very small, only SE_m and BSE_m from the Gr membrane can be detected by the SEM detector. Therefore, vapor filled channels exhibit the lowest SE signal

$$S_{vapor} \approx SE_m + BSE_m. \tag{4.5}$$

When the channel is filled with water, the SEM signal from water cell capped with Gr S_{water} includes:

$$S_{water} = SE_m + BSE_m + \eta_{SE} \cdot SE_{water} + \eta_{BSE} \cdot BSE_{water} + SE_{water-m}. \tag{4.6}$$

Here, $SE_{water-m}$ is the SEs generated inside the Gr membrane by outgoing BSE emitted in water and η is an energy dependent attenuation factor accounting for

attenuation of the electron flux by the Gr membrane. It is convenient to use SEM signal from the gold coated MCA as a reference. Similar to eq. (4.5), SEM signal from the Gr coated Au film can be written as

$$S_{Au} = SE_m + BSE_m + \eta_{SE} \cdot SE_{Au} + \eta_{BSE} \cdot BSE_{Au} + SE_{Au-m}. \tag{4.7}$$

Here, SE_{Au-m} is the intensity of the SEs generated in Gr by BSE scattered in Au film. Now we can introduce a relative contrast value:

$$\beta = \frac{S_{water} - S_{vapor}}{S_{Au} - S_{vapor}} = \frac{\eta_{SE} \cdot SE_{water} + \eta_{BSE} \cdot BSE_{water} + SE_{water-m}}{\eta_{SE} \cdot SE_{Au} + \eta_{BSE} \cdot BSE_{Au} + SE_{Au-m}}. \tag{4.8}$$

The dependence of β on electron beam energy is shown in Figure 4.2 (f). If an electron attenuation length is significantly larger than Gr membrane thickness, we can neglect the $SE_{water-m}$ and SE_{Au-m} terms. Thus, we obtain:

$$\beta = \frac{\sigma_{water}}{\sigma_{Au}}. \tag{4.9}$$

Here, σ_{water} and σ_{Au} are the total electron yields of water and gold, respectively (both values depend on the PE beam energy). This condition occurs at high electron beam energy and, since the SE/BSE ratio generally decreases with energy, β approaches the ratio of the corresponding BSE coefficients. Conversely, at low electron

energy the surface sensitive SEs and corresponding attenuation factors contribute majorly to β parameter and, therefore, it approaches 1 when the Gr membrane dominates the signal independently of the region of interest.

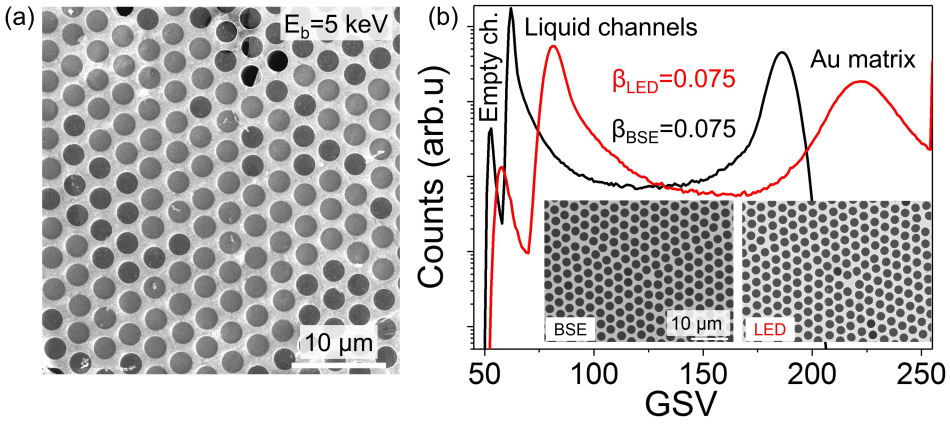

Figure 4.3: SEM imaging of the sample using different detectors. (a) TTL secondary electron image of water-filled MCA. (b) SEM GSV histograms of water-filled MCA recorded simultaneously from the same area (insets) using standard ET and BSE SEM detectors (E_b=10 keV).

Due to high SE contribution form liquid layers below Gr the employment of the TTL or E-T type lower electron detectors (LED) is preferable over BSE detector in a wide energy range of PEs. As an example, water filled channels can be easily discriminated from the empty ones in Figure 4.3 (b). In practice, even for 10 keV PE beam the β-parameter measured with LED is twice larger compared to one recorded using BSEs. This is due to significant contribution of the $\eta_{SE} \cdot SE_{water}$ member (see eq. 4.8) to the total electron signal measured by LED.

In addition to imaging, transparency of the Gr membranes to electrons and photons enables chemical analysis and elemental mapping of liquids and immersed

micro-objects under the ambient pressure conditions. Below we discuss the application of two of the most commonly used electron spectroscopies integrated with SEM, EDS, and AES in liquids. Generally, the IMFPs for outgoing electrons are orders of magnitude smaller than the penetration depth for similar energy X-ray photons, making the AES probing depth T_W on the order of 1 nm to 2 nm while an EDS signal can be recorded from hundreds of nanometers deep into the water. Therefore, these "electron in-electron out" and "electron in-photon out" spectroscopies (Figure 4.4 (a)) are not equivalent but rather complementary to each other.

EDS analysis:

Figure 4.4 (b) depicts two EDS spectra acquired through the Gr membrane from the water filled (blue line) MCA channel and the same channel after liquid was dried (red line). [108] The spectra contain the major O Kα peak at 0.53 keV showing the signature of liquid water below the Gr membrane and three minor peaks: C Kα, Au Mα, and Si Kα originating from the Gr and surface/walls of the MCA matrix. One can notice that despite the attenuation of outgoing X-rays by water, the scattering of PEs in water enhances C Kα, Au Mα, and the Si Kα emission in the water filled channels compared to the empty ones. This is due to geometry of the sample and EDS setup, where 15 keV beam penetrates microns deep into the empty channel before it hits the walls. The X-rays generated inside the empty channel have no direct line of sight to the detector and become strongly attenuated by MCA matrix. Figure 4.4 (c) shows the corresponding SEM images and elemental maps obtained through the Gr membrane. The channels filled with water exhibit a

more prominent O Kα intensity compared with the empty (or vapor filled) channels, which marked with white circles in Figure 4.4 (c). EDS is not sufficiently sensitive to distinguish between empty and vapor filled channels. Note, that the contribution of the Gr membrane to the total EDS signal is negligible, making the novel MCA platform an excellent candidate for analysis of samples immersed in gaseous and liquid environments.

AES analysis:

Unlike EDS spectro-microscopy, which can probe water immersed objects hundreds nanometers deep, [219] AES is a surface sensitive technique due to strong attenuation of the 100 eV – 1000 eV Auger electrons in the condensed matter. Therefore, AES was used exclusively to study solid surfaces under high or UHV conditions, [220] In this work, we demonstrate that ultrathin membranes can be used to extend the standard laboratory based scanning AES metrology to the realm of liquid interfaces and immersed objects. [108] The AES analysis was performed at room temperature in a UHV chamber at a base pressure of $\approx 10^{-7}$ Pa. The AES spectra were collected at 3 keV or 5 keV PE beam energies and 400 pA current followed by spectra averaging over 19.6 μm^2 area of MCA channels ($\theta = 85\,^\circ$, $\alpha = 65\,^\circ$). Radiolysis effects, such as hydrogen bubble formation, may strongly affect AES spectra collection. Only those filled channels which did not change their composition during AES acquisition were used for analysis. The peak-to-peak intensity was deduced from the differential spectra. To calculate the thicknesses of Gr and water layers,

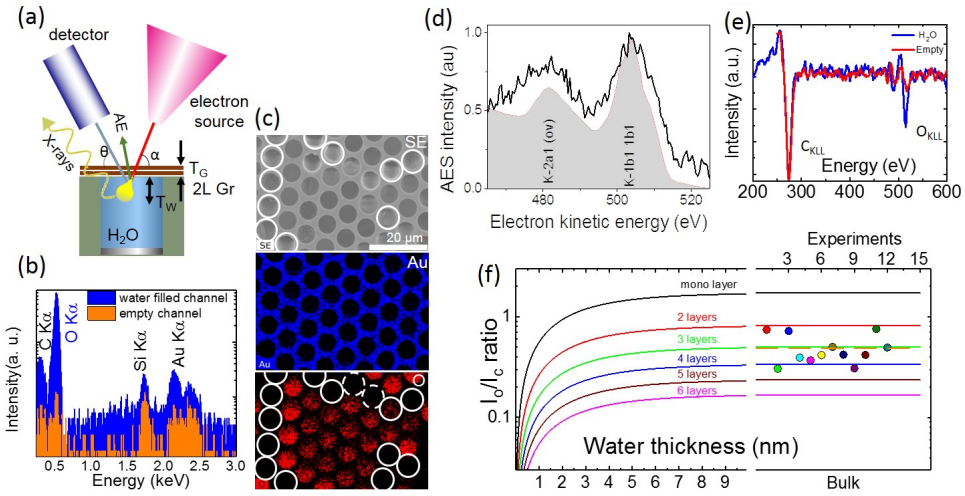

Figure 4.4: Electron spectroscopies in a liquid-filled MCA. (a) The experimental setup for EDS and AES data collection. The yellow bulb defines the electron interaction volume. (b) EDS spectra (log scale) recorded in water filled (blue) and empty (orange) channel acquired through a double layer graphene membrane. The intense O Kα peak is due to the presence of liquid water inside the channel. The Si Kα and Au Kα peaks originate from the Au coated MCA silica matrix. (c) An SEM image (top) and EDS maps of an MCA with water, depicting Au and O element distribution. The white circles depict the empty channels, while dashed ones denote the channels where water evaporated during map acquisition. (d) AES O_{KLL} spectra exhibiting characteristic K-VV transitions typical for liquid water. For comparison, off-resonance AES of water jet excited with synchrotron soft X-rays from Ref. [218] is shown in a gray color. (e) Differential AES spectra recorded from two adjacent water filled (blue curve) and empty (red curve) MCA channels. (f) The calculated dependence of O_{KLL} to C_{KLL} peak intensities ratio as a function of the thickness of water under the graphene and a number of the graphene layers. The right panel shows experimental I_O/I_C data recorded from ten water filled channels capped with a bilayer graphene. The measured average ratio (dotted line) corresponds to an effective membrane thickness to be approximately 3 graphene layers.

the attenuation formula [221] and corresponding set of parameters were used.

Figures 4.4 (a) and (e) show the geometry of the experiments and typical C_{KLL} and O_{KLL} differential AES spectra in the Gr capped empty and water filled channels, respectively. Using standard attenuation formula, [220] the intensity of the C_{KLL} peak of Gr with an effective thickness, T_G, can be calculated as:

$$I_{C_{KLL}} = I_0 \cdot \sigma_{C_{KLL}} \cdot \gamma_{C_{KLL}} \cdot F(E_{C_{KLL}}) \cdot D(E_{C_{KLL}}) \cdot N_G \cdot (1+r(E_0,\alpha)) \int_0^{T_G} e^{\frac{-z}{\lambda_{C-G} \cdot sin\theta}} \, \mathrm{d}z. \tag{4.10}$$

Similarly, the intensity of the water O_{KLL} peak attenuated by the Gr membrane cap can be written as: [220]

$$I_{O_{KLL}} = I_0 \cdot \sigma_{O_{KLL}} \cdot \gamma_{O_{KLL}} \cdot F(E_{O_{KLL}}) \cdot D(E_{O_{KLL}}) \cdot N_W \cdot [1+r(E_0,\alpha)] e^{\frac{-T_G}{\lambda_{O-G} \cdot sin\theta}} \int_0^{T_W} e^{\frac{-z}{\lambda_{O-W} \cdot sin\theta}} \, dz. \tag{4.11}$$

Here, I_0 is the intensity of the PE beam, $\sigma_{C_{KLL}}$ and $\sigma_{O_{KLL}}$ are the K shell ionization cross-sections of C and O for PEs with energy of E_0, which are $1.95\times10^{-19}\,\mathrm{cm}^2$ and $0.82\times10^{-19}\,\mathrm{cm}^2$, respectively. [222] $\gamma_{O_{KLL}}$ and $\gamma_{O_{KLL}}$ are the probabilities that the ionized core level K in elements C and O will emit KLL Auger electrons, which are 0.9988 and 0.9963, respectively. [223] $D(E_{C_{KLL}})$ and $D(E_{O_{KLL}})$ are the collection efficiency of detector, which is assumed to be constant for all Auger electrons with energies above 200 eV. [224] $F(E_{C_{KLL}})$ and $F(E_{O_{KLL}})$ are the transmission

efficiency of the electron spectrometer to be proportional to corresponding Auger electron energies when the spectrometer was operated in a constant retarding ratio mode. [225] N_G and N_W are the atomic densities of the Gr $113\,\mathrm{nm}^{-3}$ and water $33.4\,\mathrm{nm}^{-3}$, respectively. $r(E_0, \alpha) = 0.255$ is Monte Carlo simulated backscattering-correction-factor [226] for 5 kV PEs propagating in water. λ_{CG}, λ_{OG}, and λ_{OW} are the attenuation lengths of the C_{KLL} Auger electrons in Gr, the O_{KLL} Auger electrons in Gr, the O_{KLL} Auger electrons in water, respectively. We used $\lambda_{CG} = 0.65\,\mathrm{nm}$ and $\lambda_{OG} = 1.29\,\mathrm{nm}$ from previous AES data. [227] For λ_{OW} we used 3.1 nm as measured by liquid micro-jet photoelectron spectroscopy. [228] The ratio between the C_{KLL} and O_{KLL} peak intensities for a T_G thick Gr membrane capping a T_W thick water layer can be calculated using the sample structure (Figure 4.4 (a)):

$$\frac{I_{O_{KLL}}}{I_{C_{KLL}}} = \frac{\sigma_{O_{KLL}} \cdot \gamma_{O_{KLL}} \cdot N_G \cdot F(E_{O_{KLL}}) \cdot \lambda_{O-W} \cdot [1 - e^{\frac{-T_W}{\lambda_{O-W}\,sin\theta}}]}{\sigma_{C_{KLL}} \cdot \gamma_{C_{KLL}} \cdot N_W \cdot F(E_{C_{KLL}}) \cdot \lambda_{C-G} \cdot [1 - e^{\frac{-T_G}{\lambda_{C-G}\,sin\theta}}]} e^{\frac{-T_G}{\lambda_{O-G}\,sin\theta}}. \quad (4.12)$$

For bulk water $T_W = \infty$, thus the ratio reduces to:

$$\frac{I_{O_{KLL}}}{I_{C_{KLL}}} = \frac{\sigma_{O_{KLL}} \cdot \gamma_{O_{KLL}} \cdot N_G \cdot F(E_{O_{KLL}}) \cdot \lambda_{O-W}}{\sigma_{C_{KLL}} \cdot \gamma_{C_{KLL}} \cdot N_W \cdot F(E_{C_{KLL}}) \cdot \lambda_{C-G} \cdot [1 - e^{\frac{-T_G}{\lambda_{C-G}\,sin\theta}}]} e^{\frac{-T_G}{\lambda_{O-G}\,sin\theta}}. \quad (4.13)$$

In this work, we used the peak-to-peak AES intensity ratio instead of area of AES peaks for estimation.

Figure 4.4 (d) shows a normal AES recorded in an individual water-filled MCA channel through a bilayer Gr cap. For comparison, off-resonance AES of a water jet

excited with synchrotron soft X-rays is shown in gray color. [218] The overall shape of the recorded AES spectra, arising from the superposition of multiple $K-VV$ type Auger decays, correlates well with the synchrotron results. In this case, a water oxygen K core hole is filled with electrons from a few available valence levels (V) with the corresponding Auger electron emission from the same moiety of the valence levels (V). The broadening and the energy shifts of the liquid water AES bands originate from the combination of the polarization screening and delocalization effects occurring due to numerous intermolecular decay channels available in liquid water. [229, 230] The elevated noise level in our scanning AES stems from the short acquisition time, which was chosen to mitigate strong radiolysis of water. Figure 4.4 (e) shows two differential AES spectra collected from water-filled and empty channels. Both spectra have identical C_{KLL} peaks associated with the Gr membranes but only the spectrum collected from the liquid-containing channel exhibits a prominent O_{KLL} component, confirming the presence of water. We use the experimental AES intensity ratio, $\frac{I_{O_{KLL}}}{I_{C_{KLL}}}$, and the attenuation formalism (see Ref. [231]) to estimate both the effective Gr thickness, T_G, and the water probing depth, T_W.

Figure 4.4 (f) depicts the calculated O_{KLL} to C_{KLL} intensity ratio as a function of water depth for several thicknesses of the Gr membrane. The curves demonstrate the saturation of the $\frac{I_{O_{KLL}}}{I_{C_{KLL}}}$ ratio, occurring once the water layer exceeds the AES probing depth. The signal for a 3 nm thick water layer nearly reaches the constant bulk-like level, independent of the Gr thickness. The experimental data collected

from water-filled MCA cells yield $\frac{I_{O_{KLL}}}{I_{C_{KLL}}} = 0.49 \pm 0.15$, which corresponds to the signal for bulk water covered in average with approximately 3 Gr layers (Figure 4.4 (f), right panel). Here, the experimental uncertainty is calculated from twelve tested channels. This deviation from a nominal bilayer Gr coverage is likely due to the presence of residual hydrocarbon and oxygen containing contaminants on the transferred CVD Gr membranes, which increases their effective thickness and attenuation of the AES signal. These preexisting -OH, -O containing contaminants contribute to O_{KLL} spectrum of the dry Gr (red curve in Figure 4.4) and preclude reliable discrimination between the vapor filled and empty channels during Auger characterization. The other factors like Gr wrinkles and folds can also contribute to the data scatter.

PEEM analysis:

Though photoelectron imaging of processes and objects in gaseous or liquid environments was a long-standing scientific goal, the differential pumping approach resulted only in $\approx 10^{-1}$ Pa of near sample pressures when applied to the PEEM setup. PEEM at liquid-solid interfaces became feasible due successful realization of the MCA platform. The MCA sample filled with water and capped with Gr was illuminated with monochromatic soft X-rays with an energy between 525 eV and 560 eV, covering the O K-absorption edge (≈535 eV). Under this excitation, fast photoelectrons and Auger electrons from the liquid that have the IMFP in excess of the thickness of the capping Gr membrane able to escape into the vacuum

with only minor attenuation. [232] These electrons constitute the total electron yield (TEY) that was used for spatially resolved XAS of the liquid or for spectrally resolved PEEM imaging (Figure 4.5 (c,d)). Water-containing areas have a sharp characteristic onset in the absorption cross-section around $h\nu \approx 535\,\mathrm{eV}$ and thus can be easily discriminated from the other substrate materials (Gr, Au) which have a flat photoemission background across this energy range.

Figure 4.5 (c) shows a set of four PEEM images of the Gr-capped water filled MCA recorded at different energies while scanning across the O K edge. [109] The contrast in these images originates from spatial variations of the local TEY from the Au-coated MCA matrix and the Gr-capped MCA channels. The Gr-capped channels can either be filled with liquid water or be empty. A fraction of the channels does not have a Gr cap and these have the lowest signal in Figure 4.5 (c). As can be seen, the contrast between water-filled and empty channels is miniscule below O K absorption threshold at $h\nu \approx 535\,\mathrm{eV}$ and increases drastically above it. Such sequences of PEEM images constitute a spatial X-ray absorption chemical map and specific regions of interest (ROI) can be designated for site-selective XAS. Figure 4.5 (d) compares two such XAS spectra collected from two ROIs: water filled (blue) and empty (red) channels. The empty channels show weak spectral feature at $\approx 532\,\mathrm{eV}$ characteristic of carbonyl group containing hydrocarbons. [233] These contaminations have been previously observed in XAS of ice and water [4] and in our case can also be due to PMMA residue at the Gr membrane left after Gr transfer. [106] On the other hand, the filled channels demonstrate an XAS spectrum with pronounced features and a shape similar to liquid bulk water probed *via* TEY or in

transmission detection modes (see reviews [234, 235] and references therein). Such a spectrum is a result of transitions from the strongly localized O 1s core level of water molecules to unoccupied valence orbitals derived from the gas-phase $4a_1$ and $2b_2$ states. [236] In good accordance with prior XAS works on liquid water, [4, 234] our PEEM-derived XAS spectrum in Figure 4.5 (d) has a characteristic pre-edge (≈535 eV), main peak (≈537.5 eV) features, and a post-edge band around ≈541 eV. The commonly accepted interpretation of water XAS features assigns the pre-peak and main band to the excitation of water molecules with one broken (or largely distorted H-bond, a so-called single-donor (SD) molecule) while the post-edge band corresponds to the molecular environment with strong H-bonds (double donor (DD) molecules) and increased tetrahedrality. [236]

It is important to emphasize that the XAS spectrum in Figure 4.5 (c) originates from the first few layers of water at the Gr - water interface. This interfacial sensitivity of the through-membrane PEEM spectro-microscopy stems from the attenuating role of the Gr layer, which has low transparency for slow few electron-volts SEs emitted from deeper water layers. [237] Therefore, the bulklike nature of our spectra indicates that interaction of interfacial water molecules with Gr is very weak and neither the electronic nor the geometrical structure are strongly affected by the Gr. In addition, the intensity ratio of the main bands and the absence of the characteristic OH (≈526 eV) or H_2O_2 (≈533 eV) [238] features in the water XAS spectrum indicate that the Gr-water interface is not accumulating radiolysis products under the selected irradiation conditions. A previous XAS study of interfacial water in contact with gold [239] revealed the significant suppression of the pre-edge peak

under similar experimental conditions. Thus, Gr represents a model benchmark material to study interfacial water behavior with PEEM.

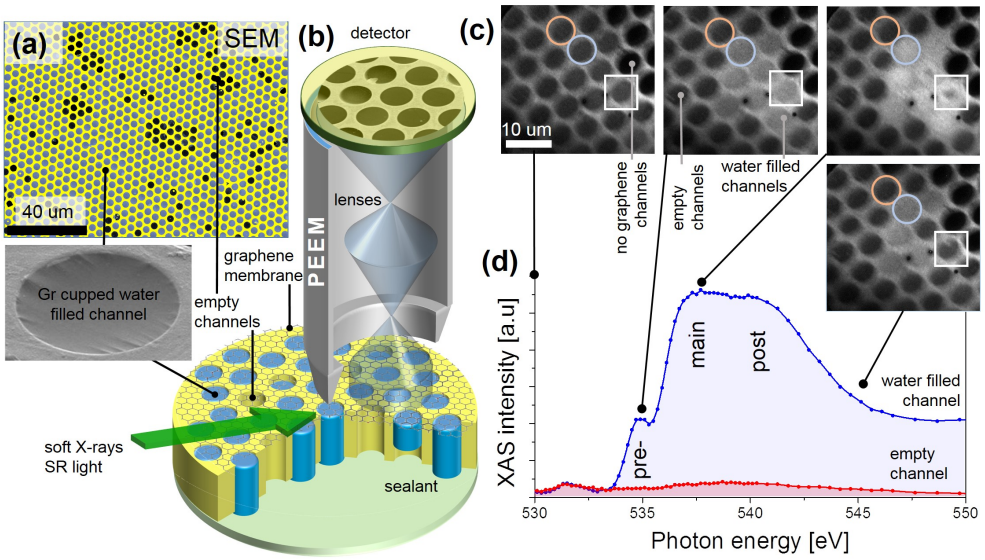

Figure 4.5: Multichannel array sample design and PEEM setup. (a) SEM (5 keV, color coded) image of water-filled graphene-capped microchannel sample; the darker channels correspond to the graphene-capped but empty channels. Inset: water-filled 4 μm wide channel (SEM, 2 keV). (b) The schematics of the PEEM and liquid cell setups. (c) PEEM images of the water filled MCA collected at different X-ray energies while crossing the O K-edge. (d) The resultant XAS spectra collected from different regions of interest: water-filled (blue circle and spectrum) and empty (red circle and spectrum) channels. White squares mark the channels that exhibit the dynamic behavior. The spectra were normalized to incident X-ray intensity.

4.5 Application examples

In addition to unique electron and X-ray imaging and spectroscopy capabilities, the Gr-capped MCA liquid sample platform has yet other advantages allowing

both: (i) high magnification stereomicroscopy in individual liquid channels and (ii) simultaneous monitoring of thousands of independent microchambers in real time when set for a large FOV. The platform, therefore, combines the advantages of high resolution SEM studies of local phenomena in liquids with the advantages of powerful image processing, pattern recognition, and data mining algorithms when applied to large FOV. [109] Below, we describe few examples of what can be routinely performed with this setup.

4.5.1 Electrochemical measurements

As an example of probing electrochemistry at (meso-) and microscale, we examine here classical copper electroplating from an aqueous 1 mol/L $CuSO_4$ solution. In our two-electrode system, the Gr-covered gold coating on the front (imaging) side of the MCA plate acts as a working electrode, and the back-side platinum coating serves as a counter and pseudo-reference electrode, as shown in Figure 4.1. Real time SEM visualization of the electroplating process in individual microchannels is correlated in Figure 4.6 with the global voltammogram simultaneously recorded for the whole MCA sample. The system starts out with a clear Gr windows at positive potential (Figure 4.6 (a), inset 1). At around -0.3 V the voltammogram shows a broad peak that corresponds to the onset of copper nucleation at the Gr-gold-electrolyte interface on the channels' periphery (Figure 4.6 (a), inset 2). This peak is very similar to the α-peak observed during copper electroplating on gold in the presence of ppm-level traces of disulfide and chlorine additives. It may arise

in our system due to the presence of small amounts of contaminants in the electrolyte and have some contribution from dissolved oxygen reduction and hydrogen adsorption on the working electrode. Clearly, this peak corresponds to underpotential deposition of Cu nanoparticles since it is followed by a main copper deposition peak (Figure 4.6 (a), inset 3) related to growth of larger copper crystals. Interestingly, at this stage the previously-formed nanocrystals start dissolving, presumably in an Ostwald ripening-type process (Figure 4.6 (a), inset 3, channel's periphery). It has been previously shown [240] that the α-peak can be assigned to underpotential deposition of Cu nanocrystals. Upon reversal of the potential sweep, copper is stripped from the working electrode in a series of anodic peaks, leaving Gr windows empty again (Figure 4.6 (a), inset 4). To ascertain the chemical composition of the observed deposits, we performed EDS mapping of microchannels, following application of cathodic and anodic potentials. As Figure 4.6 (b) confirms, a large microparticle that was grown during deposition is made of copper. It dissolves during stripping, leaving behind a copper sulfate solution with a much weaker EDS-Cu signal. This model system demonstrates the usefulness of the MCA approach in studying electrochemical processes *in situ*.

4.5.2 Beam induced crystal growth

Another illustration of MCA usage is the investigation of the complex process of electron beam induced precipitation during SEM studies in liquid solutions. For this experiment, the MCA was filled with a saturated aqueous solution of CsI, and

its front-side Gr electrode was grounded. While solution below the Gr membrane was stable in a vacuum, high-beam-current SEM imaging of the sample led to precipitation of cubic crystals inside the channels, as illustrated in Figure 4.7 (a-c). Most of the crystals were observed to nucleate at the microchannel walls (Figure 4.7 (a)), and only few grew on the Gr membrane itself. This observation can be explained by two factors: higher density of nucleation sites on the walls, and enhanced yield of SEs from the thick solid walls as compared to the liquid electrolyte and thin Gr membrane. After thermalization, the solvated electrons must be co-reactants in the crystal growth, as without irradiation no crystallization occurs. This fact rules out the possibility of precipitation due to simple water evaporation in a vacuum (*i.e.* leaky channels). Deposition and dissolution of metals (Au, Ag, Pt) and colloidal particles under electron beam irradiation has been reported previously by multiple groups. [241–245] However, only one paper, to our knowledge, has reported a beam-induced synthesis of inorganic salt crystals: $Na_2S_2O_8$ was decomposed under the beam into Na_2SO_4, and the latter precipitated due to its lower solubility in water. In our experiments, EDS mapping of the grown crystals clearly shows that they contain cesium and iodine, and not gold (Figure 4.7 (d)) despite that the gold coating slowly corrodes at the perimeter of the channels and Au^{3+} ions must be present in solution ($3I_2 + 2Au \rightarrow 2AuI_3$, see below). Several inorganic salts ($CsIO_n$, n = 2,3,4) can form as a reaction with water radiolysis products and CsI according to:

$$
\begin{aligned}
2H_2O - 2e^- &\xrightarrow{\text{e-beam}} H_2O_2 + 2H^+ \\
2I^- - 2e^- &\xrightarrow{\text{e-beam}} I_2 \\
I_2 + (2n-1)H_2O_2 &\longrightarrow 2HIO_n + (2n-2)H_2O
\end{aligned}
\tag{4.14}
$$

Or, overall:

$$
CsI + nH_2O \xrightarrow{\text{e-beam}} CsIO_n + nH_2\uparrow \tag{4.15}
$$

The $CsIO_n$ iodates (which are also cubic, as are CsI and gold) are less soluble in water than CsI, and should readily precipitate, if formed. However, as follows from eq. 4.15, their synthesis must be accompanied by release of large amount of molecular hydrogen. Simple estimates based on the crystal size (from Figure 4.7 (a-c)), hydrogen solubility in saturated CsI solution (Sechenov coefficients) and amount of released hydrogen show that large hydrogen bubbles must be formed during $CsIO_n$ growth a phenomenon that is not observed. Thus, we conclude that the growing crystals must be made of pristine cesium iodide. The mechanism of their precipitation from solution must necessarily be different from the growth of noble metal crystals and Na_2SO_4 (electrochemical reduction of precursor) and colloidal particle aggregation (alteration of zeta potential that determines their stability in solution). CsI is a strong electrolyte that does not form colloidal solutions. It is also clear that its composition is not changed during crystallization.

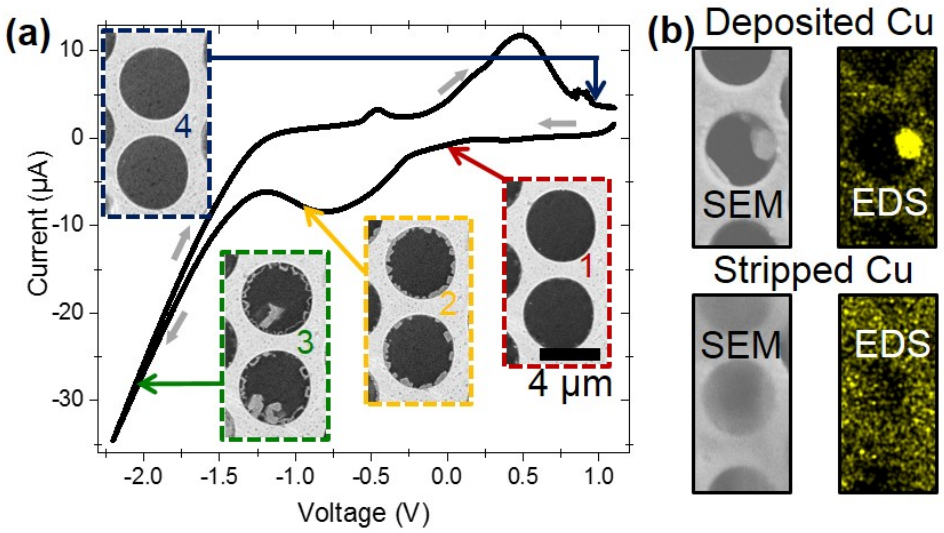

Figure 4.6: Copper electroplating and stripping: individual cells FOV. (a) Cyclic voltammogram of Cu deposition and stripping at the graphene electrode in ≈1 mol/L aqueous $CuSO_4$ electrolyte. The voltammogram was obtained at 1 mV/s scanning rate; potential was swept from positive to negative polarity and back. Platinum was used as a pseudo-reference electrode. (b) SEM images and corresponding EDS Cu maps showing deposition and stripping of a copper particle.

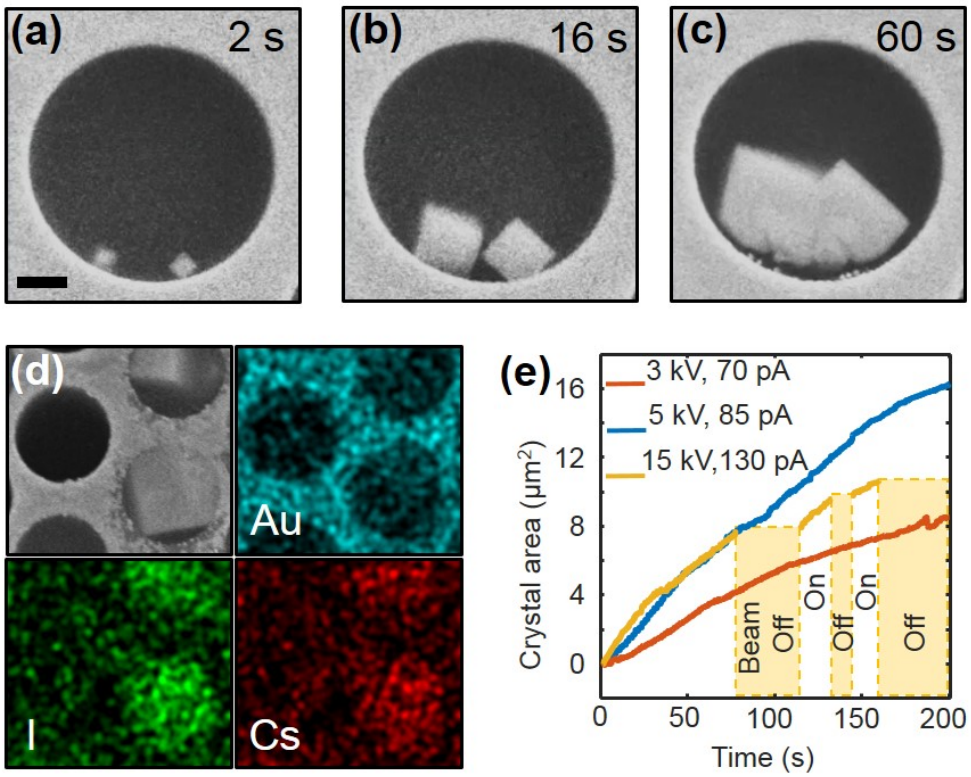

Figure 4.7: Cesium iodide crystal growth: individual cells FOV. (a-c) Consecutive screen shots from SEM video of the beam-induced nucleation and growth process of two CsI crystals from saturated aqueous solution. Although crystals originally nucleate at the wall, at later stages (panel c) they become disconnected from it due to partial dissolution. Beam energy was 15 keV. The scale bar is 1 micrometer. (d) The SEM image (gray) and EDS maps (colored) of gold, iodine, and cesium recorded from a region with grown CsI crystals. Channels are of the same size as in (a). (e) Crystal area vs. time curves extracted from videos demonstrates nearly linear dependency. The yellow curve interrupts twice for periods when the beam was blanked. Interestingly, the crystal size neither increases, nor decreases during these periods.

Thus, the CsI precipitation from solution must be determined by the change in the activity coefficients of Cs^+ and I^- ions due to alteration of the ionic strength of the solution by the water radiolysis products. The main steady-state water radiation products are hydrogen gas, hydrogen peroxide and protons. Hydrogen is a strong reduction agent. It cannot significantly influence the solubility of CsI, as it can neither reduce this salt, nor change the solution ionic strength (not being an ion itself). Hydrogen peroxide is an oxidizer and, being a good solvent similar to water; it is unlikely it may decrease the solubility of CsI. Conversely, solvated protons are ions that can significantly alter the ionic strength of the solution, and, through that, change the CsI solubility. Note, that low pH typically increases solubility of inorganic compounds (*e.g.* insoluble carbonates, sulfides, phosphates, hydroxides, *etc.*). Hence, the most plausible mechanism that can account for the crystal precipitation, growth and dissolution is the complex dynamics of local ionic strength of the solution mostly caused by solvated protons. Depending on the radiation dose, initial CsI concentration, and channel geometry (which limits diffusion), the radiation products shift the local chemical equilibrium favoring nucleation, growth or dissolution of the CsI crystals at different locations and times. Elucidation of the exact mechanism of this process would require solving a system of radiolysis reaction-diffusion equations under scanning beam excitation and specific geometry as well as extension of Debye-Huckel theory [246] to saturated CsI electrolyte. This, however, is outside the scope of the present work. As a concluding remark, we note that the rate of CsI crystal growth is almost linear and depends on the beam energy and current (Figure 4.7 (e)). The crystals have a clear non-dendritic shape and stop growing when the

electron beam is blanked (yellow curve, Figure 4.7 (e)). It is also noteworthy that the growing fronts of two adjacent crystals merge as they grow (Figure 4.7 (b-c)) and are not repelled due to precursor depletion as was observed for metallic particles before. Taken together, all these observations suggest a kinetic-limited adsorption, rather than diffusion-limited growth mechanism.

4.6 Combinatorial SEM studies

Similar to the microarray bioassays approach, the platform enables combinatorial/comparative SEM analysis of different liquid analytes simultaneously present in the MCA matrix (Figure 4.8 (a)). Here, three sections of an MCA sample were filled with water and solution of NaBr and LiBr. SEM imaging of all 3 sample sectors under the same conditions and detector settings allows for their direct and quantitative comparison. After identifying individual cells in each of the images (Figures 4.8 (b-d)) with an image recognition algorithm, we calculated mean signal intensity within the boundaries of each cell and plotted histograms of these mean cell intensities. Regions filled with water and NaBr electrolyte have very few empty or broken cells, and their histograms have one maximum at 100–104 units (Figure 4.8 (b,d)), whereas the LiBr histogram (Figure 4.8 (c)) breaks into two distinct distributions: empty cells with a maximum around 72 units and filled cells with a maximum around 97 units. Note, that a direct quantitative comparison of the gray scale values maxima: 97 units for LiBr, 100 units for water and 104 units for NaBr allows for prompt discrimination between different analytes using SEM images.

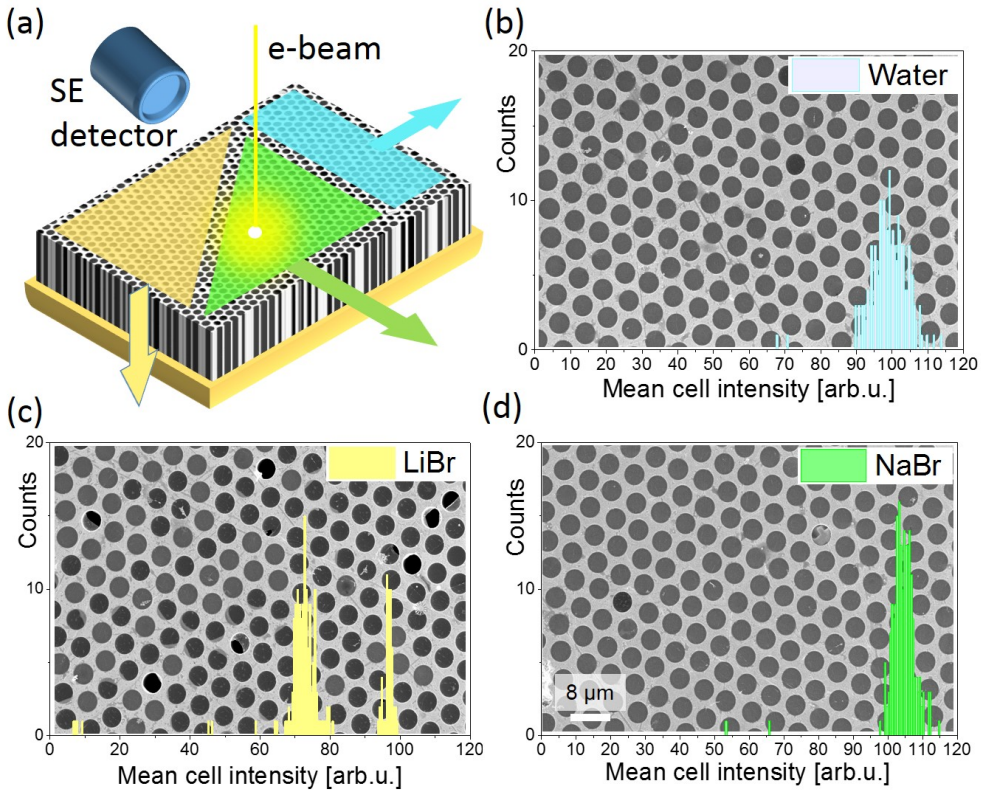

Figure 4.8: An example of combinatorial SEM imaging (E_b = 5 keV) using MCA platform. Three section of the bilayer graphene MCA sample were filled with water and 1 mol/L solutions of LiBr and NaBr and imaged with E-T detector under the same contrast brightness settings. (a) Schematic of the MCA sample with colored regions filled with different electrolytes. (b-d) SEM images and cell histograms of each region. Histograms show distribution of number of cells with a given mean cell signal intensity. Note, that the gold-coated matrix GSV of the images were excluded from analysis and not reflected in the histograms.

4.7 Summary

In summary, we have fabricated a novel sample platform for SEM experiments in liquids, which is based on a Gr-capped ordered array of microcapsules filled with liquid analyte(s). This array can retain liquid samples for more than 5 hours under HV, which is sufficient for routine electron imaging and spectroscopy experiments. Table 4.1 summarizes the ambient pressure EMS techniques enabled in a liquid cell MCA platform. We show that high electron transparency and mechanical strength of the bilayer Gr allow high resolution SEM imaging (including low voltage SEM), Auger and EDS spectroscopies to be done on samples of practical importance, such as water and other electrolytes. Typical experiments, such as electrochemical plating and crystal growth, were demonstrated as examples. Moreover, because the MCA platform is composed of a lattice of identical microcapsules, it can be used in conjunction with powerful statistical analysis, data mining, and pattern recognition methods. The latter allows for the study of the complex spectro-temporal and spatiotemporal behaviors at liquid-solid interfaces. Finally, this platform is not limited to SEM metrology but can be used in laboratory stand-alone or synchrotron based XPS, [247] PEEM, [109] and low energy electron microscopy (LEEM) setups.

Table 4.1: Ambient pressure EMS techniques enabled in a liquid cell MCA platform

In situ EMS techniques	Applications	Examples
SEM/EDS	• Nanoscale SEM microscopy/EDS spectroscopy in liquids; • Lifetime analysis of MCA liquid samples based on SEM sensitivity to empty/liquid cell and statistical approach; • Radiolysis studies; • Characterization of electrochemical reactions: particle nucleation, agglomeration, and dissolution; • Studies of electron beam induced crystal growth; • Comparative analysis based on SE yield of different liquid samples under the same imaging conditions	Figures 4.2, 4.3, 4.4, 4.6, 4.7, 4.8
AES	• Surface/interface sensitive spectroscopy of liquid samples; • Quantification of the signal attenuation in the Gr membrane	Figure 4.4
PEEM	Spatially resolved XAS studies of liquid samples	Figure 4.5
XPS	Wide field of view spectroscopy (>100 μm)	Outlook

Chapter 5: Effects of oxidation and charging rate on Li plating at carbon anodes of all-solid-state batteries

Li metal is the preferred anode material for all-solid-state Li batteries due to its high theoretical capacity and low voltage vs. standard hydrogen electrode. However, stable plating and stripping of Li metal in contact with a solid electrolyte at high current density ($>10\,\mathrm{mA/cm^2}$) remains a significant challenge due to formation of highly non-uniform morphology and penetration of the electrolyte by metallic Li filaments. To better understand the fundamental mechanism of Li metal plating, we use *operando* electron microscopy and Auger spectroscopy to probe nucleation, growth, and stripping of Li metal during electrochemical cycling of a solid-state Li battery as a function of current density and oxygen pressure. We find a linear correlation between the nucleation density of lithium clusters and the charging rate, which agrees with a classical thin film nucleation and growth model. Following nucleation, Li growth proceeds in the form of nanowires (NWs), a process promoted by the formation of a thin lithium oxide shell on the surface of the metallic Li by reaction with residual oxidizing gases in UHV. Surprisingly, we find that increasing partial pressure of O_2 to $\sim 10^{-5}$ Pa causes Li plating to proceed mostly by nucleation of new 3D clusters, thus turning a mostly out-of-plane nanowire growth mode into an in-plane growth mode. This chapter is adapted from Ref. [248]

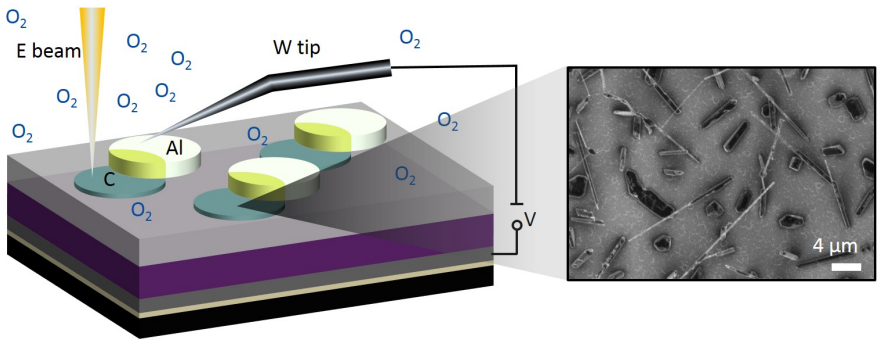

5.1 Motivation

Li metal is an attractive anode material for SSLIBs due to its high theoretical capacity (3,860 $mAhg^{-1}$) and low voltage vs. standard hydrogen electrode (- 3.040 V). [249–251] However, stable plating and stripping of Li metal electrodes in contact with a solid-state electrolyte (SSE) remains a significant challenge, even when the Li/SSE interface is thermodynamically or kinetically stabilized. [252, 253] In order to match the energy capacity of a typical Li-ion coin cell, a relatively thick Li metal film of $\sim$20 μm is needed. [253] Non-uniform plating/stripping of such thick layer and void formation at the Li/SSE interface can cause failure due to the severe mechanical strains and increased charge transfer resistance because of reduced electrode/SSE interface area. [254–256] An additional problem with elemental Li anodes is the observed shorting of the cells by metallic Li filaments growing through grain boundaries of crystalline SSEs. [257] Both issues become particularly problematic for current densities exceeding $\sim$1 mA/cm^2, which is still well below the $>$10 mA/cm^2 requirement for portable electronics and electric vehicle applications. [94] Improvements in plated Li metal morphology and suppression of dendrite formation at current densities as high as 10 mA/cm^2 have recently been demonstrated in a highly concentrated liquid ether based electrolyte with lithium bis(fluorosulfonyl)imide salt, illustrating the important role that surface chemistry can play in the evolution of Li during plating and dissolution. [258] Advances in controlling Li metal morphology have also been reported for promising garnet SSEs using a thin amorphous Si or Al_2O_3 coating to improve the surface wetting character-

istics resulting in stable cycling for current density as high as $0.2\,\mathrm{mA/cm^2}$. [259,260] Further advances in controlling Li morphology, however, require detailed understanding of Li growth mechanism during plating and dissolution, as well as the effects that the substrate and the surrounding environment (*i.e.* adsorbates) have on this process. [101,102,261]

To address this need, we use *operando* variable pressure SEM and AES to measure nucleation, growth, and stripping of Li metal anode in a thin film SSLIB as a function of current density and oxygen partial pressure. Previously, *operando* UHV SEM was used retrofitted with an electrical nanomanipulator probe to capture, in real time, the microstructure evolution of an Al anode during its lithiation and delithiation reactions. It was also demonstrated how chemical side reactions on the anode surface and anode/current collector interface profoundly affect battery capacity retention. [98,99] In Chapter 5, we extend this approach to characterize Li metal plating and stripping on an ultra-thin carbon electrode deposited on amorphous, nitrogen doped LiPON SSE and a lithium cobalt oxide ($LiCoO_2$) cathode. Our observations reveal a linear correlation between the nucleation density of lithium clusters and the charging rate, which agrees well with the classical 2D model of nucleation and growth. Surprisingly, the morphology of metallic Li deposition drastically changes from in-plane growth mode to out-of-plane whisker-like growth once the oxygen pressure in UHV chamber increases from $\sim 10^{-7}\,\mathrm{Pa}$ to $\sim 10^{-6}\,\mathrm{Pa}$. However, the in-plane Li growth mode is again recovered once the oxygen pressure further rises to $10^{-5}\,\mathrm{Pa}$.

5.2 All-solid-state battery fabrication

The structure of the battery and the experimental set-up are illustrated in Figure 5.1. Arrays of SSLIBs are fabricated on a Si (001) wafer covered with a 100 nm thermal SiO_2. A 90 nm Pt/30 nm Ti current collector is deposited using an electron beam evaporation followed by a 345 nm thick $LiCoO_2$ cathode deposited by radio frequency sputtering using previously described conditions. [262] Following deposition, the $LiCoO_2$ is annealed in O_2 atmosphere at 700 °C for 2 hours to form the high-temperature phase. A 340 nm thick LiPON electrolyte layer is sputtered on top of the cathode layer. Next, an array of amorphous carbon anodes with thickness of ≈35 nm is evaporated through a stencil mask with diameter of 0.51 mm. Then ≈210 nm thick Al pads have been evaporated through the same shadow mask but with a significant offset to leave most of the carbon anode surface exposed. The Al pads are used to make electrical contact to the carbon anodes.

All *operando* measurements are carried out in a UHV-SEM system with a base pressure of 10^{-7} Pa which has been previously described in Ref. [98] Electrochemical charging and discharging of the SSLIBs are carried out using a commercial current voltage source measure unit in a 2-electrode configuration with the cathode serving as the working electrode and the anode as the counter and reference electrode. Characterization of pristine carbon anodes using Raman spectroscopy and HRTEM shows that the thin carbon films are amorphous, without pores, and composed of 2 nm to 5 nm diameter fullerene-like clusters (Figure 5.2 (a,c)). Electron diffraction also indicates short range ordering typical for amorphous carbons (Figure 5.2 (c)).

XPS reveals preferentially sp^3 bonding of carbon atoms in the films (Figure 5.2 (d)). Low-loss and core loss electron energy-loss spectroscopy (EELS) analyses support the dominance of the sp^3 bonding at the surface. In low-loss EELS, the bulk plasmon is observed at 28 eV energy loss, suggesting that the sp^3/sp^2 ratio is ~1.5. [263] In core loss EELS, the net C K-edge at 284 eV energy loss reveals a barely visible $\pi*$-peak at about 289 eV followed by a broader dominating $\sigma*$-peak at 300 eV energy loss (Figure 5.2 (e,f)). The significant presence of the C-O and carbonyl groups can also be observed at the surface. Finally, EDS shows a very low oxygen bulk concentration, likely originating from carbonyl, carboxyl, and hydroxyl groups adsorbed by carbon, presumably, during the sample exposure to ambient air.

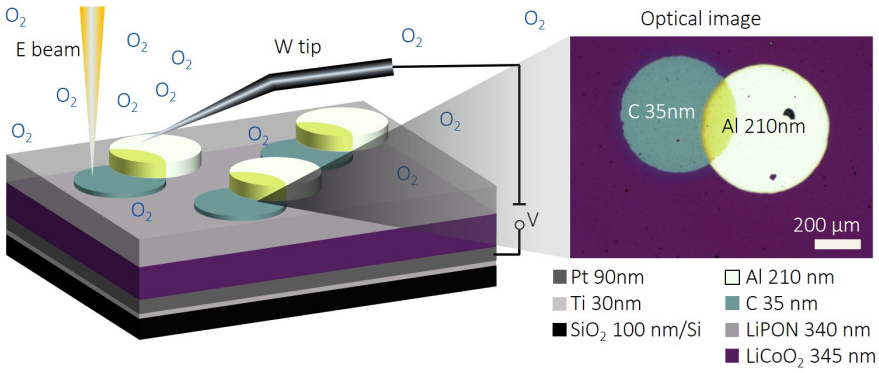

Figure 5.1: (Left) Schematic of experimental setup used to cycle the all-solid-state batteries in an SEM with controlled concentration of O_2. The grounded tungsten (W) tip is used to contact the C-Al anode. A potential is applied to the Pt-Ti current collector electrode to charge/ discharge the electrochemical cell. (Right) Real color optical image of C-Al anode in a representative device.

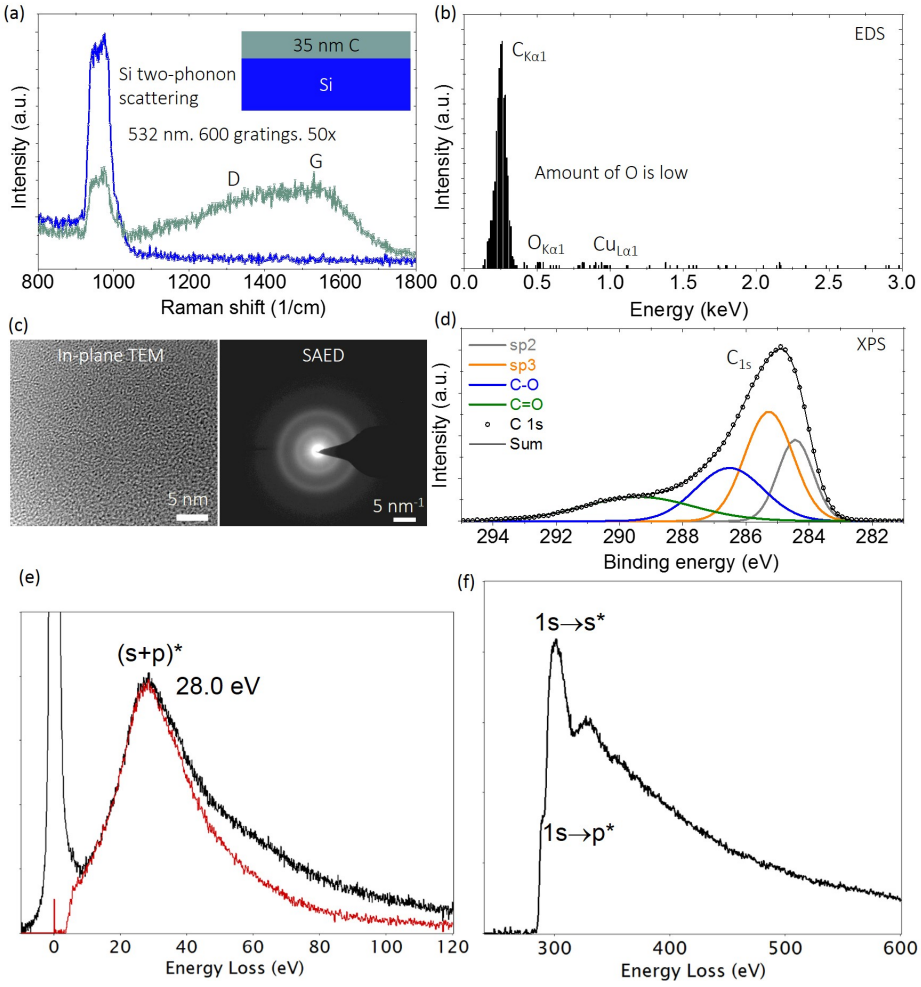

Figure 5.2: Carbon anode characterization. (a) Raman spectra obtained from a 35 nm C film e-beam evaporated onto a Si substrate (black) and a pristine Si substrate (blue). (b) EDS spectrum of a suspended C film. Cu residual peaks are due to a metal frame supporting C film. (c) In-plane HRTEM image (left) shows homogenous featureless C film with no pores composed of 2 nm to 5 nm diameter fullerene-like clusters. The SAED pattern (right) displays two broad rings with interatomic spacing of 0.12 nm and 0.22 nm, respectively, indicating short range ordering typical for amorphous carbons. (d) XPS signal acquired from a 35 nm C film. C_{1s} is fitted after Shirley background subtraction. (e) Low-loss and (f) core loss EELS of a suspended carbon anode film. The black curve in (e) denotes an original spectral intensity with the bulk plasmon at 28 eV energy loss. The single scattering distribution derived by a Fourier-log deconvolution of the original spectrum [264] is shown in red.

5.3 *Operando* characterization of battery performance

The nucleation, growth, and dissolution of Li nanowires on the carbon anode at constant current density of $0.1\,\mathrm{mA/cm^2}$ are shown in Figure 5.3. Formation of metallic Li nuclei visible in the SEM (Figure 5.3 (b)) occurs at $\approx 4\,\mathrm{V}$ cell potential, which is also seen as a 'kink' in the potential *versus* time curve (Figure 5.3 (g)). Following the nucleation stage, Li clusters grow out-of-plane, forming Li nanowires (Figure 5.3 (c)), which rapidly populate the entire C pad surface. Interestingly, the growth behavior of Li NWs changes from vertical out-of-plane elongation to lateral growth (increasing diameter) if they contact the carbon anode surface along their length, such as due to bending. Examples of this change in growth mode are highlighted by white dashed contours in Figures 5.3 (c-e) and illustrated schematically in Figure 5.3 (h): two initially separated Li NWs (Figure 5.3 (c) merge together after attaching to the C anode along the whole NW length. For out-of-plane NW growth, Li is supplied exclusively through the NW base/C-anode interface. However, if a NW leans and physically contacts the substrate along its long axis, it begins to expand its diameter through a newly formed interface supplied with Li atoms. It is important to note that upon discharging almost all Li NWs and clusters undergo dissolution leaving only characteristic bright sheaths composed of lithium oxides, hydroxides or carbonates (Figure 5.3 (f)) on the C pad.

Before considering the growth mechanism of Li nanowires, we discuss how the nucleation density of plated Li clusters depends on the charging current density. Figure 5.4 (a) shows the areal density of Li clusters *versus* the state-of-charge

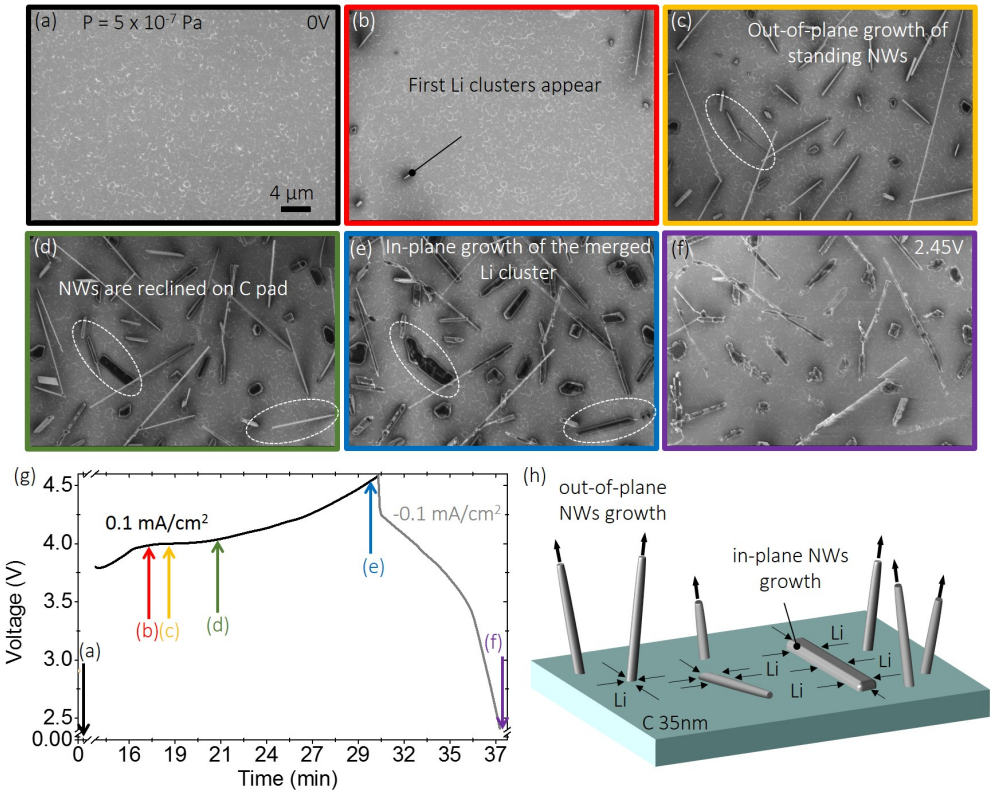

Figure 5.3: *Operando* imaging Li nucleation and growth at 0.1 mA/cm^2. *Operando* SEM micrographs showing (a) pristine carbon surface, (b) the initial nucleation of Li deposits at ≈4 V, (c) out-of-plane growth of free-standing Li NWs, (d) coalescence of in-plane Li NWs, (e) Li deposits at 4.6 V, and (f) the carbon surface at 2.45 V after Li was stripped. The regions highlighted by the white dashed contours indicate the Li NWs that grow initially out-of-plane (free standing) and eventually in-plane reclined at the substrate. (g) Galvanostatic charging/discharging curve. The color-coded arrows depict the time when each SEM image was acquired. (h) Schematic depicting in- and out-of-plane growth direction of the Li NWs.

for different current densities of $0.026\,\mathrm{mA/cm^2}$, $0.08\,\mathrm{mA/cm^2}$, $0.17\,\mathrm{mA/cm^2}$, and $0.26\,\mathrm{mA/cm^2}$. The nucleation density is estimated using corresponding SEM images in Figure 5.5. Independently of charging rate, the Li nucleation initiates at $\approx 2.5{\times}10^{-4}\,\mathrm{C}$ and $\approx 4\,\mathrm{V}$, which corresponds to oversaturation regime of C anode (Li concentration >100%, assuming a C_6Li stoichiometry) (Figure 5.4 (b)). The number of Li clusters grows rapidly until it reaches a steady state where no new clusters appear, indicating that lithium transported from cathode to anode contribute predominantly to cluster growth rather nucleation. The nucleation density at a steady state increases linearly with a current density (Figure 5.4, inset).

In order to quantify the Li nucleation kinetics in our experiment, we adopted a classical thin film nucleation and growth model (see reviews [265,266] and references therein). According to this model, guest atoms deposited onto the host substrate form either continuous film or discontinuous nanostructures depending on thermodynamic and kinetic parameters. By analogy with this model, Li-ions are driven from the cathode through SSE to C anode during battery charging and become reduced to metallic form at the anode. Upon oversaturation of the carbon anode, atoms of metallic lithium laterally diffuse both inside C anode and at C-vacuum interface, forming Li clusters, which further grow as nanoparticles. The SE yield of metallic lithium is lower compared to one from C anode, [192, 267] resulting in corresponding contrast difference in images Figure 5.3 (a-f). Following the close analogy between electrochemical Li plating and film growth by physical vapor deposition, the nucleation density of Li clusters, N, at a steady state in vacuum can be expressed by:

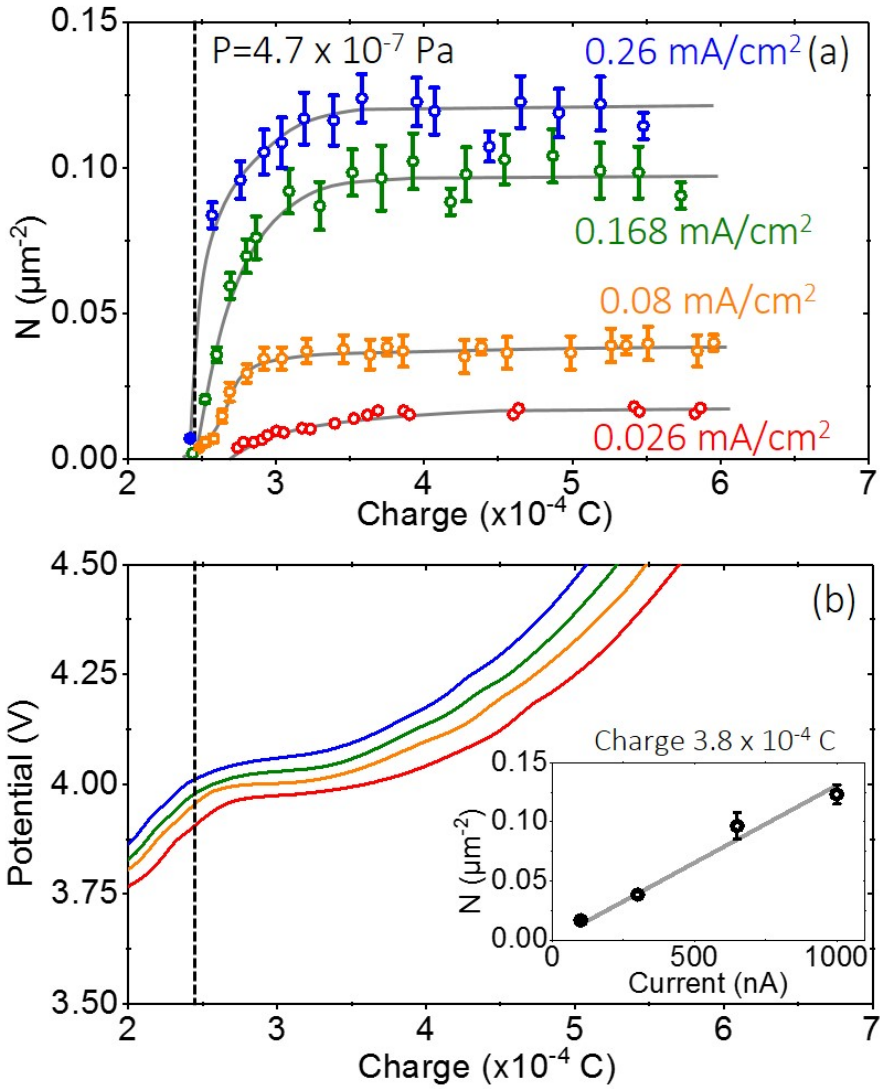

Figure 5.4: Dependence of the Li cluster nucleation density on a current rate. (a) Nucleation density and (b) potential as a function of the battery state-of-charge for 0.026 mA/cm^2 (red), 0.08 mA/cm^2 (orange), 0.168 mA/cm^2 (green), and 0.26 mA/cm^2 (blue), respectively. Gray lines in (a) serve as a guide to the eye. The inset in (b) depicts the nucleation density behavior, N, *versus* the charging current at a steady state. The error bars correspond to an uncertainty of nucleation pattern recognition at the boarders of the SEM field of view.

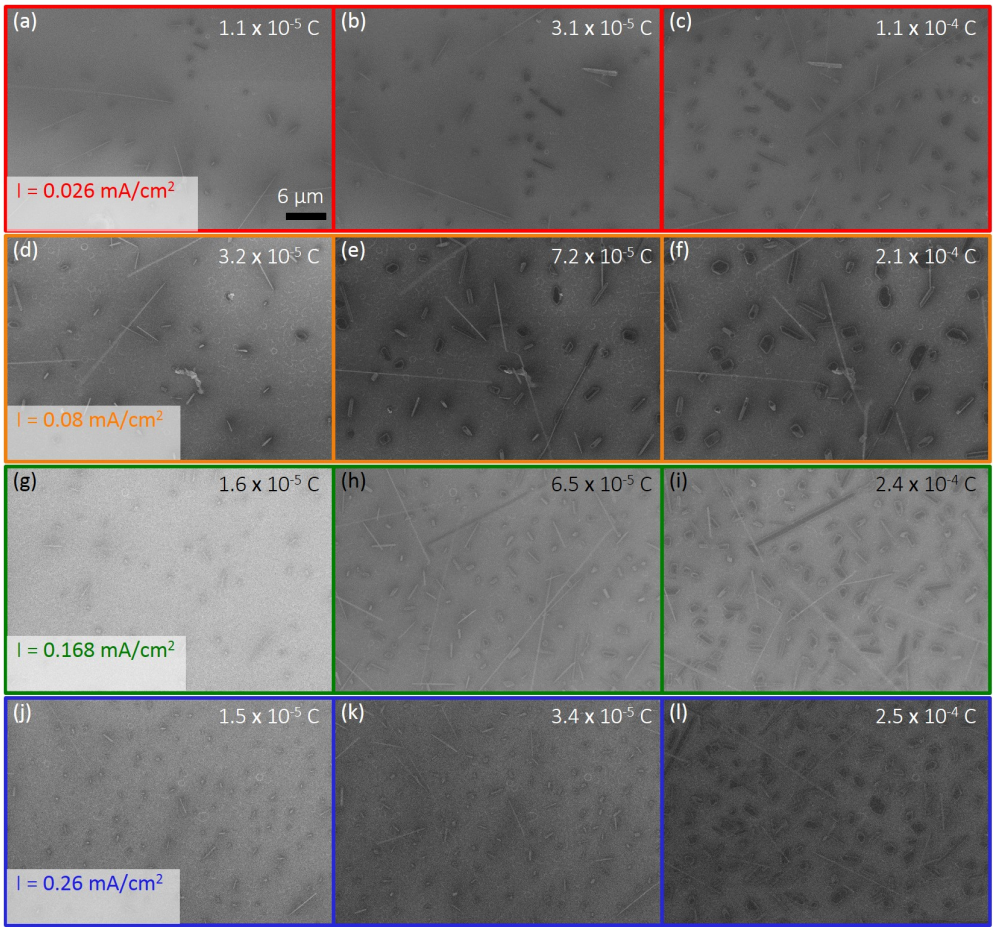

Figure 5.5: SEM images showing the Li nucleation density evolution for charging rates of (a-c) 0.026 $\mathrm{mA/cm^2}$ (red), (d-f) 0.08 $\mathrm{mA/cm^2}$ (orange), (g-i) 0.168 $\mathrm{mA/cm^2}$ (green), and (j-l) 0.26 $\mathrm{mA/cm^2}$ (blue), respectively.

$$N \propto \left(\frac{J}{D}\right)^{\frac{z}{z+2}}, \tag{5.1}$$

where J, D, and z stand for the current (flux of Li atoms), surface diffusion coefficient, and a minimal number of atoms in a thermodynamically stable cluster. Usually, the critical nucleus consists of a few hundred atoms [268] and, therefore, the nucleation density is approximately linearly proportional to the current at a constant diffusion coefficient. This dependence is observed in our experimental data (see inset in Figure 5.4 (b)), validating the applicability of this approach to our system.

As we indicated earlier, the Li nanowires are covered by a thin oxide/hydroxide layer. To gain better understanding of how this oxide develops, we use *operando* AES to monitor O_{KLL} and C_{KLL} signal evolution during battery cycling at $4.7{\times}10^{-7}$ Pa. The region of the signal acquisition and AES spectrum from a pristine C-anode are shown in Figure 5.6 (a) and (b), respectively. The AES spectrum indicates the presence of C_{KLL} and O_{KLL} peaks only, with no other elements present in detectable concentrations. AES spectra are acquired from different representative regions to avoid e-beam induced effects on oxidation. During the first cycle at $0.13\,\mathrm{mA/cm^2}$ charging current density, the intensity ratio O_{KLL}/C_{KLL} increases from 0.3 to 3.5, suggesting lithium cluster oxidation by gaseous and/or pre-adsorbed oxidative species. Interestingly, the comparison of AES spectra acquired from Li clusters and lithiated carbon regions manifests higher degree of oxidation of lithiated

carbon rather than pristine Li deposits (Figure 5.6 (e-f)). This could be due to higher concentration of pre-adsorbed oxygen in the amorphous carbon compared to metallic Li particles.

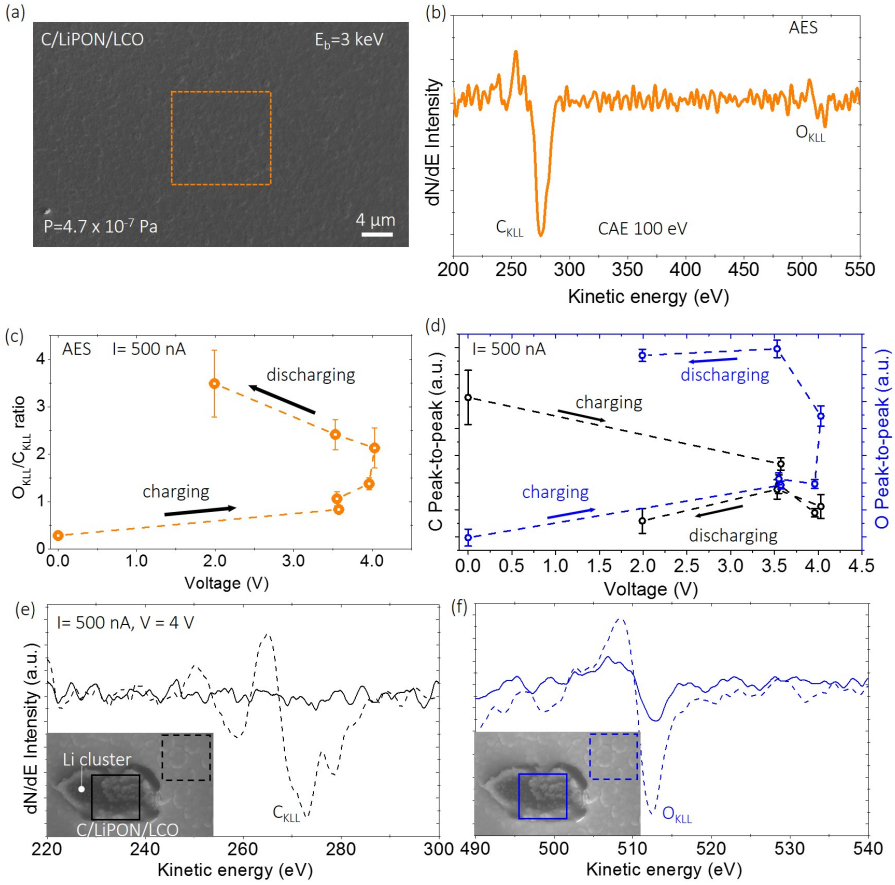

Figure 5.6: *Operando* AES of Li plating. (a) SEM image of the pristine battery with C anode before charging. The orange box shows the region where AES signal was obtained. (b) AES spectrum from the pristine battery with C anode. (c) Evolution of O to C ratio of Auger peaks obtained from C anode during battery operation. Error bars correspond to the level of AES background noise. (d) C and O AES peak evolution during battery charging. C_{KLL} (e) and O_{KLL} (f) AES spectra acquired from Li cluster and lithiated C anode at ≈4 V. Insets depict the corresponding regions where AES signals were collected.

Because Li is highly reactive, any oxygen containing species from the ambient

will form lithium oxide or hydroxides on the metallic cluster surface. To elucidate how the partial pressure of oxygen affects Li growth, we characterize Li plating as a function of oxygen pressure in the range of 5×10^{-7} Pa to 5×10^{-5} Pa. SEM images in Figure 5.7 (a-c) depict the Li particles plated at 0.77 mA/cm^2 current density under 5.7×10^{-7} Pa, 5.7×10^{-6} Pa, and 4.8×10^{-5} Pa oxygen pressure, respectively. The out-of-plane Li NW growth is observed only at the intermediate O_2 partial pressure range (Figure 5.7 (b)), whereas at lower partial pressure Li growth proceeds by cluster nucleation/ripening (Figure 5.7 (a)) and at higher pressure growth proceeds by constant cluster nucleation. Comparing nucleation density of Li deposits at 5.7×10^{-7} Pa and 4.8×10^{-5} Pa results in (i) three-fold increase of nucleation density due to thicker lithium oxide shell formation. This is supported by SEM contrast inversion due to increased charging of oxidized Li nanostructures under an e-beam exposure (Figure 5.7 (c)). Our proposed mechanism of the oxidation effect on Li deposit morphology surmises that metallic lithium possessing the body-centered cubic (BCC) crystal structure nucleates and grows as 3D microparticles at carbon anode-vacuum interface under UHV conditions (Figure 5.7 (d)). The characteristic faceting observed for each Li particle in Figure 5.7 (a) supports the crystalline nature of the metallic nanostructures. However, the SEM image in Figure 5.7 (b) shows that a sheath forms around the metallic lithium core under low concentration of oxygen traces. In our picture for lithium oxide sheath formation, we posit a commensurate flux of Li and O to the surface for the formation of stable lithium oxide surfaces. For a pressure of 5.7×10^{-6} Pa, the O flux rate is, 4.8×10^{13} (s$\cdot$ cm^2)$^{-1}$, which is 100 times smaller than the Li current J. However, only a fraction of

the intercalated Li nucleates at the surface. Assuming that surface nucleation is thermally activated, we have $\frac{dN_{surface}}{dt} = \nu \cdot N_{subsurface} \cdot e^{\frac{-E_a}{k_B T}}$, where ν is the attempt frequency $\frac{k_B T}{h} \approx 10^{13}\, s^{-1}$, E_a is the activation energy of Li atoms to reach the surface, $N_{surface}$, and $N_{subsurface}$ are the 2D Li densities immediately on and below the surface, respectively. The time scale for the measurement ensures that the volume density reaches approximately steady state, so $N_{subsurface}$ is given by $Jt(a/d)$, where a is the lattice constant, d is the graphite layer thickness, and t is time. We find that the surface nucleation rate is close to the O impinging rate for E_a =0.9 eV. This activation energy can be compared to the surface energy at the surface of lithium oxide because both indicate the energy cost of breaking atomic bonds in the bulk compared with forming bonds. The surface energy of lithium oxide is computed to be 1.2 eV/a^2 to 1.3 eV/a^2, [269] where a is the in-plane lattice constant of the low energy (111) surface of Li_2O. The presence of a stable sheath passivates the surface from rapid bulk oxidation and inhibits lateral diffusion [270,271] due to high activation energy. Therefore, the volume expansion during charging can only occur through the out-of-plane elongation resulting in 1D growth (Figure 5.7 (e)). Similar considerations have been proposed for oxygen assisted growth of Si nanowires. [272] Additionally, the mechanical response of lithium oxide nanowires indicates that they are highly ductile. [273] As the Li nanowires grow, any newly emerged Li surface at the NW footprint gets immediately oxidized, thus forcing one-dimensional growth. At higher oxygen partial pressure, a thick and mechanically robust oxide shell is formed around each cluster (Figure 5.7 (f)) and the Li current contributes mostly to nucleation of new Li nanostructures rather than to growth of the pre-existing ones.

To describe the changes in nucleation density in the presence of oxygen, we extend the 2D model of Li nucleation and growth by considering the second species (O) diffusing across the carbon anode. Following the atomistic nucleation formalism for oxygen and lithium atoms, we modify eq. 5.1 using the generalized formula for two species:

$$N \propto ((z+k+2)(\sigma_{Li}J + \sigma_O P)\frac{I^z P^k}{D})^{\frac{1}{k+z+2}}, \tag{5.2}$$

where P, σ_{Li}, σ_O, z, and k represent the oxygen pressure, capture numbers of clusters to absorb Li or O adatoms, and a minimal number of Li and O atoms in a stable cluster, respectively. For negligible amount of oxygen, P≈0 and k≈0, the expression 5.2 reduces to eq. 5.1. In case of significant oxygen flux, a critical cluster can comprise only a few atoms, and dependence of N on Li current and oxygen pressure becomes sublinear supporting semi-quantitatively the experimental results.

Grazing angle SEM imaging of Li plating (Figure 5.8) supports the root-growth mechanism of out-of-plane Li deposits. Using the kink in the Li NW as a fiducial point, one can notice that the growth occurs at the Li nanostructure-C interface, pushing the whole NW in direction normal to the C-anode plane. In addition, comparison of high tilt angle SEM micrographs of Li NWs with the shells left after discharge (Figure 5.9), suggests that the oxide sheath is a few tens of nanometer thick. Upon discharging, the SEM image illustrates the void formation in the middle of NWs due to metallic Li dissolution, leaving only the sheaths at the C-anode.

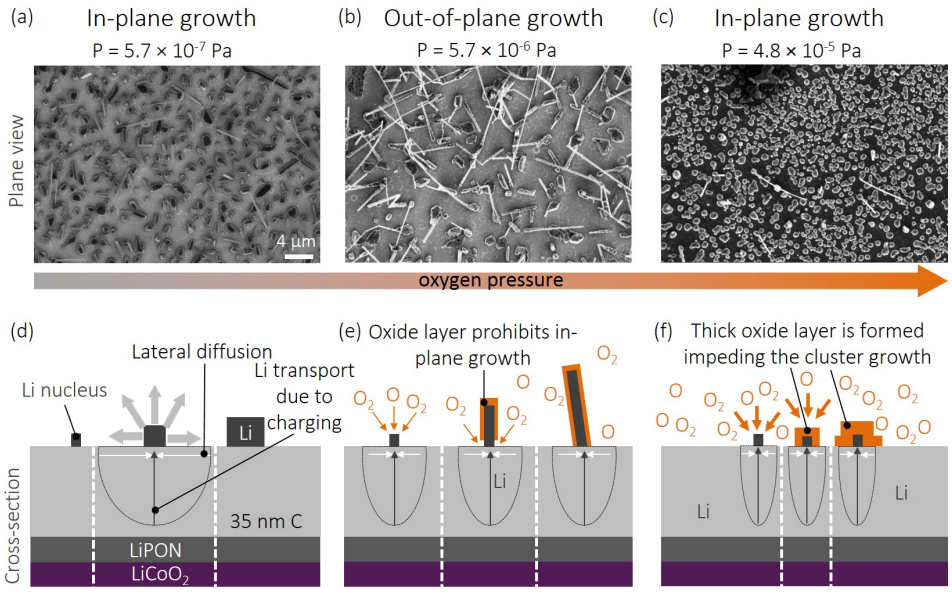

Figure 5.7: Effect of oxygen pressure on Li plating morphology. (a-c) SEM images of Li plated at 5.7×10^{-7} Pa, 5.7×10^{-6} Pa, and 4.8×10^{-5} Pa residual O pressure, respectively; 0.77 mA/cm^2 current density. (d-f) Schematics showing the Li nucleation and growth for the images presented in (a-c). In the presence of oxygen, a lithium oxide sheath is developed.

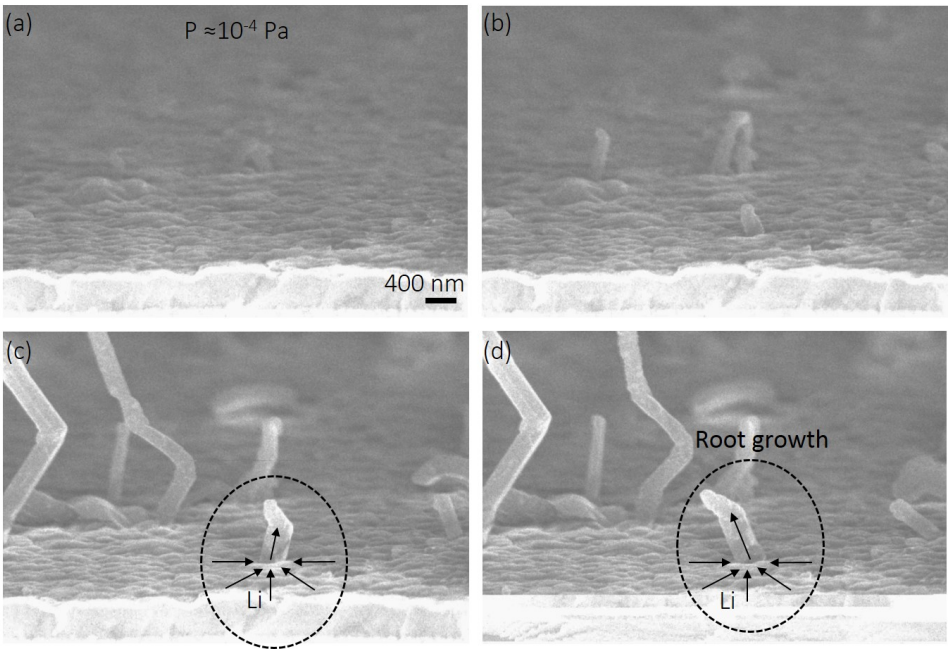

Figure 5.8: Cross-section SEM images of the Li plating, showing a root growth behavior. The SEM images depict (a) the pristine battery, (b) nucleation of the Li deposits, (c-d) Li NW growth.

Finally, we briefly discuss the effects of e-beam irradiation during Li plating experiments. The e-beam can appreciably increase the Li oxidation rate, resulting in corresponding changes in nucleation density and morphology of Li deposits. Figure 5.10 (a) and (b) depict the SEM images obtained after Li is plated at 5.73×10^{-6} Pa and 4.8×10^{-5} Pa oxygen pressures, respectively. The rectangle regions in both micrographs were exposed to e-beam during cycling, resulting in changes of both nucleation density and Li cluster morphology compared to unexposed regions. In case of battery charging at 5.7×10^{-6} Pa residual pressure, the region exposed to the e-beam demonstrates suppression of Li NWs. However, lithium deposition at 4.8×10^{-5} Pa under e-beam radiation shows higher nucleation density than one without the e-beam exposure. Moreover, the SEM images (Figure 5.10 (a) and (b)) depict that C-anode regions of $\approx5\,\mu$m near the perimeter of exposed areas are depleted in Li particles, suggesting the unidirectional Li transport and trapping at irradiated zones. Our results suggest that the e-beam radiation locally increases oxidation kinetics due to e-beam induced oxygen dissociation. [274] The observed phenomenon can be used to control the degree of oxidation and morphology variation of Li deposits with high spatial resolution.

5.4 Summary

In summary, we used *operando* SEM to investigate Li plating in a thin film solid state battery and the effects of O_2 partial pressure on the metallic Li morphology. At the lowest O_2 partial pressure of $\sim 10^{-7}$ Pa, Li plating proceeds by classic nucleation

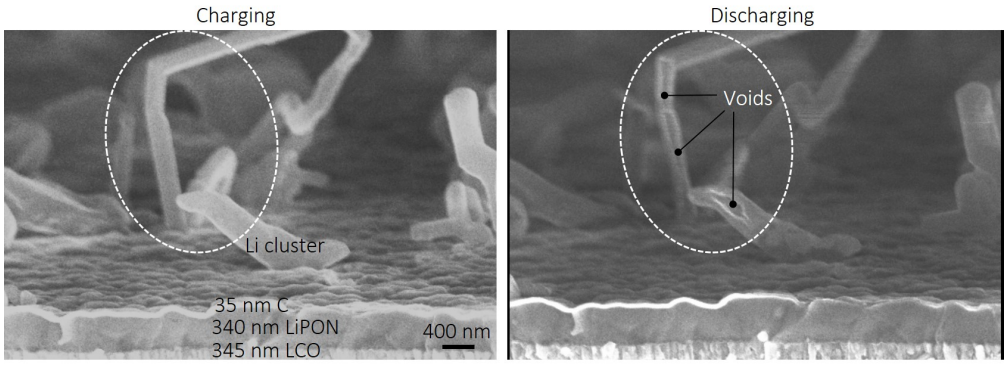

Figure 5.9: Cross-section SEM image of the sample, showing Li NWs during battery charging and discharging. Upon discharging, voids are formed in the middle of NWs due to metallic Li dissolution, leaving only the sheaths at the C-anode.

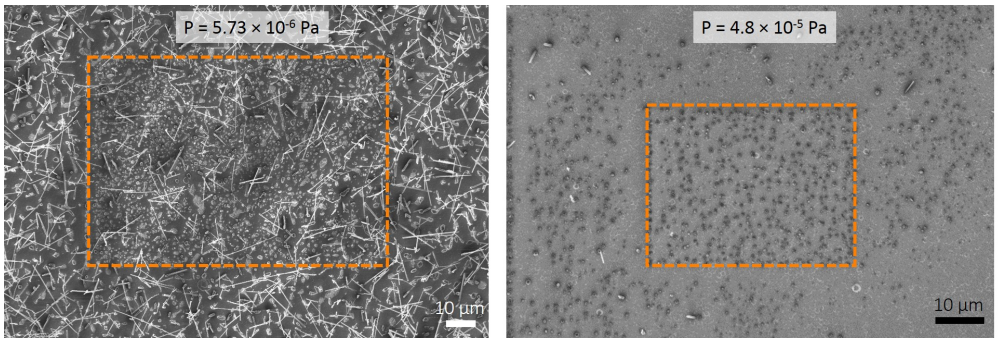

Figure 5.10: E-beam induced effects increase oxidation rates. The battery is charged at (a) 5.73×10^{-6} Pa and (b) 4.8×10^{-5} Pa. Orange dashed boxes show the regions exposed to the e-beam during battery cycling.

growth that produces planar deposits. At intermediate O_2 partial pressure of $\sim 10^{-6}$ Pa, the oxide sheath formed around the growing Li nanostructures leads to nanowire growth, while at still higher pressure of $\sim 10^{-5}$ Pa, the thicker oxide shell prevents Li growth beyond nucleation, leading again to planar deposits. Our results demonstrate the sensitivity of Li plating to reactive impurities and the usefulness of *operando* SEM for characterizing solid state electrochemical processes.

Chapter 6: Conclusions and Outlook

In conclusion, we demonstrated a series of novel opportunities for *in situ*/ *operando* characterization of liquid and reactive samples using electron microscopy and spectroscopy methods. Our approach implements carbon-based membranes and anodes such as Gr, GO, and amorphous C, which offer minimal inelastic scattering of electrons due to their nanometer-scale thickness and low atomic number. Because of high electron transparency and mechanical/chemical stability of these materials, we were able to image and collect electron spectra from samples of interest capped with those membranes.

We developed and tested the encapsulation method based on self-assembling GO membranes. We proved that a wide range of solid, liquid, gaseous micro- and mesoscopic samples can be reliably adhered to a variety of substrates and encapsulated with an electron and optically transparent GO membranes using a simple drop casting method. We showed that the GO film thickness can be properly adjusted by varying the concentration of GO colloid solution and/or size of droplets. Depending on topography and hydrophobic properties of substrates, the ultimate encapsulation can exhibit different behavior such as covering, wrapping, and complete isolation of objects. The electron and optical transparency of GO films enabled

SEM/STEM imaging and EDS, AES, Raman, fluorescence spectroscopies of encapsulated objects. The proposed method of sample encapsulation with GO membranes can find broad applications in X-ray microtomography, flame photometry, mass-spectroscopy, micro-fluidic devices, histology, and forensics.

We proposed and tested the new technique of CVD-grown Gr transfer based on an anthracene sacrificial layer. After the transfer, the anthracene film sublimed at temperatures above 100 °C, releasing Gr. We quantified the cleanliness of the Gr using LVSEM, XPS, and TEM. The direct comparison with the commonly used methods such as the IPA assisted transfer and one based on a PMMA layer verified the advantages of our approach. For example, TEM analysis reveals the reduction of the contaminant density by 1 order of magnitude on Gr transferred using anthracene compared to the PMMA method. We envision that a novel Gr transfer procedure paves the way for integrating Gr with sensitive devices where exposure of the sample to moisture is prohibited, *e.g.* battery research.

We designed and characterized a platform made of thousands of identical isolated micro-containers capped with a Gr membrane for EMS characterization of liquid samples. The proposed platform enables wide FOV EMS including PEEM and conventional XPS. The liquid sample lifetime measurements confirmed that the time when the number of liquid cells halves under vacuum conditions is $\approx 2.7\,\mathrm{h}$, which is sufficient to perform comprehensive EMS characterization of a liquid sample. Both EDS and AES data collected from a water sample demonstrated unique capabilities of the platform to realize electron spectroscopy in liquids. Finally, the MCA platform opens a new horizon for combinatorial analysis of different samples

under the same EMS conditions.

The last chapter provided both qualitative and quantitative findings on the effects of oxidation and charging rates on a lithium plating morphology at C anodes in SSLIBs. *Operando* SEM and AES results indicated that even under UHV conditions, cycling of SSLIB resulted in significant Li oxidation at the battery anode. We employed the 2D nucleation and growth model to describe the linear dependence of Li nucleation density *versus* charging current. The conducted experiments supported the proposed theoretical assumption. We experimentally defined the narrow range of oxygen gas pressure ($\sim 10^{-6}$ Pa) that promotes out-of-plane NW-like growth of Li deposits during SSLIB cycling. Our results will help provide deeper insights into capacity loss mechanisms and define the risk-free parameter space for reliable SSLIB operation.

The future work would be to elucidate the details of Li-ion transport at anode-SSE interfaces during battery cycling. For that, we propose implementing graphene as an electron transparent anode for SSLIBs. This approach would allow for *operando* characterization of Gr-SSE interface using spatially resolved EMS analysis through the Gr anode. The main technical challenge would be to fabricate the proposed electrochemical cell because most SSEs (*e.g.* LiPON) are moister sensitive. Thus, a dry method of graphene transfer is required. The anthracene based method proposed and tested in Chapter 3 can overcome the processing challenges to obtain the graphene anode. In addition, the conformal coverage and, therefore, reliable electric contact between graphene and SSE would be a must. The preliminary results of this approach are shown in Figure 6.1. We fabricated a SSLIB made

of $LiCoO_2$ as a cathode, LiPON as a SSE, and Gr as an anode. The graphene was transferred using capillary effect of toluene, which should be chemically inert to LiPON. The sequence of SEM images in Figure 6.1 depicts the gradual lithiation of the SSLIB at galvanotactic mode (I = 30 nA). Performing EMS through the Gr can be helpful to reveal the kinetics of Li electrochemical deposition below the anode. The technical realization of the proposed approach requires further optimization of Gr transfer method to obtain conformal coverage of LiPON electrolyte with graphene.

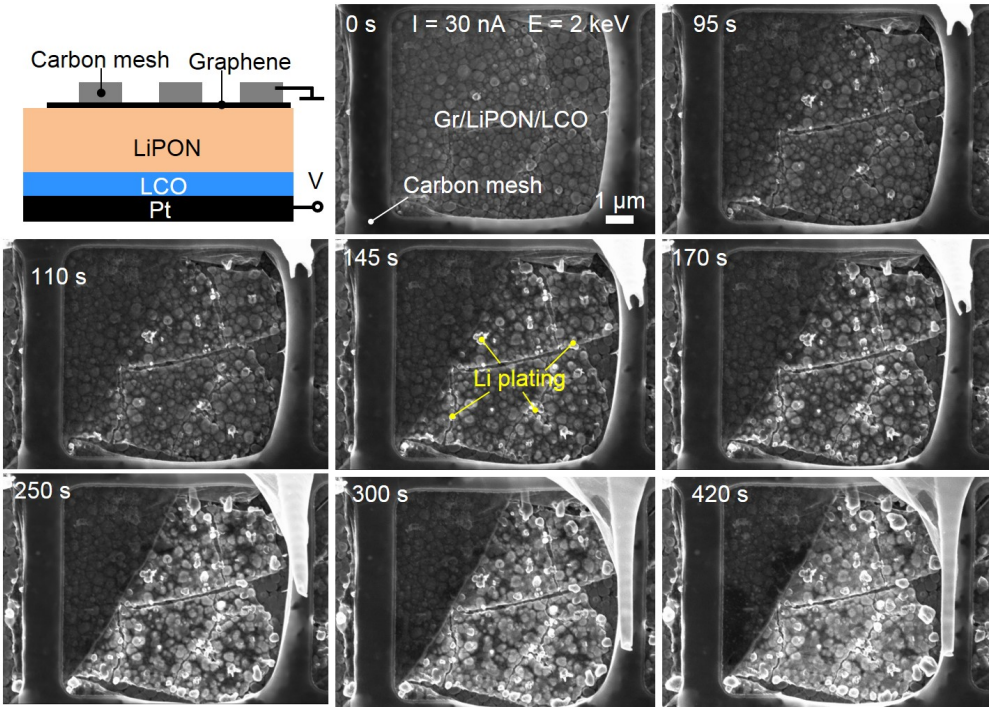

Figure 6.1: *Operando* SEM imaging of the Li deposition in SSLIB through an electron transparent graphene anode. The SEM images are collected at 95 s, 110 s, 145 s, 170 s, 250 s, 300 s, and 420 s during battery charging at 30 nA current.

Appendix A: Fabrication and characterization procedures

A.1 *EMS enabled through the encapsulation of objects by graphene oxide membranes*[1]

Sample Preparation: GO solution was fabricated according to standard Hummers' method followed by dispersing in water *via* sonication to obtain homogeneous suspension. [44, 45, 123, 148] Different concentrations of the solution ($0.02\,\mathrm{kg/m^3}$ – $1\,\mathrm{kg/m^3}$) were used to tune the thickness of the drop-cast membranes. SiO_2/Si wafers and different metal substrates were employed as solid supports for objects of interest. To study the effect of wetting on encapsulation dynamics, the surface was functionalized with a hydrophobic silane. Besides planar substrates, microchannel arrays made of a boron doped silicate glass were used. Hydrogen bubbles were produced in GO water solution by electrolysis. A water drop was placed on top of two copper electrodes, and a DC electrolysis was initiated. PDMS microparticles were synthesized using microfluidic setup. [149] PDMS microposts were created using standard photolithography based approach to fabricate elastomeric stamps for soft lithography. Water fleas (*Daphnia*) were transferred on a Si substrate with micropipette from culture liquid. The laboratory strain of *E.coli* bacteria and grass pollen were encapsulation by a similar drop casting procedure. All experiments involving biological samples – *Daphnia*, *E.coli* bacteria, and grass pollen - were conducted at the SIUC campus.

Imaging: An optical microscope and field emission SEM were employed to observe the encapsulation process and final products. The electron beam energy and type of an electron detector were varied to gain the desired contrast of encapsulated objects. Electron trajectory simulations were calculated by means of Monte Carlo simulation package. [163] For STEM, specimens were placed onto a 50 nm thick polyimide TEM grid. The latter was mounted on a carbon STEM holder with Au covered plate facing E-T detector. Electrons transmitted through the sample produced the image formed by a secondary electron signal scattered from the gold surface. Therefore, the image could be created concurrently by either conventional SE_1 scattered from the specimen and collected by TTL detector or by transmitted signal resulting in SE_2 and analyzed by E-T detector. Atomic force microscopy images were obtained in a tapping mode at a scan rate of 0.5 Hz.

Raman Spectroscopy: The Raman spectra were collected using a Raman mi-

[1] The text is adapted from Ref. [103]

croscope with a 532 nm excitation laser. Laser power was set to 2 mW. 25 μm slit aperture and 50× objective were used. The estimated spot size was 2.1 μm.

Auger Spectroscopy: For Auger spectroscopy, the samples were admitted to a UHV analytical chamber using standard load-lock system. No additional cleaning or baking procedures were undertaken. Auger electrons were excited by a 3 keV primary e-beam and collected at takeoff angle close to normal to the sample surface. Hemispherical electron energy analyzer was set to 100 eV pass energy.

A.2 *Anthracene as a sacrificial layer for clean transfer of CVD-grown graphene*[2]

Sample Preparation: Graphene was obtained using CVD method. Briefly, 125 μm thick copper foil was electropolished in phosphoric acid and annealed at 1065 °C under the flow of 2.5% H_2 in Ar for 30 min. Then, methane was added to atmosphere with a gradual increase in concentration up to 40 ppm. Finally, the sample was cooled down to room temperature. A 14 μm thick film of anthracene was deposited using thermal evaporation in a test tube evacuated down to 10^{-3} Pa. During evaporation, the Gr/Cu sample was maintained at -20 °C to minimize the grain size of the PAH film. The Cu substrate was etched in APS aqueous solution at 40 °C and anthracene/Gr stack was two times rinsed in a DI water bath to remove etchant residues. Finally, the anthracene/Gr was transferred onto the substrate of interest using a Pt loop. The sample was placed on a hot plate to desorb anthracene at 120 °C. For comparative analysis, a half of the carbon mesh was coated with 10 nm Pt; then, Gr was transferred onto the Pt coated and uncoated region of the carbon mesh. Cleaning using Pt catalysis was realized on a hot plate at 180 °C for 30 min. To perform the second cleaning, the carbon mesh with a suspended Gr was inserted into the activated C and annealed at 210 °C for 90 min.

Sample characterization: Raman spectra were acquired under ambient conditions with a micro-Raman spectrometer equipped with a 514.5 nm (2.41 eV) wavelength excitation laser and a grating with a 1800 mm^{-1} pitch, while operating in 180^o backscattering geometry. A 50× objective was used to focus the excitation laser to an approximately 1 μm spot onto the sample with an incident power of less than 2 mW to avoid local heating effects. Low voltage SEM was implemented to characterize suspended Gr. The contrast and brightness setting were fixed to perform measurements under the same imaging conditions.

A.3 *Graphene membranes for ambient pressure EMS*[3]

Sample Preparation: Graphene was grown on a Cu foil using a high pressure modification [40, 188] of the commonly used CVD method. As-grown graphene was transferred onto one side of commercially available glass multichannel arrays using

[2]The text is adapted from Ref. [107]

[3]The text is adapted from Ref. [108, 109]

PMMA as a sacrificial layer. [105] Briefly, a 200 nm PMMA film was spin-coated onto a graphene/Cu stack followed by etching copper in ammonium persulfate solution (APS) at 40 °C for 2 h. Then, the graphene monolayer was rinsed three times in deionized (DI) water and transferred onto another graphene/Cu foil. After annealing the sample on a hot plate for 2 h at 180 °C, etching in APS and rinsing in DI water were repeated again. A PMMA/bilayer graphene stack was transferred onto an MCA consisting of thousands of hollow straight channels with a diameter of 5 μm and 1:80 aspect ratio. Prior to graphene transfer, the MCA front surface was precoated with 200 nm/10 nm Au/Cr film serving as an adhesive layer for graphene and to minimize substrate charging during the SEM imaging. Then, the sample was annealed on the hot plate for 2 h at 180 °C again. For electrochemical measurements, the inner part of the channels at the backside of MCA was covered with a 40 nm Pt layer using ALD. After the transfer, the PMMA was dissolved in an acetone bath at 70 °C. Then, the acetone was gradually substituted with the IPA solution at 80 °C and then with DI water. For studies involving electrolytes, a droplet of the electrolyte was drop-casted onto the backside of the MCA. After a few minutes required for establishing concentration equilibrium, the excess of the droplet was removed with a filter paper and a UV-curable adhesive or liquid metal such as galinstan was applied to seal the liquid-containing MCA channels. The backside of the sample dedicated to combinatorial SEM imaging was prepatterned with strips of a hydrophobic layer before the liquid filling. This prevented cross-contamination between the analytes during application.

SEM Imaging: The sample was observed using a field emission scanning electron microscope. An EverhartThornley (E-T) detector sensitive to both SE and backscattered electrons (BSEs) was employed for SEM imaging. The SEM base pressure was $\approx 10^4$ Pa. The gray-scale value of the SEM images was linearly proportional to the intensity of scattered and secondary electrons collected by the detector. For lifetime measurements, the SEM images were obtained at 5 keV and a few tens pA primary electron beam. For EDS spectroscopy and mapping, the sample was probed by a 15 keV primary beam.

AES Analysis: The AES analysis was performed at room temperature in an ultrahigh vacuum (UHV) chamber at a base pressure of $\approx 10^7$ Pa. The AES spectra were collected at 3 or 5 keV primary electron beam energies and 400 pA current followed by spectra averaging over 19.6 μm^2 area of MCA channels. Radiolysis effects, such as hydrogen bubble formation, may strongly affect AES spectra collection. Only those filled channels which did not change their composition during AES acquisition were used for analysis. The peak-to-peak intensity was deduced from the differential spectra. To calculate the thicknesses of graphene and water layers, the attenuation formula [231] and corresponding set of parameters were used.

PEEM Setup: X-ray photoemission electron microscopy (X-PEEM) was conducted at the 10ID-1 SpectroMicroscopy Beamline of the Canadian Light Source (CLS), a 2.9 GeV synchrotron. The beamline photon energy covers the range from 130 to 2700 eV with an $\approx 10^{12}$ s^{-1} photon flux at the O K-edge (540 eV) and the beamline exit slit size set at 50 μm $\times$ 50 μm. The plane grating monochromator can deliver a spectral resolution of better than 0.1 eV in the measured energy range, and

the photon energy scale was calibrated based on samples with known XAS features. The monochromatic X-ray beam can be focused by an ellipsoidal mirror down to ≈20 μm spot and irradiated on the sample in PEEM at a grazing incidence angle of 16^o. The sample is biased at 20 kV with respect to PEEM objective. FOV image stacks (sequences) were acquired over a range of photon energies at the O K-edge. The incident beam intensity was measured by recording the photocurrent from an Au mesh located in the upstream part of the PEEM beamline and was used to normalize the PEEM data acquired from the sample ROIs.

A.4 *Effects of oxidation and charging rate on Li plating at carbon anodes of all-solid-state batteries*[4]

Sample Preparation: 100 nm thermal SiO_2 was obtained on Si (001) wafer *via* thermal oxidation in a furnace tube. Then, a 90 nm Pt/30 nm Ti was deposited using electron beam evaporation. A 345 nm thick $LiCoO_2$ cathode was sputtered in nitrogen plasma. The sample then underwent annealing in O_2 atmosphere for 2 hours at 700 °C to structurize the cathode. A 340 nm thick LiPON electrolyte film was sputtered on top of the cathode. An array of amorphous C anodes with thickness of 35 nm was deposited *via* thermal evaporation through a stencil mask with 0.51 mm orifices. Finally, 210 nm thick Al pads were deposited through the same mask with a significant offset.

Sample characterization: All measurements were conducted in UHV-SEM and AES system operating at 10^{-7} Pa base pressure. For AES measurements, 500 nA electron beam current and 100 eV CAE mode of electron energy analyzer were used. A current voltage source-measure unit with a two-electrode configuration was implemented to perform battery cycling. A W tip was used to contact Al current collector to charge/discharge battery. Raman setup equipped with 532 nm laser and 600 gratings was employed to collect the spectrum. The nucleation density was estimated based on SEM images. To control O_2 pressure in a vacuum chamber, a needle valve and turbo pump were used to inject the gas and evacuate the chamber, respectively.

[4]The text is adapted from Ref. [248]

Appendix B: List of Awards/Publications/Presentations

B.1 *Awards/Honors/Recognitions*

1. 2^{nd} Place Poster Award: AVS Mid-Atlantic Chapter DC Regional Meeting Gaithersburg, MD, May 25, 2017
2. Art Zone Contest Finalist: AVS 63^{rd} International Symposium & Exhibition - Nashville, TN, November 6–11, 2016
3. Poster Presentation Honorable Mention: AVS Mid-Atlantic Chapter DC Regional Meeting - Gaithersburg, MD, May 26, 2016

B.2 *Publications*

*(*equal contribution)*

1. **Alexander Yulaev*,** Hongxuan Guo*, Evgheni Strelcov*, Lei Chen, Ivan Vlassiouk, and Andrei Kolmakov, *"Graphene Microcapsule Arrays for Combinatorial Electron Microscopy and Spectroscopy in Liquids,"* ACS Applied Materials and Interfaces **9,** 26492, 2017, *front cover.*
2. Hongxuan Guo*, Evgheni Strelcov*, **Alexander Yulaev*,** Jian Wang, Narayana Appathurai, Stephen Urquhart, John Vinson, Subin Sahu, Michael P. Zwolak, and Andrei Kolmakov, *"Enabling photoemission electron microscopy in liquids via graphene-capped microchannel arrays,"* Nano Letters **17,** 1034, 2017.
3. **Alexander Yulaev,** Alexey Lipatov, Annie Xi Lu, Alexander Sinitskii, Marina S. Leite, and Andrei Kolmakov, *"Imaging and Analysis of Encapsulated Objects through Self-Assembled Electron and Optically Transparent Graphene Oxide Membranes,"* Advanced Materials Interfaces **4,** 2, 2017, *frontispiece.*
4. **Alexander Yulaev,** Guangjun Cheng, Angela R. Hight Walker, Ivan V. Vlassiouk, Alline Myers, Marina S. Leite, and Andrei Kolmakov, *"Toward Clean Suspended CVD Graphene,"* RSC Advances **6,** 83954, 2016.
5. Jürgen Kraus, Robert Reichelt, Sebastian Günther, Luca Gregoratti, Matteo Amati, Maya Kiskinova, **Alexander Yulaev,** Ivan Vlassiouk, Andrei Kolmakov, *"Photoelectron Spectroscopy of Wet and Gaseous Samples through Electron Transparent Graphene Membranes,"* Nanoscale **6,** 14394, 2014.

6. Slavomir Nemšák, Evgheni Strelcov, Tomáš Duchoň, Hongxuan Guo, Johanna Hackl, **Alexander Yulaev,** Ivan Vlassiouk, David N. Mueller, Claus M. Schneider, and Andrei Kolmakov, *"Interfacial Electrochemistry in Liquids Probed with Photoemission Electron Microscopy," Submitted,* 2017

7. **Alexander Yulaev,** Vladimir Oleshko, Jabez J. McClelland, Paul Haney, A. Alec Talin, Marina S. Leite, and Andrei Kolmakov, *"From Nanoclusters to Nanowires and Back: Radical Transformations in Plated Li Metal Morphology Observed Using* in-situ *Electron Microscopy," In preparation,* 2017.

B.3 *Conference Proceedings*

1. **Alexander Yulaev,** A. Alec Talin, Marina S. Leite, and Andrei Kolmakov, *"Li Diffusion in All-Solid-State Batteries Imaged Through Optical and Electron Transparent Electrodes,"* Microscopy and Microanalysis 07/2016; 20(S3):1352–1353.

2. **Alexander Yulaev,** Alexey Lipatov, Alexander Sinitskii, and Andrei Kolmakov, *"Immobilization and Encapsulation of Micro- and Nano- Objects with Electron Transparent Graphene Oxide membranes,"* Microscopy and Microanalysis 08/2014; 20(S3):1798–1799.

3. Hongxuan Guo, **Alexander Yulaev,** Evgheni Strelcov, and Andrei Kolmakov, *"SEM and Auger Electron Spectroscopy of Liquid Water through Graphene Membrane,"* Microscopy and Microanalysis 23, 880, 2017.

4. E. Strelcov, H. Guo, **A. Yulaev,** J. Wang, N. Appathurai, S. Urquhart, J. Vinson, S. Subin, M. Zwolak, and A. Kolmakov, *"Combinatorial Microscopy in Liquids with Low Energy Electrons,"* Microscopy and Microanalysis 23, 186, 2017.

B.4 *Presentations related to this thesis*

(*denotes presenter)

1. **Alexander Yulaev*,** Vladimir Oleshko, Paul Haney, A. Alec Talin, Marina S. Leite, and Andrei Kolmakov, *"Probing Li-ion transport at carbon anode/solid electrolyte interfaces using* in-operando *SEM,"* SPIE Optics and Photonics - San Diego, CA, August, 6–10 2017 (poster presentation).

2. **Alexander Yulaev*,** Vladimir Oleshko, Paul Haney, A. Alec Talin, Marina S. Leite, and Andrei Kolmakov, *"Surface Oxidation Affects the Capacity of All-Solid-State Lithium-ion Battery,"* AVS Mid-Atlantic DC Regional Meeting Gaithersburg, MD, May 25, 2017 (poster presentation). **2^{nd} Place Poster Award**.

3. **Alexander Yulaev*,** Vladimir Oleshko, A. Alec Talin, Marina S. Leite, and Andrei Kolmakov, *"In Operando SEM of Plating in All-solid-state Lithium-ion Battery with Carbon Anodes,"* 2017 MRS Spring Meeting & Exhibit - Phoenix, AZ, April, 17–21, 2017 (oral presentation).

4. **Alexander Yulaev*,** Vladimir Oleshko, A. Alec Talin, Marina S. Leite, and Andrei Kolmakov, *"The Effect of Oxidation and Charge/Discharge rates on Li Plating in All-Solid-State Batteries,"* APS 2017 March Meeting New Orleans, LA, March, 12-17, 2017 (oral presentation).

5. Hongxuan Guo, Evgheni Strelcov*, **Alexander Yulaev,** Jian Wang, Narayana Appathurai, Stephen Urquhart, John Vinson, Subin Sahu, Michael P. Zwolak, and Andrei Kolmakov*, *"Real-time spectromicroscopy of the graphene-water interface using photoelectrons: first liquid PEEM results,"* APXPS-2016 - Oxford, UK, December 14, 2016 (oral presentation).

6. Hongxuan Guo*, **Alexander Yulaev,** and Andrei Kolmakov, *"Development of multi-channel graphene liquid cells based for in situ electron spectroscopy and microscopy,"* 2016 MRS Fall Meeting & Exhibit Boston, MA, November 27–December 2, 2016 (oral presentation).

7. **Alexander Yulaev*,** A. Alec Talin, Marina S. Leite, and Andrei Kolmakov, *"Probing Li-Ion Transport in All-Solid-State Batteries through Electron Transparent Electrodes,"* AVS 63nd International Symposium & Exhibition - Nashville, TN, November 6–11, 2016 (oral presentation). **Art Zone Contest finalist**.

8. Hongxuan Guo*, **Alexander Yulaev,** and Andrei Kolmakov, *"Wafer Scale Fabrication of the Suspended Graphene Membranes for In Situ Electron Microscopy and Spectroscopy in Liquids,"* AVS 63nd International Symposium & Exhibition - Nashville, TN, November 6–11, 2016 (poster presentation).

9. Hongxuan Guo*, **Alexander Yulaev,** and Andrei Kolmakov, *"Design and Performance of Large Surface Area Graphene Liquid Cell for in Situ Electron Spectroscopy and Microscopy,"* AVS 63nd International Symposium & Exhibition - Nashville, TN, November 6–11, 2016 (poster presentation).

10. Hongxuan Guo, Evgheni Strelcov*, **Alexander Yulaev,** Jian Wang, Narayana Appathurai, Stephen Urquhart, John Vinson, Subin Sahu, Michael P. Zwolak, and Andrei Kolmakov, *"PEEM in liquids: a new experimental approach and first tests,"* The 10th LEEM/PEEM - Monterey, CA, September 11–15, 2016 (oral presentation).

11. **Alexander Yulaev*,** A. Alec Talin, Marina S. Leite, and Andrei Kolmakov, *"Li Diffusion in All-Solid-State Batteries Imaged Through Optical and Electron Transparent Electrodes,"* Microscopy & Microanalysis 2016 Meeting Columbus, OH, July 24–28, 2016 (poster presentation).

12. **Alexander Yulaev*,** Guangjun Cheng, Angela R. Hight Walker, Ivan V. Vlassiouk, Alline Myers, Marina S. Leite, and Andrei Kolmakov, *"Graphene transfer using anthracene as a sacrificial layer,"* AVS Mid-Atlantic Chapter DC Regional Meeting at NIST - Gaithersburg, MD, May 26, 2016 (poster presentation). **Honorable Mention**.

13. **Alexander Yulaev*,** Guangjun Cheng, Angela R. Hight Walker, Ivan V. Vlassiouk, Alline Myers, Marina S. Leite, and Andrei Kolmakov, *"Dry Transfer of CVD Grown Graphene Using Anthracene as a Sacrificial Layer,"* NanoDay UMD College Park, MD, May 17–18, 2016 (poster presentation).

14. **Alexander Yulaev*,** Alec Talin, Marina S. Leite, and Andrei Kolmakov, *"Electron Transparent Electrodes for All-solid-state Batteries,"* Graduate Student Seminar, IREAP UMD, April 29, 2016 (oral presentation).

15. **Alexander Yulaev*,** *"Electron transparent membranes, coatings, and electrodes,"* CNST NIST All-Hands Meeting, June 9, 2016 (oral presentation).

16. **Alexander Yulaev*,** *"Electron transparent membranes and electrodes,"* ERG Meeting, NIST, March 30, 2016 (oral presentation).

17. **Alexander Yulaev*,** Guangjun Cheng, Angela Hight Walker, Marina Leite, Andrei Kolmakov, *"Facile Clean Transfer Method of CVD Grown Graphene Using Anthracene as a Sacrificial Layer,"* 2015 MRS Fall Meeting & Exhibit Boston, MA, November 29–December 4, 2015 (oral presentation).

18. **Alexander Yulaev*,** Guangjun Cheng, Angela Hight Walker, Marina Leite, Andrei Kolmakov, *"Obtaining Clean Suspended CVD Graphene: Comparative Examination of Few Transfer and Cleaning Protocols,"* AVS 62nd International Symposium & Exhibition - San Jose, CA, 18-23 October 2015 (oral presentation).

19. **Alexander Yulaev*,** Alexey Lipatov, Alexander Sinitskii, Marina S. Leite, Annie Xi Lu, and Andrei Kolmakov, *"Immobilization and Encapsulation of Micro- and Nano-Objects with Electron Transparent Graphene Oxide Membranes,"* IREAP UMD, October 2, 2015 (oral presentation).

20. **Alexander Yulaev*,** *"Poly-Aromatic Hydrocarbon Nanostructure Growth on Single and Multi-Layer Graphene,"* Graduate Student Seminar, IREAP UMD, February 20, 2015 (oral presentation).

21. **Alexander Yulaev*,** Guangjun Cheng, Angela Hight Walker, Marina S. Leite, Andrei Kolmakov, *"Comparative studies of the growth of model poly-aromatic hydrocarbon nanostructures on single and multilayer supported and suspended graphene,"* 2014 MRS Fall Meeting & Exhibit - Boston, MA, November 30–December 5, 2014 (poster presentation).

22. **Alexander Yulaev*,** and Andrei Kolmakov, *"Poly-aromatic hydrocarbon nanostructure growth on single and multi-layer graphene,"* AVS 61st International Symposium & Exhibition - Baltimore, MD, November 9-14, 2014 (oral presentation).

23. Christopher Brown*,**Alexander Yulaev,** and Andrei Kolmakov, *"Microfluidic Cell for In Situ Scanning Electron Microscopy of Hydrated Dynamic Systems,"* AVS 61st International Symposium & Exhibition - Baltimore, MD, November 9-14, 2014 (poster presentation).

24. **Alexander Yulaev*,** and Andrei Kolmakov, *"Immobilization and Encapsulation of Micro- and Nano- Objects with Electron Transparent Graphene Oxide membranes,"* M&M meeting 2014 - Hartford, CT, August 3–7, 2014 (poster presentation).

25. **Alexander Yulaev*,** and Andrei Kolmakov, *"Multichannel sample platform for ambient pressure XPS and electron microscopy,"* NanoDay UMD College Park, MD, June 11, 2014 (poster presentation).

26. **Alexander Yulaev*,** and Andrei Kolmakov, *"Multichannel sample platform for ambient pressure XPS and electron microscopy,"* AVS Mid-Atlantic Chapter DC Regional Meeting at NIST - Gaithersburg, MD, May 15, 2014 (poster presentation).

27. **Alexander Yulaev*,** and Andrei Kolmakov, *"Encapsulation and Electron Microscopy of Microscopic Objects Using Graphene Oxide Membranes,"* 2013 MRS Fall Meeting & Exhibit Boston, MA, December 1–6, 2013 (poster presentation).

Bibliography

[1] F. M. Ross, *Liquid Cell Electron Microscopy*. Cambridge University Press, 2016.

[2] V. E. Ruska, "Beitrag zur übermikroskopischen abbildung bei höheren drucken," *Colloid & Polymer Science*, vol. 100, no. 2, pp. 212–219, 1942.

[3] S. Helveg, C. López-Cartes, J. Sehested, P. L. Hansen, B. S. Clausen, J. R. Rostrup-Nielsen, F. Abild-Pedersen, and J. K. Nørskov, "Atomic-scale imaging of carbon nanofibre growth," *Nature*, vol. 427, no. 6973, pp. 426–429, 2004.

[4] H. Bluhm, D. F. Ogletree, C. S. Fadley, Z. Hussain, and M. Salmeron, "The premelting of ice studied with photoelectron spectroscopy," *Journal of Physics: Condensed Matter*, vol. 14, no. 8, p. L227, 2002.

[5] G. Ketteler, S. Yamamoto, H. Bluhm, K. Andersson, D. E. Starr, D. F. Ogletree, H. Ogasawara, A. Nilsson, and M. Salmeron, "The nature of water nucleation sites on TiO_2 (110) surfaces revealed by ambient pressure X-ray photoelectron spectroscopy," *The Journal of Physical Chemistry C*, vol. 111, no. 23, pp. 8278–8282, 2007.

[6] A. Verdaguer, C. Weis, G. Oncins, G. Ketteler, H. Bluhm, and M. Salmeron, "Growth and structure of water on SiO_2 films on Si investigated by kelvin probe microscopy and *in situ* X-ray spectroscopies," *Langmuir*, vol. 23, no. 19, pp. 9699–9703, 2007.

[7] E. Lundgren, J. Gustafson, A. Mikkelsen, J. N. Andersen, A. Stierle, H. Dosch, M. Todorova, J. Rogal, K. Reuter, and M. Scheffler, "Kinetic hindrance during the initial oxidation of Pd (100) at ambient pressures," *Physical review letters*, vol. 92, no. 4, p. 046101, 2004.

[8] G. Ketteler, D. F. Ogletree, H. Bluhm, H. Liu, E. L. Hebenstreit, and M. Salmeron, "*In situ* spectroscopic study of the oxidation and reduction of Pd (111)," *Journal of the American Chemical Society*, vol. 127, no. 51, pp. 18269–18273, 2005.

[9] M. Todorova, W. Li, M. V. Ganduglia-Pirovano, C. Stampfl, K. Reuter, and M. Scheffler, "Role of subsurface oxygen in oxide formation at transition metal surfaces," *Physical review letters*, vol. 89, no. 9, p. 096103, 2002.

[10] M. Salmeron and R. Schlögl, "Ambient pressure photoelectron spectroscopy: A new tool for surface science and nanotechnology," *Surface Science Reports*, vol. 63, no. 4, pp. 169–199, 2008.

[11] C. Spiel, D. Vogel, Y. Suchorski, W. Drachsel, R. Schlögl, and G. Rupprechter, "Catalytic co oxidation on individual (110) domains of a polycrystalline Pt foil: local reaction kinetics by PEEM," *Catalysis Letters*, vol. 141, no. 5, pp. 625–632, 2011.

[12] L. Q. Zhang, X. H. Liu, Y. Liu, S. Huang, T. Zhu, L. Gui, S. X. Mao, Z. Z. Ye, C. M. Wang, J. P. Sullivan, *et al.*, "Controlling the lithiation-induced strain and charging rate in nanowire electrodes by coating," *ACS Nano*, vol. 5, no. 6, pp. 4800–4809, 2011.

[13] C.-M. Wang, "*In situ* transmission electron microscopy and spectroscopy studies of rechargeable batteries under dynamic operating conditions: A retrospective and perspective view," *Journal of Materials Research*, vol. 30, no. 3, pp. 326–339, 2015.

[14] M. Gu, A. Kushima, Y. Shao, J.-G. Zhang, J. Liu, N. D. Browning, J. Li, and C. Wang, "Probing the failure mechanism of SnO_2 nanowires for sodium-ion batteries," *Nano letters*, vol. 13, no. 11, pp. 5203–5211, 2013.

[15] H. Bluhm, M. Hävecker, A. Knop-Gericke, M. Kiskinova, R. Schloegl, and M. Salmeron, "*In situ* X-ray photoelectron spectroscopy studies of gas-solid interfaces at near-ambient conditions," *MRS bulletin*, vol. 32, no. 12, pp. 1022–1030, 2007.

[16] S. Tanuma, C. Powell, and D. Penn, "Calculations of electron inelastic mean free paths. ix. data for 41 elemental solids over the 50 eV to 30 keV range," *Surface and Interface Analysis*, vol. 43, no. 3, pp. 689–713, 2011.

[17] P. Cumpson and M. Seah, "Elastic scattering corrections in AES and XPS. ii. estimating attenuation lengths and conditions required for their valid use in overlayer/substrate experiments," *Surface and Interface Analysis*, vol. 25, no. 6, pp. 430–446, 1997.

[18] D. R. Penn, "Electron mean-free-path calculations using a model dielectric function," *Physical Review B*, vol. 35, no. 2, p. 482, 1987.

[19] K. Kanaya and S. Okayama, "Penetration and energy-loss theory of electrons in solid targets," *Journal of Physics D: Applied Physics*, vol. 5, no. 1, p. 43, 1972.

[20] J. I. Goldstein, "Scanning electron microscopy and X-ray microanalysis," 1979.

[21] L. Marton, "La microscopie electronique des objets biologiques," *Bull. Acad. Roy. Med. Belg*, vol. 21, pp. 600–617, 1935.

[22] I. Abrams and J. McBain, "A closed cell for electron microscopy," *Journal of Applied Physics*, vol. 15, no. 8, pp. 607–609, 1944.

[23] T. L. Daulton, B. J. Little, K. Lowe, and J. Jones-Meehan, "*In situ* environmental cell–transmission electron microscopy study of microbial reduction of chromium (vi) using electron energy loss spectroscopy," *Microscopy and Microanalysis*, vol. 7, no. 06, pp. 470–485, 2001.

[24] K. Nishijima, J. Yamasaki, H. Orihara, and N. Tanaka, "Development of microcapsules for electron microscopy and their application to dynamical observation of liquid crystals in transmission electron microscopy," *Nanotechnology*, vol. 15, no. 6, p. S329, 2004.

[25] M. Williamson, R. Tromp, P. Vereecken, R. Hull, and F. Ross, "Dynamic microscopy of nanoscale cluster growth at the solid–liquid interface," *Nature materials*, vol. 2, no. 8, pp. 532–536, 2003.

[26] N. De Jonge, D. B. Peckys, G. Kremers, and D. Piston, "Electron microscopy of whole cells in liquid with nanometer resolution," *Proceedings of the National Academy of Sciences*, vol. 106, no. 7, pp. 2159–2164, 2009.

[27] J. M. Grogan and H. H. Bau, "The nanoaquarium: a platform for in situ transmission electron microscopy in liquid media," *Journal of Microelectromechanical Systems*, vol. 19, no. 4, pp. 885–894, 2010.

[28] R. Franks, S. Morefield, J. Wen, D. Liao, J. Alvarado, M. Strano, and C. Marsh, "A study of nanomaterial dispersion in solution by wet-cell transmission electron microscopy," *Journal of nanoscience and nanotechnology*, vol. 8, no. 9, pp. 4404–4407, 2008.

[29] K.-L. Liu, C.-C. Wu, Y.-J. Huang, H.-L. Peng, H.-Y. Chang, P. Chang, L. Hsu, and T.-R. Yew, "Novel microchip for *in situ* TEM imaging of living organisms and bio-reactions in aqueous conditions," *Lab on a Chip*, vol. 8, no. 11, pp. 1915–1921, 2008.

[30] E. A. Ring and N. De Jonge, "Microfluidic system for transmission electron microscopy," *Microscopy and Microanalysis*, vol. 16, no. 05, pp. 622–629, 2010.

[31] N. de Jonge, N. Poirier-Demers, H. Demers, D. B. Peckys, and D. Drouin, "Nanometer-resolution electron microscopy through micrometers-thick water layers," *Ultramicroscopy*, vol. 110, no. 9, pp. 1114–1119, 2010.

[32] P. L. Gai and J. J. Calvino, "Electron microscopy in the catalysis of alkane oxidation, environmental control, and alternative energy sources," *Annu. Rev. Mater. Res.*, vol. 35, pp. 465–504, 2005.

[33] S. Thiberge, O. Zik, and E. Moses, "An apparatus for imaging liquids, cells, and other wet samples in the scanning electron microscopy," *Review of scientific instruments*, vol. 75, no. 7, pp. 2280–2289, 2004.

[34] A. Hitchcock, C. Morin, Y. Heng, R. Cornelius, and J. Brash, "Towards practical soft X-ray spectromicroscopy of biomaterials," *Journal of Biomaterials Science, Polymer Edition*, vol. 13, no. 8, pp. 919–937, 2002.

[35] T. H. Yoon, "Applications of soft X-ray spectromicroscopy in material and environmental sciences," *Applied Spectroscopy Reviews*, vol. 44, no. 2, pp. 91–122, 2009.

[36] V. Ballarotto, M. Breban, K. Siegrist, R. Phaneuf, and E. Williams, "Photoelectron emission microscopy of ultrathin oxide covered devices," *Journal of Vacuum Science & Technology B: Microelectronics and Nanometer Structures Processing, Measurement, and Phenomena*, vol. 20, no. 6, pp. 2514–2518, 2002.

[37] B. Frazer, B. Gilbert, and G. De Stasio, "X-ray absorption microscopy of aqueous samples," *Review of scientific instruments*, vol. 73, no. 3, pp. 1373–1375, 2002.

[38] X. Li, C. W. Magnuson, A. Venugopal, R. M. Tromp, J. B. Hannon, E. M. Vogel, L. Colombo, and R. S. Ruoff, "Large-area graphene single crystals grown by low-pressure chemical vapor deposition of methane on copper," *Journal of the American Chemical Society*, vol. 133, no. 9, pp. 2816–2819, 2011.

[39] A. Reina, X. Jia, J. Ho, D. Nezich, H. Son, V. Bulovic, M. S. Dresselhaus, and J. Kong, "Large area, few-layer graphene films on arbitrary substrates by chemical vapor deposition," *Nano letters*, vol. 9, no. 1, pp. 30–35, 2008.

[40] X. Li, W. Cai, J. An, S. Kim, J. Nah, D. Yang, R. Piner, A. Velamakanni, I. Jung, E. Tutuc, *et al.*, "Large-area synthesis of high-quality and uniform graphene films on copper foils," *Science*, vol. 324, no. 5932, pp. 1312–1314, 2009.

[41] K. S. Kim, Y. Zhao, H. Jang, S. Y. Lee, J. M. Kim, K. S. Kim, J.-H. Ahn, P. Kim, J.-Y. Choi, and B. H. Hong, "Large-scale pattern growth of graphene films for stretchable transparent electrodes," *Nature*, vol. 457, no. 7230, pp. 706–710, 2009.

[42] S. Bae, H. Kim, Y. Lee, X. Xu, J.-S. Park, Y. Zheng, J. Balakrishnan, T. Lei, H. R. Kim, Y. I. Song, *et al.*, "Roll-to-roll production of 30-inch graphene films for transparent electrodes," *Nature nanotechnology*, vol. 5, no. 8, pp. 574–578, 2010.

[43] S. Stankovich, D. A. Dikin, G. H. Dommett, K. M. Kohlhaas, E. J. Zimney, E. A. Stach, R. D. Piner, S. T. Nguyen, and R. S. Ruoff, "Graphene-based composite materials," *Nature*, vol. 442, no. 7100, pp. 282–286, 2006.

[44] R. Nair, H. Wu, P. Jayaram, I. Grigorieva, and A. Geim, "Unimpeded permeation of water through helium-leak–tight graphene-based membranes," *Science*, vol. 335, no. 6067, pp. 442–444, 2012.

[45] W. S. Hummers Jr and R. E. Offeman, "Preparation of graphitic oxide," *Journal of the American Chemical Society*, vol. 80, no. 6, pp. 1339–1339, 1958.

[46] B. Alemán, W. Regan, S. Aloni, V. Altoe, N. Alem, C. Girit, B. Geng, L. Maserati, M. Crommie, F. Wang, *et al.*, "Transfer-free batch fabrication of large-area suspended graphene membranes," *ACS Nano*, vol. 4, no. 8, pp. 4762–4768, 2010.

[47] X. Liang, B. A. Sperling, I. Calizo, G. Cheng, C. A. Hacker, Q. Zhang, Y. Obeng, K. Yan, H. Peng, Q. Li, *et al.*, "Toward clean and crackless transfer of graphene," *ACS Nano*, vol. 5, no. 11, pp. 9144–9153, 2011.

[48] W. Regan, N. Alem, B. Alemán, B. Geng, Ç. Girit, L. Maserati, F. Wang, M. Crommie, and A. Zettl, "A direct transfer of layer-area graphene," *Applied Physics Letters*, vol. 96, no. 11, p. 113102, 2010.

[49] J. Kraus, R. Reichelt, S. Günther, L. Gregoratti, M. Amati, M. Kiskinova, A. Yulaev, I. Vlassiouk, and A. Kolmakov, "Photoelectron spectroscopy of wet and gaseous samples through graphene membranes," *Nanoscale*, vol. 6, no. 23, pp. 14394–14403, 2014.

[50] C. Lee, X. Wei, J. W. Kysar, and J. Hone, "Measurement of the elastic properties and intrinsic strength of monolayer graphene," *Science*, vol. 321, no. 5887, pp. 385–388, 2008.

[51] T. J. Booth, P. Blake, R. R. Nair, D. Jiang, E. W. Hill, U. Bangert, A. Bleloch, M. Gass, K. S. Novoselov, M. I. Katsnelson, *et al.*, "Macroscopic graphene membranes and their extraordinary stiffness," *Nano letters*, vol. 8, no. 8, pp. 2442–2446, 2008.

[52] J. C. Meyer, A. K. Geim, M. I. Katsnelson, K. S. Novoselov, T. J. Booth, and S. Roth, "The structure of suspended graphene sheets," *Nature*, vol. 446, no. 7131, pp. 60–63, 2007.

[53] J. C. Meyer, C. O. Girit, M. Crommie, and A. Zettl, "Imaging and dynamics of light atoms and molecules on graphene," *Nature*, vol. 454, no. 7202, pp. 319–322, 2008.

[54] I. Müllerová, M. Hovorka, R. Hanzlíková, and L. Frank, "Very low energy scanning electron microscopy of free-standing ultrathin films," *Materials transactions*, vol. 51, no. 2, pp. 265–270, 2010.

[55] K. R. Knox, S. Wang, A. Morgante, D. Cvetko, A. Locatelli, T. O. Mentes, M. A. Niño, P. Kim, and R. Osgood Jr, "Spectromicroscopy of single and multilayer graphene supported by a weakly interacting substrate," *Physical Review B*, vol. 78, no. 20, p. 201408, 2008.

[56] J. S. Bunch, S. S. Verbridge, J. S. Alden, A. M. Van Der Zande, J. M. Parpia, H. G. Craighead, and P. L. McEuen, "Impermeable atomic membranes from graphene sheets," *Nano letters*, vol. 8, no. 8, pp. 2458–2462, 2008.

[57] E. Stolyarova, D. Stolyarov, K. Bolotin, S. Ryu, L. Liu, K. Rim, M. Klima, M. Hybertsen, I. Pogorelsky, I. Pavlishin, *et al.*, "Observation of graphene bubbles and effective mass transport under graphene films," *Nano letters*, vol. 9, no. 1, pp. 332–337, 2008.

[58] K. Xu, P. Cao, and J. R. Heath, "Graphene visualizes the first water adlayers on mica at ambient conditions," *Science*, vol. 329, no. 5996, pp. 1188–1191, 2010.

[59] M. Krueger, S. Berg, D. Stone, E. Strelcov, D. A. Dikin, J. Kim, L. J. Cote, J. Huang, and A. Kolmakov, "Drop-casted self-assembling graphene oxide membranes for scanning electron microscopy on wet and dense gaseous samples," *ACS Nano*, vol. 5, no. 12, pp. 10047–10054, 2011.

[60] A. Kolmakov, D. A. Dikin, L. J. Cote, J. Huang, M. K. Abyaneh, M. Amati, L. Gregoratti, S. Günther, and M. Kiskinova, "Graphene oxide windows for *in situ* environmental cell photoelectron spectroscopy," *Nature nanotechnology*, vol. 6, no. 10, pp. 651–657, 2011.

[61] J. M. Yuk, J. Park, P. Ercius, K. Kim, D. J. Hellebusch, M. F. Crommie, J. Y. Lee, A. Zettl, and A. P. Alivisatos, "High-resolution EM of colloidal nanocrystal growth using graphene liquid cells," *Science*, vol. 336, no. 6077, pp. 61–64, 2012.

[62] G. Zamborlini, M. Imam, L. L. Patera, T. O. Mentes, N. Stojic, C. Africh, A. Sala, N. Binggeli, G. Comelli, and A. Locatelli, "Nanobubbles at GPa pressure under graphene," *Nano letters*, vol. 15, no. 9, pp. 6162–6169, 2015.

[63] A. Kolmakov, L. Gregoratti, M. Kiskinova, and S. Günther, "Recent approaches for bridging the pressure gap in photoelectron microspectroscopy," *Topics in Catalysis*, vol. 59, no. 5-7, pp. 448–468, 2016.

[64] J.-S. Kim, Y. Liu, W. Zhu, S. Kim, D. Wu, L. Tao, A. Dodabalapur, K. Lai, and D. Akinwande, "Toward air-stable multilayer phosphorene thin-films and transistors," *Scientific reports*, vol. 5, 2015.

[65] Y. Yang, X. Li, M. Wen, E. Hacopian, W. Chen, Y. Gong, J. Zhang, B. Li, W. Zhou, P. M. Ajayan, *et al.*, "Brittle fracture of 2D $MoSe_2$," *Advanced Materials*, vol. 29, no. 2, 2017.

[66] A. Sali, R. Glaeser, T. Earnest, and W. Baumeister, "From words to literature in structural proteomics," *Nature*, vol. 422, no. 6928, pp. 216–225, 2003.

[67] N. de Jonge and F. M. Ross, "Electron microscopy of specimens in liquid," *Nature nanotechnology*, vol. 6, no. 11, pp. 695–704, 2011.

[68] S. Thiberge, A. Nechushtan, D. Sprinzak, O. Gileadi, V. Behar, O. Zik, Y. Chowers, S. Michaeli, J. Schlessinger, and E. Moses, "Scanning electron microscopy of cells and tissues under fully hydrated conditions," *Proceedings of the National Academy of Sciences of the United States of America*, vol. 101, no. 10, pp. 3346–3351, 2004.

[69] H. Sugi, T. Akimoto, K. Sutoh, S. Chaen, N. Oishi, and S. Suzuki, "Dynamic electron microscopy of ATP-induced myosin head movement in living muscle thick filaments," *Proceedings of the National Academy of Sciences*, vol. 94, no. 9, pp. 4378–4382, 1997.

[70] D. B. Peckys, U. Korf, and N. de Jonge, "Local variations of HER2 dimerization in breast cancer cells discovered by correlative fluorescence and liquid electron microscopy," *Science advances*, vol. 1, no. 6, p. e1500165, 2015.

[71] H. Zheng, R. K. Smith, Y.-w. Jun, C. Kisielowski, U. Dahmen, and A. P. Alivisatos, "Observation of single colloidal platinum nanocrystal growth trajectories," *Science*, vol. 324, no. 5932, pp. 1309–1312, 2009.

[72] F. Ross, "Electrochemical nucleation, growth and dendrite formation in liquid cell TEM," *Microscopy and Microanalysis*, vol. 16, no. S2, pp. 326–327, 2010.

[73] H. Nishiyama, M. Suga, T. Ogura, Y. Maruyama, M. Koizumi, K. Mio, S. Kitamura, and C. Sato, "Reprint of: Atmospheric scanning electron microscope observes cells and tissues in open medium through silicon nitride film," *Journal of structural biology*, vol. 172, no. 2, pp. 191–202, 2010.

[74] A. Radisic, F. Ross, and P. Searson, "*In situ* study of the growth kinetics of individual island electrodeposition of copper," *The Journal of Physical Chemistry B*, vol. 110, no. 15, pp. 7862–7868, 2006.

[75] A. Radisic, P. Vereecken, P. Searson, and F. Ross, "The morphology and nucleation kinetics of copper islands during electrodeposition," *Surface science*, vol. 600, no. 9, pp. 1817–1826, 2006.

[76] A. Radisic, P. M. Vereecken, J. B. Hannon, P. C. Searson, and F. M. Ross, "Quantifying electrochemical nucleation and growth of nanoscale clusters using real-time kinetic data," *Nano Letters*, vol. 6, no. 2, pp. 238–242, 2006.

[77] E. R. White, S. B. Singer, V. Augustyn, W. A. Hubbard, M. Mecklenburg, B. Dunn, and B. C. Regan, "*In situ* transmission electron microscopy of lead dendrites and lead ions in aqueous solution," *ACS Nano*, vol. 6, no. 7, pp. 6308–6317, 2012.

[78] M. Sun, H.-G. Liao, K. Niu, and H. Zheng, "Structural and morphological evolution of lead dendrites during electrochemical migration," *Scientific reports*, vol. 3, 2013.

[79] Z. Zeng, W.-I. Liang, H.-G. Liao, H. L. Xin, Y.-H. Chu, and H. Zheng, "Visualization of electrode–electrolyte interfaces in $LiPF_6$/EC/DEC electrolyte for lithium ion batteries *via in situ* tem," *Nano letters*, vol. 14, no. 4, pp. 1745–1750, 2014.

[80] B. L. Mehdi, J. Qian, E. Nasybulin, C. Park, D. A. Welch, R. Faller, H. Mehta, W. A. Henderson, W. Xu, C. M. Wang, *et al.*, "Observation and quantification of nanoscale processes in lithium batteries by operando electrochemical (S)TEM," *Nano letters*, vol. 15, no. 3, pp. 2168–2173, 2015.

[81] R. L. Sacci, J. M. Black, N. Balke, N. J. Dudney, K. L. More, and R. R. Unocic, "Nanoscale imaging of fundamental Li battery chemistry: solid-electrolyte interphase formation and preferential growth of lithium metal nanoclusters," *Nano letters*, vol. 15, no. 3, pp. 2011–2018, 2015.

[82] A. J. Leenheer, K. L. Jungjohann, K. R. Zavadil, J. P. Sullivan, and C. T. Harris, "Lithium electrodeposition dynamics in aprotic electrolyte observed *in situ via* transmission electron microscopy," *ACS Nano*, vol. 9, no. 4, pp. 4379–4389, 2015.

[83] A. Jansson, C. Boissier, M. Marucci, M. Nicholas, S. Gustafsson, A.-M. Hermansson, and E. Olsson, "Novel method for visualizing water transport through phase-separated polymer films," *Microscopy and Microanalysis*, vol. 20, no. 2, pp. 394–406, 2014.

[84] A. Jansson, A. Nafari, A. Sanz-Velasco, K. Svensson, S. Gustafsson, A.-M. Hermansson, and E. Olsson, "Novel method for controlled wetting of materials in the environmental scanning electron microscope," *Microscopy and Microanalysis*, vol. 19, no. 1, pp. 30–37, 2013.

[85] D. Mattia and Y. Gogotsi, "Static and dynamic behavior of liquids inside carbon nanotubes," *Microfluidics and Nanofluidics*, vol. 5, no. 3, pp. 289–305, 2008.

[86] H. Gabrisch, L. Kjeldgaard, E. Johnson, and U. Dahmen, "Equilibrium shape and interface roughening of small liquid Pb inclusions in solid Al," *Acta materialia*, vol. 49, no. 20, pp. 4259–4269, 2001.

[87] F. Ross, J. Tersoff, and M. Reuter, "Sawtooth faceting in silicon nanowires," *Physical review letters*, vol. 95, no. 14, p. 146104, 2005.

[88] X. Zhong, M. Burke, S. Schilling, S. Haigh, N. Zaluzec, *et al.*, "Novel hybrid sample preparation method for *in situ* liquid cell TEM analysis," *Microscopy and Microanalysis*, vol. 20, p. 1514, 2014.

[89] S. W. Chee, S. H. Pratt, K. Hattar, D. Duquette, F. M. Ross, and R. Hull, "Studying localized corrosion using liquid cell transmission electron microscopy," *Chemical Communications*, vol. 51, no. 1, pp. 168–171, 2015.

[90] S. W. Chee, D. J. Duquette, F. M. Ross, and R. Hull, "Metastable structures in Al thin films before the onset of corrosion pitting as observed using liquid cell transmission electron microscopy," *Microscopy and Microanalysis*, vol. 20, no. 2, pp. 462–468, 2014.

[91] S. K. Eswaramoorthy, J. M. Howe, and G. Muralidharan, "*In situ* determination of the nanoscale chemistry and behavior of solid-liquid systems," *Science*, vol. 318, no. 5855, pp. 1437–1440, 2007.

[92] J.-G. Lee and H. Mori, "*In-situ* observation of alloy phase formation in nanometre-sized particles in the Sn–Bi system," *Philosophical Magazine*, vol. 84, no. 25-26, pp. 2675–2686, 2004.

[93] J. M. Howe and H. Saka, "*In situ* transmission electron microscopy studies of the solid–liquid interface," *MRS bulletin*, vol. 29, no. 12, pp. 951–957, 2004.

[94] J. Bates, N. Dudney, B. Neudecker, A. Ueda, and C. Evans, "Thin-film lithium and lithium-ion batteries," *Solid State Ionics*, vol. 135, no. 1, pp. 33–45, 2000.

[95] R. Huggins, *Advanced batteries: materials science aspects*. Springer Science & Business Media, 2008.

[96] J. Bates, N. Dudney, G. Gruzalski, R. Zuhr, A. Choudhury, C. Luck, and J. Robertson, "Fabrication and characterization of amorphous lithium electrolyte thin films and rechargeable thin-film batteries," *Journal of power sources*, vol. 43, no. 1-3, pp. 103–110, 1993.

[97] N. Balke, S. Jesse, Y. Kim, L. Adamczyk, A. Tselev, I. N. Ivanov, N. J. Dudney, and S. V. Kalinin, "Real space mapping of Li-ion transport in amorphous Si anodes with nanometer resolution," *Nano letters*, vol. 10, no. 9, pp. 3420–3425, 2010.

[98] M. S. Leite, D. Ruzmetov, Z. Li, L. A. Bendersky, N. C. Bartelt, A. Kolmakov, and A. A. Talin, "Insights into capacity loss mechanisms of all-solid-state Li-ion batteries with Al anodes," *Journal of Materials Chemistry A*, vol. 2, no. 48, pp. 20552–20559, 2014.

[99] C. Gong, D. Ruzmetov, A. Pearse, D. Ma, J. N. Munday, G. Rubloff, A. A. Talin, and M. S. Leite, "Surface/interface effects on high-performance thin-film all-solid-state Li-ion batteries," *ACS applied materials & interfaces*, vol. 7, no. 47, pp. 26007–26011, 2015.

[100] D. Ruzmetov, V. P. Oleshko, P. M. Haney, H. J. Lezec, K. Karki, K. H. Baloch, A. K. Agrawal, A. V. Davydov, S. Krylyuk, Y. Liu, *et al.*, "Electrolyte stability determines scaling limits for solid-state 3D Li ion batteries," *Nano letters*, vol. 12, no. 1, pp. 505–511, 2011.

[101] M. Motoyama, M. Ejiri, and Y. Iriyama, "*In-Situ* electron microscope observations of electrochemical Li deposition/dissolution with a LiPON electrolyte," *Electrochemistry*, vol. 82, no. 5, pp. 364–368, 2014.

[102] M. Motoyama, M. Ejiri, and Y. Iriyama, "Modeling the nucleation and growth of Li at metal current collector/LiPON interfaces," *Journal of The Electrochemical Society*, vol. 162, no. 13, pp. A7067–A7071, 2015.

[103] A. Yulaev, A. Lipatov, A. X. Lu, A. Sinitskii, M. S. Leite, and A. Kolmakov, "Imaging and analysis of encapsulated objects through self-assembled electron and optically transparent graphene oxide membranes," *Advanced Materials Interfaces*, 2016.

[104] A. Yulaev, A. Lipatov, A. Sinitskii, and A. Kolmakov, "Immobilization and encapsulation of micro-and nano-objects with electron transparent graphene oxide membranes," *Microscopy and Microanalysis*, vol. 20, no. S3, pp. 1798–1799, 2014.

[105] J. W. Suk, A. Kitt, C. W. Magnuson, Y. Hao, S. Ahmed, J. An, A. K. Swan, B. B. Goldberg, and R. S. Ruoff, "Transfer of CVD-grown monolayer graphene onto arbitrary substrates," *ACS Nano*, vol. 5, no. 9, pp. 6916–6924, 2011.

[106] Y.-C. Lin, C.-C. Lu, C.-H. Yeh, C. Jin, K. Suenaga, and P.-W. Chiu, "Graphene annealing: how clean can it be?," *Nano letters*, vol. 12, no. 1, pp. 414–419, 2011.

[107] A. Yulaev, G. Cheng, A. R. H. Walker, I. V. Vlassiouk, A. Myers, M. S. Leite, and A. Kolmakov, "Toward clean suspended cvd graphene," *RSC Advances*, vol. 6, no. 87, pp. 83954–83962, 2016.

[108] A. Yulaev, H. Guo, E. Strelcov, L. Chen, I. Vlassiouk, and A. Kolmakov, "Graphene microcapsule arrays for combinatorial electron microscopy and spectroscopy in liquids," *ACS Applied Materials & Interfaces*, 2017.

[109] H. Guo, E. Strelcov, A. Yulaev, J. Wang, N. Appathurai, S. Urquhart, J. Vinson, S. Sahu, M. Zwolak, and A. Kolmakov, "Enabling photoemission electron microscopy in liquids *via* graphene-capped microchannel arrays," *Nano letters*, vol. 17, no. 2, pp. 1034–1041, 2017.

[110] A. G. Aberle, "Surface passivation of crystalline silicon solar cells: a review," *Progress in Photovoltaics: Research and Applications*, vol. 8, no. 5, pp. 473–487, 2000.

[111] P. M. Wilson, A. Zobel, A. Lipatov, E. Schubert, T. Hofmann, and A. Sinitskii, "Multilayer graphitic coatings for thermal stabilization of metallic nanostructures," *ACS applied materials & interfaces*, vol. 7, no. 5, pp. 2987–2992, 2015.

[112] R. H. MuÈller, K. MaÈder, and S. Gohla, "Solid lipid nanoparticles (SLN) for controlled drug delivery–a review of the state of the art," *European journal of pharmaceutics and biopharmaceutics*, vol. 50, no. 1, pp. 161–177, 2000.

[113] B. Sobrino, M. Brión, and A. Carracedo, "SNPs in forensic genetics: a review on SNP typing methodologies," *Forensic science international*, vol. 154, no. 2, pp. 181–194, 2005.

[114] B. Herrmann and S. Hummel, *Ancient DNA: recovery and analysis of genetic material from paleontological, archaeological, museum, medical, and forensic specimens*. Springer Science & Business Media, 2012.

[115] M. T. Gonzalez-Arnao and F. Engelmann, "Cryopreservation of plant germplasm using the encapsulation-dehydration technique: review and case study on sugarcane," *CryoLetters*, vol. 27, no. 3, pp. 155–168, 2006.

[116] J. J. Bozzola and L. D. Russell, *Electron microscopy: principles and techniques for biologists*. Jones & Bartlett Learning, 1999.

[117] C. Grupen, *Introduction to radiation protection: practical knowledge for handling radioactive sources*. Springer Science & Business Media, 2010.

[118] A. Y. Romanchuk, A. S. Slesarev, S. N. Kalmykov, D. V. Kosynkin, and J. M. Tour, "Graphene oxide for effective radionuclide removal," *Physical Chemistry Chemical Physics*, vol. 15, no. 7, pp. 2321–2327, 2013.

[119] J. L. Wierman, J. S. Alden, C. U. Kim, P. L. McEuen, and S. M. Gruner, "Graphene as a protein crystal mounting material to reduce background scatter," *Journal of applied crystallography*, vol. 46, no. 5, pp. 1501–1507, 2013.

[120] Y. Zhu, S. Murali, W. Cai, X. Li, J. W. Suk, J. R. Potts, and R. S. Ruoff, "Graphene and graphene oxide: synthesis, properties, and applications," *Advanced materials*, vol. 22, no. 35, pp. 3906–3924, 2010.

[121] D. Li, M. B. Müller, S. Gilje, R. B. Kaner, and G. G. Wallace, "Processable aqueous dispersions of graphene nanosheets," *Nature nanotechnology*, vol. 3, no. 2, pp. 101–105, 2008.

[122] N. R. Wilson, P. A. Pandey, R. Beanland, R. J. Young, I. A. Kinloch, L. Gong, Z. Liu, K. Suenaga, J. P. Rourke, S. J. York, *et al.*, "Graphene oxide: structural analysis and application as a highly transparent support for electron microscopy," *ACS Nano*, vol. 3, no. 9, pp. 2547–2556, 2009.

[123] D. A. Dikin, S. Stankovich, E. J. Zimney, R. D. Piner, G. H. Dommett, G. Evmenenko, S. T. Nguyen, and R. S. Ruoff, "Preparation and characterization of graphene oxide paper," *Nature*, vol. 448, no. 7152, pp. 457–460, 2007.

[124] N. Kovtyukhova, E. Buzaneva, A. Gorchinsky, P. Ollivier, B. Martin, C. Waraksa, and T. Mallouk, "Self-assembly of nanoblocks and molecules in optical thin-film nanostructures," in *Frontiers of Nano-Optoelectronic Systems*, pp. 331–346, Springer, 2000.

[125] J. Kim, L. J. Cote, F. Kim, W. Yuan, K. R. Shull, and J. Huang, "Graphene oxide sheets at interfaces," *Journal of the American Chemical Society*, vol. 132, no. 23, pp. 8180–8186, 2010.

[126] C. Chen, Q.-H. Yang, Y. Yang, W. Lv, Y. Wen, P.-X. Hou, M. Wang, and H.-M. Cheng, "Self-assembled free-standing graphite oxide membrane," *Advanced Materials*, vol. 21, no. 29, pp. 3007–3011, 2009.

[127] K. Erickson, R. Erni, Z. Lee, N. Alem, W. Gannett, and A. Zettl, "Determination of the local chemical structure of graphene oxide and reduced graphene oxide," *Advanced Materials*, vol. 22, no. 40, pp. 4467–4472, 2010.

[128] W. Lv, Z. Xia, S. Wu, Y. Tao, F.-M. Jin, B. Li, H. Du, Z.-P. Zhu, Q.-H. Yang, and F. Kang, "Conductive graphene-based macroscopic membrane self-assembled at a liquid–air interface," *Journal of Materials Chemistry*, vol. 21, no. 10, pp. 3359–3364, 2011.

[129] B. Dan, N. Behabtu, A. Martinez, J. S. Evans, D. V. Kosynkin, J. M. Tour, M. Pasquali, and I. I. Smalyukh, "Liquid crystals of aqueous, giant graphene oxide flakes," *Soft Matter*, vol. 7, no. 23, pp. 11154–11159, 2011.

[130] J. E. Kim, T. H. Han, S. H. Lee, J. Y. Kim, C. W. Ahn, J. M. Yun, and S. O. Kim, "Graphene oxide liquid crystals," *Angewandte Chemie International Edition*, vol. 50, no. 13, pp. 3043–3047, 2011.

[131] Z. Xu and C. Gao, "Aqueous liquid crystals of graphene oxide," *ACS Nano*, vol. 5, no. 4, pp. 2908–2915, 2011.

[132] F. Guo, F. Kim, T. H. Han, V. B. Shenoy, J. Huang, and R. H. Hurt, "Hydration-responsive folding and unfolding in graphene oxide liquid crystal phases," *ACS Nano*, vol. 5, no. 10, pp. 8019–8025, 2011.

[133] R. Joshi, P. Carbone, F.-C. Wang, V. G. Kravets, Y. Su, I. V. Grigorieva, H. Wu, A. K. Geim, and R. R. Nair, "Precise and ultrafast molecular sieving through graphene oxide membranes," *Science*, vol. 343, no. 6172, pp. 752–754, 2014.

[134] D. W. Boukhvalov, M. I. Katsnelson, and Y.-W. Son, "Origin of anomalous water permeation through graphene oxide membrane," *Nano letters*, vol. 13, no. 8, pp. 3930–3935, 2013.

[135] A. V. Talyzin, T. Hausmaninger, S. You, and T. Szabó, "The structure of graphene oxide membranes in liquid water, ethanol and water–ethanol mixtures," *Nanoscale*, vol. 6, no. 1, pp. 272–281, 2014.

[136] H. Li, Z. Song, X. Zhang, Y. Huang, S. Li, Y. Mao, H. J. Ploehn, Y. Bao, and M. Yu, "Ultrathin, molecular-sieving graphene oxide membranes for selective hydrogen separation," *Science*, vol. 342, no. 6154, pp. 95–98, 2013.

[137] H. W. Kim, H. W. Yoon, S.-M. Yoon, B. M. Yoo, B. K. Ahn, Y. H. Cho, H. J. Shin, H. Yang, U. Paik, S. Kwon, *et al.*, "Selective gas transport through few-layered graphene and graphene oxide membranes," *Science*, vol. 342, no. 6154, pp. 91–95, 2013.

[138] M. Hu and B. Mi, "Enabling graphene oxide nanosheets as water separation membranes," *Environmental science & technology*, vol. 47, no. 8, pp. 3715–3723, 2013.

[139] K. Raidongia and J. Huang, "Nanofluidic ion transport through reconstructed layered materials," *Journal of the American Chemical Society*, vol. 134, no. 40, pp. 16528–16531, 2012.

[140] Y. Wang, Z. Li, D. Hu, C.-T. Lin, J. Li, and Y. Lin, "Aptamer/graphene oxide nanocomplex for *in situ* molecular probing in living cells," *Journal of the American Chemical Society*, vol. 132, no. 27, pp. 9274–9276, 2010.

[141] N. Mohanty, M. Fahrenholtz, A. Nagaraja, D. Boyle, and V. Berry, "Impermeable graphenic encasement of bacteria," *Nano letters*, vol. 11, no. 3, pp. 1270–1275, 2011.

[142] D. Wei, J. Liang, Y. Zhu, Z. Yuan, N. Li, and Y. Qian, "Formation of graphene-wrapped nanocrystals at room temperature through the colloidal coagulation effect," *Particle & Particle Systems Characterization*, vol. 30, no. 2, pp. 143–147, 2013.

[143] H. Wang, Y. Yang, Y. Liang, J. T. Robinson, Y. Li, A. Jackson, Y. Cui, and H. Dai, "Graphene-wrapped sulfur particles as a rechargeable lithium–sulfur battery cathode material with high capacity and cycling stability," *Nano letters*, vol. 11, no. 7, pp. 2644–2647, 2011.

[144] G. Zhou, D.-W. Wang, F. Li, L. Zhang, N. Li, Z.-S. Wu, L. Wen, G. Q. Lu, and H.-M. Cheng, "Graphene-wrapped Fe_3O_4 anode material with improved reversible capacity and cyclic stability for lithium ion batteries," *Chemistry of Materials*, vol. 22, no. 18, pp. 5306–5313, 2010.

[145] Y. Chen, F. Guo, A. Jachak, S.-P. Kim, D. Datta, J. Liu, I. Kulaots, C. Vaslet, H. D. Jang, J. Huang, *et al.*, "Aerosol synthesis of cargo-filled graphene nanosacks," *Nano letters*, vol. 12, no. 4, pp. 1996–2002, 2012.

[146] J. Luo, X. Zhao, J. Wu, H. D. Jang, H. H. Kung, and J. Huang, "Crumpled graphene-encapsulated Si nanoparticles for lithium ion battery anodes," *The journal of physical chemistry letters*, vol. 3, no. 13, pp. 1824–1829, 2012.

[147] S. Liu, M. Hu, T. H. Zeng, R. Wu, R. Jiang, J. Wei, L. Wang, J. Kong, and Y. Chen, "Lateral dimension-dependent antibacterial activity of graphene oxide sheets," *Langmuir*, vol. 28, no. 33, pp. 12364–12372, 2012.

[148] N. I. Kovtyukhova, P. J. Ollivier, B. R. Martin, T. E. Mallouk, S. A. Chizhik, E. V. Buzaneva, and A. D. Gorchinskiy, "Layer-by-layer assembly of ultrathin composite films from micron-sized graphite oxide sheets and polycations," *Chemistry of Materials*, vol. 11, no. 3, pp. 771–778, 1999.

[149] K. Jiang, P. C. Thomas, S. P. Forry, D. L. DeVoe, and S. R. Raghavan, "Microfluidic synthesis of monodisperse pdms microbeads as discrete oxygen sensors," *Soft Matter*, vol. 8, no. 4, pp. 923–926, 2012.

[150] A. F. Routh, "Drying of thin colloidal films," *Reports on Progress in Physics*, vol. 76, no. 4, p. 046603, 2013.

[151] C.-N. Yeh, K. Raidongia, J. Shao, Q.-H. Yang, and J. Huang, "On the origin of the stability of graphene oxide membranes in water," *Nature chemistry*, vol. 7, no. 2, pp. 166–170, 2015.

[152] M. Acik, C. Mattevi, C. Gong, G. Lee, K. Cho, M. Chhowalla, and Y. J. Chabal, "The role of intercalated water in multilayered graphene oxide," *ACS Nano*, vol. 4, no. 10, pp. 5861–5868, 2010.

[153] P. J. Yunker, T. Still, M. A. Lohr, and A. Yodh, "Suppression of the coffee-ring effect by shape-dependent capillary interactions," *Nature*, vol. 476, no. 7360, pp. 308–311, 2011.

[154] R. D. Deegan, O. Bakajin, T. F. Dupont, G. Huber, S. R. Nagel, and T. A. Witten, "Contact line deposits in an evaporating drop," *Physical review E*, vol. 62, no. 1, p. 756, 2000.

[155] J. L. Tan, J. Tien, D. M. Pirone, D. S. Gray, K. Bhadriraju, and C. S. Chen, "Cells lying on a bed of microneedles: an approach to isolate mechanical force," *Proceedings of the National Academy of Sciences*, vol. 100, no. 4, pp. 1484–1489, 2003.

[156] Q. Cheng, Z. Sun, G. Meininger, and M. Almasri, "Flexible micropost arrays for studying traction forces of vascular smooth muscle cells,"

[157] Y. Ma, H. Davis, and L. Scriven, "Microstructure development in drying latex coatings," *Progress in Organic Coatings*, vol. 52, no. 1, pp. 46–62, 2005.

[158] O. D. Neikov, I. Murashova, N. A. Yefimov, and S. Naboychenko, *Handbook of non-ferrous metal powders: technologies and applications*. Elsevier, 2009.

[159] J. B. Park, Y.-J. Kim, S.-M. Kim, J. M. Yoo, Y. Kim, R. Gorbachev, I. Barbolina, S. J. Kim, S. Kang, M.-H. Yoon, *et al.*, "Non-destructive electron microscopy imaging and analysis of biological samples with graphene coating," *2D Materials*, vol. 3, no. 4, p. 045004, 2016.

[160] M. Wojcik, M. Hauser, W. Li, S. Moon, and K. Xu, "Graphene-enabled electron microscopy and correlated super-resolution microscopy of wet cells," *Nature communications*, vol. 6, 2015.

[161] J. Park, H. Park, P. Ercius, A. F. Pegoraro, C. Xu, J. W. Kim, S. H. Han, and D. A. Weitz, "Direct observation of wet biological samples by graphene liquid cell transmission electron microscopy," *Nano letters*, vol. 15, no. 7, pp. 4737–4744, 2015.

[162] R. Kempaiah, S. Salgado, W. L. Chung, and V. Maheshwari, "Graphene as membrane for encapsulation of yeast cells: protective and electrically conducting," *Chemical Communications*, vol. 47, no. 41, pp. 11480–11482, 2011.

[163] H. Demers, N. Poirier-Demers, A. R. Couture, D. Joly, M. Guilmain, N. de Jonge, and D. Drouin, "Three-dimensional electron microscopy simulation with the CASINO Monte Carlo software," *Scanning*, vol. 33, no. 3, pp. 135–146, 2011.

[164] J. Goldstein, D. E. Newbury, P. Echlin, D. C. Joy, A. D. Romig Jr, C. E. Lyman, C. Fiori, and E. Lifshin, *Scanning electron microscopy and X-ray microanalysis: a text for biologists, materials scientists, and geologists*. Springer Science & Business Media, 2012.

[165] S. Hofmann, "Quantitative depth profiling in surface analysis: A review," *Surface and Interface Analysis*, vol. 2, no. 4, pp. 148–160, 1980.

[166] M. Xu, D. Fujita, and N. Hanagata, "Monitoring electron-beam irradiation effects on graphenes by temporal auger electron spectroscopy," *Nanotechnology*, vol. 21, no. 26, p. 265705, 2010.

[167] J. Kim, L. J. Cote, F. Kim, and J. Huang, "Visualizing graphene based sheets by fluorescence quenching microscopy," *Journal of the American Chemical Society*, vol. 132, no. 1, pp. 260–267, 2009.

[168] G. Eda, G. Fanchini, and M. Chhowalla, "Large-area ultrathin films of reduced graphene oxide as a transparent and flexible electronic material," *Nature nanotechnology*, vol. 3, no. 5, pp. 270–274, 2008.

[169] P. J. Withers, "X-ray nanotomography," *Materials today*, vol. 10, no. 12, pp. 26–34, 2007.

[170] A. Hitchcock, J. Wang, and M. Obst, "3d chemical imaging with STXM spectro-tomography," *Microscopy and Microanalysis*, vol. 16, no. S2, pp. 850–851, 2010.

[171] J. S. Bunch, A. M. Van Der Zande, S. S. Verbridge, I. W. Frank, D. M. Tanenbaum, J. M. Parpia, H. G. Craighead, and P. L. McEuen, "Electromechanical resonators from graphene sheets," *Science*, vol. 315, no. 5811, pp. 490–493, 2007.

[172] F. Schedin, A. Geim, S. Morozov, E. Hill, P. Blake, M. Katsnelson, and K. Novoselov, "Detection of individual gas molecules adsorbed on graphene," *Nature materials*, vol. 6, no. 9, pp. 652–655, 2007.

[173] J.-N. Longchamp, T. Latychevskaia, C. Escher, and H.-W. Fink, "Low-energy electron transmission imaging of clusters on free-standing graphene," *Applied Physics Letters*, vol. 101, no. 11, p. 113117, 2012.

[174] J. Gu, X. Yang, Z. Lv, N. Li, C. Liang, and Q. Zhang, "Functionalized graphite nanoplatelets/epoxy resin nanocomposites with high thermal conductivity," *International Journal of Heat and Mass Transfer*, vol. 92, pp. 15–22, 2016.

[175] A. Reina, H. Son, L. Jiao, B. Fan, M. S. Dresselhaus, Z. Liu, and J. Kong, "Transferring and identification of single-and few-layer graphene on arbitrary substrates," *The Journal of Physical Chemistry C*, vol. 112, no. 46, pp. 17741–17744, 2008.

[176] C. R. Dean, A. F. Young, I. Meric, C. Lee, L. Wang, S. Sorgenfrei, K. Watanabe, T. Taniguchi, P. Kim, K. L. Shepard, *et al.*, "Boron nitride substrates for high-quality graphene electronics," *Nature nanotechnology*, vol. 5, no. 10, pp. 722–726, 2010.

[177] Z. Cheng, Q. Zhou, C. Wang, Q. Li, C. Wang, and Y. Fang, "Toward intrinsic graphene surfaces: a systematic study on thermal annealing and wet-chemical treatment of SiO_2-supported graphene devices," *Nano letters*, vol. 11, no. 2, pp. 767–771, 2011.

[178] M. Ishigami, J. Chen, W. Cullen, M. Fuhrer, and E. Williams, "Atomic structure of graphene on SiO_2," *Nano letters*, vol. 7, no. 6, pp. 1643–1648, 2007.

[179] J. D. Wood, G. P. Doidge, E. A. Carrion, J. C. Koepke, J. A. Kaitz, I. Datye, A. Behnam, J. Hewaparakrama, B. Aruin, Y. Chen, *et al.*, "Annealing free, clean graphene transfer using alternative polymer scaffolds," *Nanotechnology*, vol. 26, no. 5, p. 055302, 2015.

[180] P. Gupta, P. D. Dongare, S. Grover, S. Dubey, H. Mamgain, A. Bhattacharya, and M. M. Deshmukh, "A facile process for soak-and-peel delamination of cvd graphene from substrates using water," *Scientific reports*, vol. 4, 2014.

[181] L. Gao, W. Ren, H. Xu, L. Jin, Z. Wang, T. Ma, L.-P. Ma, Z. Zhang, Q. Fu, L.-M. Peng, *et al.*, "Repeated growth and bubbling transfer of graphene with millimetre-size single-crystal grains using platinum," *Nature communications*, vol. 3, p. 699, 2012.

[182] J. Kang, D. Shin, S. Bae, and B. H. Hong, "Graphene transfer: key for applications," *Nanoscale*, vol. 4, no. 18, pp. 5527–5537, 2012.

[183] A. V. Zaretski and D. J. Lipomi, "Processes for non-destructive transfer of graphene: widening the bottleneck for industrial scale production," *Nanoscale*, vol. 7, no. 22, pp. 9963–9969, 2015.

[184] C. T. Cherian, F. Giustiniano, I. Martin-Fernandez, H. Andersen, J. Balakrishnan, and B. Özyilmaz, "bubble-freeelectrochemical delamination of CVD graphene films," *Small*, vol. 11, no. 2, pp. 189–194, 2015.

[185] V. Oja and E. M. Suuberg, "Vapor pressures and enthalpies of sublimation of polycyclic aromatic hydrocarbons and their derivatives," *Journal of Chemical & Engineering Data*, vol. 43, no. 3, pp. 486–492, 1998.

[186] J.-N. Longchamp, C. Escher, and H.-W. Fink, "Ultraclean freestanding graphene by platinum-metal catalysis," *Journal of Vacuum Science & Technology B*, vol. 31, no. 2, p. 020605, 2013.

[187] G. Algara-Siller, O. Lehtinen, A. Turchanin, and U. Kaiser, "Dry-cleaning of graphene," *Applied Physics Letters*, vol. 104, no. 15, p. 153115, 2014.

[188] I. Vlassiouk, M. Regmi, P. Fulvio, S. Dai, P. Datskos, G. Eres, and S. Smirnov, "Role of hydrogen in chemical vapor deposition growth of large single-crystal graphene," *ACS Nano*, vol. 5, no. 7, pp. 6069–6076, 2011.

[189] D. Yoon, Y.-W. Son, and H. Cheong, "Negative thermal expansion coefficient of graphene measured by raman spectroscopy," *Nano letters*, vol. 11, no. 8, pp. 3227–3231, 2011.

[190] E. Mikmeková, H. Bouyanfif, M. Lejeune, I. Müllerová, M. Hovorka, M. Unčovskỳ, and L. Frank, "Very low energy electron microscopy of graphene flakes," *Journal of microscopy*, vol. 251, no. 2, pp. 123–127, 2013.

[191] G. Cheng, I. Calizo, and A. R. H. Walker, "Metal-catalyzed etching of graphene governed by metal–carbon interactions: A comparison of Fe and Cu," *Carbon*, vol. 81, pp. 678–687, 2015.

[192] Y. Lin and D. C. Joy, "A new examination of secondary electron yield data," *Surface and Interface analysis*, vol. 37, no. 11, pp. 895–900, 2005.

[193] Z. Li, Y. Wang, A. Kozbial, G. Shenoy, F. Zhou, R. McGinley, P. Ireland, B. Morganstein, A. Kunkel, S. P. Surwade, *et al.*, "Effect of airborne contaminants on the wettability of supported graphene and graphite," *Nature materials*, vol. 12, no. 10, pp. 925–931, 2013.

[194] O. Cretu, A. V. Krasheninnikov, J. A. Rodríguez-Manzo, L. Sun, R. M. Nieminen, and F. Banhart, "Migration and localization of metal atoms on strained graphene," *Physical review letters*, vol. 105, no. 19, p. 196102, 2010.

[195] P. Y. Huang, C. S. Ruiz-Vargas, A. M. van der Zande, W. S. Whitney, M. P. Levendorf, J. W. Kevek, S. Garg, J. S. Alden, C. J. Hustedt, Y. Zhu, *et al.*, "Grains and grain boundaries in single-layer graphene atomic patchwork quilts," *Nature*, vol. 469, no. 7330, pp. 389–392, 2011.

[196] X. Li, Y. Zhu, W. Cai, M. Borysiak, B. Han, D. Chen, R. D. Piner, L. Colombo, and R. S. Ruoff, "Transfer of large-area graphene films for high-performance transparent conductive electrodes," *Nano letters*, vol. 9, no. 12, pp. 4359–4363, 2009.

[197] A. Pirkle, J. Chan, A. Venugopal, D. Hinojos, C. Magnuson, S. McDonnell, L. Colombo, E. Vogel, R. Ruoff, and R. Wallace, "The effect of chemical residues on the physical and electrical properties of chemical vapor deposited graphene transferred to SiO_2," *Applied Physics Letters*, vol. 99, no. 12, p. 122108, 2011.

[198] M. Her, R. Beams, and L. Novotny, "Graphene transfer with reduced residue," *Physics Letters A*, vol. 377, no. 21, pp. 1455–1458, 2013.

[199] C. Fadley, R. Baird, W. Siekhaus, T. Novakov, and S. Bergström, "Surface analysis and angular distributions in X-ray photoelectron spectroscopy," *Journal of Electron Spectroscopy and Related Phenomena*, vol. 4, no. 2, pp. 93–137, 1974.

[200] W. S. Werner, "Simulation of electron spectra for surface analysis using the partial-intensity approach (PIA)," *Surface and interface analysis*, vol. 37, no. 11, pp. 846–860, 2005.

[201] G. Beamson, D. Briggs, *et al.*, *High resolution XPS of organic polymers*. Wiley, 1992.

[202] R. Zan, U. Bangert, Q. Ramasse, and K. S. Novoselov, "Interaction of metals with suspended graphene observed by transmission electron microscopy," *The journal of physical chemistry letters*, vol. 3, no. 7, pp. 953–958, 2012.

[203] E. Jensen, A. Burrows, and K. Mølhave, "Monolithic chip system with a microfluidic channel for *in situ* electron microscopy of liquids," *Microscopy and Microanalysis*, vol. 20, no. 2, pp. 445–451, 2014.

[204] M. Tanase, J. Winterstein, R. Sharma, V. Aksyuk, G. Holland, and J. A. Liddle, "High-resolution imaging and spectroscopy at high pressure: a novel liquid cell for the transmission electron microscope," *Microscopy and Microanalysis*, vol. 21, no. 6, pp. 1629–1638, 2015.

[205] M. Suga, H. Nishiyama, Y. Konyuba, S. Iwamatsu, Y. Watanabe, C. Yoshiura, T. Ueda, and C. Sato, "The atmospheric scanning electron microscope with open sample space observes dynamic phenomena in liquid or gas," *Ultramicroscopy*, vol. 111, no. 12, pp. 1650–1658, 2011.

[206] E. Jensen, C. Købler, P. S. Jensen, and K. Mølhave, "*In-situ* SEM microchip setup for electrochemical experiments with water based solutions," *Ultramicroscopy*, vol. 129, pp. 63–69, 2013.

[207] A. S. Al-Asadi, J. Zhang, J. Li, R. A. Potyrailo, and A. Kolmakov, "Design and application of variable temperature setup for scanning electron microscopy in gases and liquids at ambient conditions," *Microscopy and Microanalysis*, vol. 21, no. 3, pp. 765–770, 2015.

[208] N. Liv, D. S. van Oosten Slingeland, J.-P. Baudoin, P. Kruit, D. W. Piston, and J. P. Hoogenboom, "Electron microscopy of living cells during in situ fluorescence microscopy," *ACS Nano*, vol. 10, no. 1, pp. 265–273, 2015.

[209] J. D. Stoll and A. Kolmakov, "Electron transparent graphene windows for environmental scanning electron microscopy in liquids and dense gases," *Nanotechnology*, vol. 23, no. 50, p. 505704, 2012.

[210] C. Wang, Q. Qiao, T. Shokuhfar, and R. F. Klie, "High-resolution electron microscopy and spectroscopy of ferritin in biocompatible graphene liquid cells and graphene sandwiches," *Advanced Materials*, vol. 26, no. 21, pp. 3410–3414, 2014.

[211] Y. Han, K. Nguyen, Y. Ogawa, H. Shi, J. Park, and D. A. Muller, "Electron microscopy in air: Transparent atomic membranes and imaging modes," *Microscopy and Microanalysis*, vol. 21, p. 1111, 2015.

[212] H. I. Rasool, C. Ophus, W. S. Klug, A. Zettl, and J. K. Gimzewski, "Measurement of the intrinsic strength of crystalline and polycrystalline graphene," *Nature communications*, vol. 4, p. 2811, 2013.

[213] R. S. Weatherup, B. Eren, Y. Hao, H. Bluhm, and M. B. Salmeron, "Graphene membranes for atmospheric pressure photoelectron spectroscopy," *The journal of physical chemistry letters*, vol. 7, no. 9, pp. 1622–1627, 2016.

[214] J. J. Velasco-Velez, V. Pfeifer, M. Hävecker, R. S. Weatherup, R. Arrigo, C.-H. Chuang, E. Stotz, G. Weinberg, M. Salmeron, R. Schlögl, *et al.*, "Photoelectron spectroscopy at the graphene–liquid interface reveals the electronic structure of an electrodeposited cobalt/graphene electrocatalyst," *Angewandte Chemie International Edition*, vol. 54, no. 48, pp. 14554–14558, 2015.

[215] S. C. O'Hern, D. Jang, S. Bose, J.-C. Idrobo, Y. Song, T. Laoui, J. Kong, and R. Karnik, "Nanofiltration across defect-sealed nanoporous monolayer graphene," *Nano letters*, vol. 15, no. 5, pp. 3254–3260, 2015.

[216] M. S. Boutilier, C. Sun, S. C. O'Hern, H. Au, N. G. Hadjiconstantinou, and R. Karnik, "Implications of permeation through intrinsic defects in graphene on the design of defect-tolerant membranes for gas separation," *ACS Nano*, vol. 8, no. 1, pp. 841–849, 2014.

[217] S. C. O'Hern, C. A. Stewart, M. S. Boutilier, J.-C. Idrobo, S. Bhaviripudi, S. K. Das, J. Kong, T. Laoui, M. Atieh, and R. Karnik, "Selective molecular transport through intrinsic defects in a single layer of CVD graphene," *ACS Nano*, vol. 6, no. 11, pp. 10130–10138, 2012.

[218] B. Winter, U. Hergenhahn, M. Faubel, O. Björneholm, and I. V. Hertel, "Hydrogen bonding in liquid water probed by resonant Auger-electron spectroscopy," *The Journal of chemical physics*, vol. 127, no. 9, p. 094501, 2007.

[219] J. Kirz, C. Jacobsen, and M. Howells, "Soft X-ray microscopes and their biological applications," *Quarterly reviews of biophysics*, vol. 28, no. 1, pp. 33–130, 1995.

[220] M. P. Seah and D. Briggs, *Practical Surface Analysis: Auger and X-ray Photoelectron Spectroscopy*. John Wiley & Sons, 1990.

[221] J. Comyn, "Practical surface analysisby Auger and X-ray photoelectron spectroscopy: Edited by D. Briggs and MP Seah John Wiley and Sons limited, 1983," 1984.

[222] X. Llovet, C. J. Powell, F. Salvat, and A. Jablonski, "Cross sections for inner-shell ionization by electron impact," *Journal of Physical and Chemical Reference Data*, vol. 43, no. 1, p. 013102, 2014.

[223] M. Seah and I. Gilmore, "Quantitative AES. viii: analysis of auger electron intensities from elemental data in a digital auger database," *Surface and interface analysis*, vol. 26, no. 12, pp. 908–929, 1998.

[224] S. Mroczkowski and D. Lichtman, "Calculated Auger yields and sensitivity factors for KLL–NOO transitions with 1–10 kV primary beams," *Journal of Vacuum Science & Technology A: Vacuum, Surfaces, and Films*, vol. 3, no. 4, pp. 1860–1865, 1985.

[225] P. Ruffieux, P. Schwaller, O. Gröning, L. Schlapbach, P. Gröning, Q. Herd, D. Funnemann, and J. Westermann, "Experimental determination of the transmission factor for the omicron EA125 electron analyzer," *Review of Scientific Instruments*, vol. 71, no. 10, pp. 3634–3639, 2000.

[226] A. Jablonski, A. Jablonski, and C. Powell, *NIST backscattering-correction-factor database for Auger electron spectroscopy*. US Department of Commerce, National Institute of Standards and Technology, 2016.

[227] M. Xu, D. Fujita, J. Gao, and N. Hanagata, "Auger electron spectroscopy: a rational method for determining thickness of graphene films," *ACS Nano*, vol. 4, no. 5, pp. 2937–2945, 2010.

[228] S. Thürmer, R. Seidel, M. Faubel, W. Eberhardt, J. C. Hemminger, S. E. Bradforth, and B. Winter, "Photoelectron angular distributions from liquid

water: Effects of electron scattering," *Physical review letters*, vol. 111, no. 17, p. 173005, 2013.

[229] P. Slavicek, N. V. Kryzhevoi, E. F. Aziz, and B. Winter, "Relaxation processes in aqueous systems upon X-ray ionization: Entanglement of electronic and nuclear dynamics," *The journal of physical chemistry letters*, vol. 7, no. 2, pp. 234–243, 2016.

[230] T. Jahnke, H. Sann, T. Havermeier, K. Kreidi, C. Stuck, M. Meckel, M. Schöffler, N. Neumann, R. Wallauer, S. Voss, *et al.*, "Ultrafast energy transfer between water molecules," *Nature Physics*, vol. 6, no. 2, p. 139, 2010.

[231] D. Briggs and M. Seah, "Practical surface analysis by Auger and X-ray photoelectron spectroscopy, John Wiley and Sons," *New York*, 1990.

[232] B. H. Frazer, B. Gilbert, B. R. Sonderegger, and G. De Stasio, "The probing depth of total electron yield in the sub-kev range: TEY-XAS and X-PEEM," *Surface science*, vol. 537, no. 1, pp. 161–167, 2003.

[233] M. C. Tinone, N. Ueno, J. Maruyama, K. Kamiya, Y. Harada, T. Sekitani, and K. Tanaka, "Site specific photochemical reaction of PMMA and related polymers by inner shell electron excitation," *Journal of electron spectroscopy and related phenomena*, vol. 80, pp. 117–120, 1996.

[234] A. Nilsson, D. Nordlund, I. Waluyo, N. Huang, H. Ogasawara, S. Kaya, U. Bergmann, L.-Å. Näslund, H. Öström, P. Wernet, *et al.*, "X-ray absorption spectroscopy and X-ray Raman scattering of water and ice; an experimental view," *Journal of Electron Spectroscopy and Related Phenomena*, vol. 177, no. 2, pp. 99–129, 2010.

[235] T. Fransson, Y. Harada, N. Kosugi, N. A. Besley, B. Winter, J. J. Rehr, L. G. Pettersson, and A. Nilsson, "X-ray and electron spectroscopy of water," *Chemical reviews*, vol. 116, no. 13, pp. 7551–7569, 2016.

[236] P. Wernet, D. Nordlund, U. Bergmann, M. Cavalleri, M. Odelius, H. Ogasawara, L.-Å. Näslund, T. Hirsch, L. Ojamäe, P. Glatzel, *et al.*, "The structure of the first coordination shell in liquid water," *Science*, vol. 304, no. 5673, pp. 995–999, 2004.

[237] L. Frank, E. Mikmeková, I. Müllerová, and M. Lejeune, "Counting graphene layers with very slow electrons," *Applied Physics Letters*, vol. 106, no. 1, p. 013117, 2015.

[238] C. Laffon, S. Lacombe, F. Bournel, and P. Parent, "Radiation effects in water ice: A near-edge X-ray absorption fine structure study," *The Journal of chemical physics*, vol. 125, no. 20, p. 204714, 2006.

[239] J.-J. Velasco-Velez, C. H. Wu, T. A. Pascal, L. F. Wan, J. Guo, D. Prendergast, and M. Salmeron, "The structure of interfacial water on gold electrodes studied by X-ray absorption spectroscopy," *Science*, p. 1259437, 2014.

[240] Y.-D. Chiu, W.-P. Dow, S.-M. Huang, S.-L. Yau, and Y.-L. Lee, "Sensitivity enhancement for quantitative electrochemical determination of a trace amount of accelerator in copper plating solutions," *Journal of The Electrochemical Society*, vol. 158, no. 5, pp. D290–D297, 2011.

[241] N. Kolmakova and A. Kolmakov, "Scanning electron microscopy for *in Situ* monitoring of semiconductor- liquid interfacial processes: Electron assisted reduction of Ag ions from aqueous solution on the surface of TiO_2 rutile nanowire," *The Journal of Physical Chemistry C*, vol. 114, no. 40, pp. 17233–17237, 2010.

[242] E. U. Donev and J. T. Hastings, "Electron-beam-induced deposition of platinum from a liquid precursor," *Nano letters*, vol. 9, no. 7, pp. 2715–2718, 2009.

[243] J. H. Park, N. M. Schneider, J. M. Grogan, M. C. Reuter, H. H. Bau, S. Kodambaka, and F. M. Ross, "Control of electron beam-induced Au nanocrystal growth kinetics through solution chemistry," *Nano letters*, vol. 15, no. 8, pp. 5314–5320, 2015.

[244] R. R. Unocic, A. R. Lupini, A. Y. Borisevich, D. A. Cullen, S. V. Kalinin, and S. Jesse, "Direct-write liquid phase transformations with a scanning transmission electron microscope," *Nanoscale*, vol. 8, no. 34, pp. 15581–15588, 2016.

[245] K. W. Noh, Y. Liu, L. Sun, and S. J. Dillon, "Challenges associated with *in-situ* TEM in environmental systems: The case of silver in aqueous solutions," *Ultramicroscopy*, vol. 116, pp. 34–38, 2012.

[246] M. R. Wright, *An introduction to aqueous electrolyte solutions*. John Wiley & Sons, 2007.

[247] S. Nappini, A. Matruglio, D. Naumenko, S. Dal Zilio, F. Bondino, M. Lazzarino, and E. Magnano, "Graphene nanobubbles on TiO_2 for *in-operando* electron spectroscopy of liquid-phase chemistry," *Nanoscale*, vol. 9, no. 13, pp. 4456–4466, 2017.

[248] A. Yulaev, V. Oleshko, J. J. McClelland, P. Haney, A. A. Talin, M. S. Leite, and A. Kolmakov, "From nanoclusters to nanowires and back: radical transformations in plated Li metal morphology observed using *operando* electron microscopy," *In preparation*.

[249] J.-M. Tarascon and M. Armand, "Issues and challenges facing rechargeable lithium batteries," *Nature*, vol. 414, no. 6861, pp. 359–367, 2001.

[250] M. Armand and J.-M. Tarascon, "Building better batteries," *Nature*, vol. 451, no. 7179, pp. 652–657, 2008.

[251] S. Chu and A. Majumdar, "Opportunities and challenges for a sustainable energy future," *Nature*, vol. 488, no. 7411, p. 294, 2012.

[252] F. Yonemoto, A. Nishimura, M. Motoyama, N. Tsuchimine, S. Kobayashi, and Y. Iriyama, "Temperature effects on cycling stability of Li plating/stripping on Ta-doped $Li_7La_3Zr_2O_{12}$," *Journal of Power Sources*, vol. 343, pp. 207–215, 2017.

[253] J. Janek and W. G. Zeier, "A solid future for battery development," *Nature Energy*, vol. 1, p. 16141, 2016.

[254] G. Stone, S. Mullin, A. Teran, D. Hallinan, A. Minor, A. Hexemer, and N. Balsara, "Resolution of the modulus versus adhesion dilemma in solid polymer electrolytes for rechargeable lithium metal batteries," *Journal of The Electrochemical Society*, vol. 159, no. 3, pp. A222–A227, 2012.

[255] D. Lin, Y. Liu, Z. Liang, H.-W. Lee, J. Sun, H. Wang, K. Yan, J. Xie, and Y. Cui, "Layered reduced graphene oxide with nanoscale interlayer gaps as a stable host for lithium metal anodes," *Nature nanotechnology*, vol. 11, no. 7, pp. 626–632, 2016.

[256] K. K. Fu, Y. Gong, B. Liu, Y. Zhu, S. Xu, Y. Yao, W. Luo, C. Wang, S. D. Lacey, J. Dai, *et al.*, "Toward garnet electrolyte–based Li metal batteries: An ultrathin, highly effective, artificial solid-state electrolyte/metallic Li interface," *Science Advances*, vol. 3, no. 4, p. e1601659, 2017.

[257] Y. Takeda, O. Yamamoto, and N. Imanishi, "Lithium dendrite formation on a lithium metal anode from liquid, polymer and solid electrolytes," *Electrochemistry*, vol. 84, no. 4, pp. 210–218, 2016.

[258] J. Qian, W. A. Henderson, W. Xu, P. Bhattacharya, M. Engelhard, O. Borodin, and J.-G. Zhang, "High rate and stable cycling of lithium metal anode," *Nature communications*, vol. 6, 2015.

[259] W. Luo, Y. Gong, Y. Zhu, K. K. Fu, J. Dai, S. D. Lacey, C. Wang, B. Liu, X. Han, Y. Mo, *et al.*, "Transition from superlithiophobicity to superlithiophilicity of garnet solid-state electrolyte," *Journal of the American Chemical Society*, vol. 138, no. 37, pp. 12258–12262, 2016.

[260] X. Han, Y. Gong, K. K. Fu, X. He, G. T. Hitz, J. Dai, A. Pearse, B. Liu, H. Wang, G. Rubloff, *et al.*, "Negating interfacial impedance in garnet-based solid-state Li metal batteries," *Nature materials*, vol. 16, no. 5, pp. 572–579, 2017.

[261] D. Santhanagopalan, D. Qian, T. McGilvray, Z. Wang, F. Wang, F. Camino, J. Graetz, N. Dudney, and Y. S. Meng, "Interface limited lithium transport in solid-state batteries," *The journal of physical chemistry letters*, vol. 5, no. 2, pp. 298–303, 2013.

[262] A. A. Talin, D. Ruzmetov, A. Kolmakov, K. McKelvey, N. Ware, F. El Gabaly, B. Dunn, and H. S. White, "Fabrication, testing, and simulation of all-solid-state three-dimensional Li-ion batteries," *ACS applied materials & interfaces*, vol. 8, no. 47, pp. 32385–32391, 2016.

[263] P. Fallon and L. M. Brown, "Analysis of chemical-vapour-deposited diamond grain boundaries using transmission electron microscopy and parallel electron energy loss spectroscopy in a scanning transmission electron microscope," *Diamond and Related Materials*, vol. 2, no. 5-7, pp. 1004–1011, 1993.

[264] R. F. Egerton, *Electron energy-loss spectroscopy in the electron microscope*. Springer Science & Business Media, 2011.

[265] T. Michely and J. Krug, "Islands, mounds and atoms, vol. 42," 2004.

[266] M. Einax, W. Dieterich, and P. Maass, "Colloquium: Cluster growth on surfaces: Densities, size distributions, and morphologies," *Reviews of Modern Physics*, vol. 85, no. 3, p. 921, 2013.

[267] H. Seiler, "Secondary electron emission in the scanning electron microscope," *Journal of Applied Physics*, vol. 54, no. 11, pp. R1–R18, 1983.

[268] R. Cahn and P. Haasen, "Physical metallurgy," 1983.

[269] M. M. Islam and T. Bredow, "Density functional theory study for the stability and ionic conductivity of Li_2O surfaces," *The Journal of Physical Chemistry C*, vol. 113, no. 2, pp. 672–676, 2008.

[270] E. Dologlou, "Self-diffusion in solid lithium," *Glass Physics and Chemistry*, vol. 36, no. 5, pp. 570–574, 2010.

[271] Y. Oishi, Y. Kamei, M. Akiyama, and T. Yanagi, "Self-diffusion coefficient of lithium in lithium oxide," *Journal of Nuclear Materials*, vol. 87, no. 2-3, pp. 341–344, 1979.

[272] R.-Q. Zhang, Y. Lifshitz, and S.-T. Lee, "Oxide-assisted growth of semiconducting nanowires," *Advanced Materials*, vol. 15, no. 7-8, pp. 635–640, 2003.

[273] H. Zheng, Y. Liu, S. X. Mao, J. Wang, and J. Y. Huang, "Beam-assisted large elongation of *in situ* formed Li_2O nanowires," *Scientific reports*, vol. 2, p. 542, 2012.

[274] J. Coburn and H. F. Winters, "Ion-and electron-assisted gas-surface chemistryan important effect in plasma etching," *Journal of Applied physics*, vol. 50, no. 5, pp. 3189–3196, 1979.